THE UNIVERSITY OF CHICAGO

ENGINEERING A PROTEIN-INSPIRED SYNTHETIC MATERIAL TO SEQUESTER AND SENSE PHOSPHATE

A DISSERTATION SUBMITTED TO

THE FACULTY OF THE PRITZKER SCHOOL OF MOLECULAR ENGINEERING

IN CANDIDACY FOR THE DEGREE OF

DOCTOR OF PHILOSOPHY

BY

WHITNEY CLAIRE FOWLER

CHICAGO, ILLINOIS

AUGUST 2022

“But I am among you as one who serves.”

TABLE OF CONTENTS

LIST OF FIGURES

LIST OF TABLES

ACKNOWLEDGMENTS

My experience getting my Ph.D. through the Pritzker School of Molecular Engineering (PME) has been a privilege and a joy. This sentiment in inextricably linked to the kindness and faithfulness of many people who have so wonderfully supported me during these years, both professionally and personally. I am grateful to articulate my thankfulness for them here.

Many people have played an instrumental role in my growth as an academic. Most obviously, I am incredibly grateful for the mentorship and support given by my two Ph.D. advisors, Matt Tirrell and Juan de Pablo. They have modeled to me what excellent, cutting-edge, and honest scholarship looks like, all the while being humble, good people who treat others with respect. Because of them, I feel able to contribute to the beautiful landscape of intellectual inquiry in a more significant way, and I feel very privileged to have their examples of scholarship and mentorship to emulate as I continue in academia.

I also have been transformed as a scholar through many other academic relationships for which I am deeply grateful. Prof. Moshe Gottlieb went above his obligation as a collaborator to invest in me as an international mentee and host me on a beautiful visit to his beautiful country of Israel. My candidacy and defense committee members—Dr. Seth Darling, Dr. Jim Skinner, and Dr. Junhong Chen—have offered invaluable support and insight on my work. I am deeply grateful for Prof. Amanda Marciel, who significantly invested in me as a young graduate student when I had very little experience and who remains a role model for me as a woman leader in STEM. Other mentor figures in the Tirrell group also had a significant impact on my growth, including Prof. Handan Acar, Dr. Mat Schnorenberg, Dr. Jeff Ting, Dr. Alex Marras, and Dr. Yu Tian, all of whom spent time investing in me as a colleague. The camaraderie of many other Tirrell group members has also been incredibly meaningful, especially in their unified support of me during hard seasons,

including Dr. Siqi Meng, Dr. Ge Zhang, Dr. Angelika Neitzel, Kaden Stevens, Carlos Jimenez, and many others. I am also thankful for the support and investment of many core facility scientists, including Dr. Tera Lavoie, Dr. Elena Solomaha, and Dr. Rebecca Sponenburg. Finally, I significantly grew as an educator and pedagogue while at the PME, and I am grateful for key mentors in this area including Laura Rico-Beck, Dr. Rovana Popoff, and Dr. Kiki Zissimopoulos.

It has been a unique privilege to collaborate closely with six other women on my research project. I have been so thankful for Dr. Ashely Guo and Chuting Deng for combining their computational insights with my experimental work to discover interesting results. All simulations in this thesis were performed by them. I also loved working with Michal Zaiden, the postdoctoral scholar at Ben Gurion University, who has supported me as a friend and refined me as a colleague. Lastly, it has been a deep privilege to mentor and work alongside Gabriella Griffen, Tess Teodoro, and Jihyeon Yeo, three UChicago undergraduate students who have now graduated. The three of them brought life to the many weeks of research work, and I loved learning from them as well.

Finally, I am very deeply grateful for the support of my friends and family during my studies. I have been blessed with an incredible community here in Chicago through my church with too many people to name that have each played significant roles in my life. People there like Torie Lettow, Ali McMillan, Paul Calio, Matthew Du, members of my community groups, and many others have walked with me through highs and lows. It has also been a rich blessing to mentor and grow with many undergrad students through my church. My parents, siblings, and extended family have all been amazingly supportive of me beyond what words can express. And finally, I would not be true to myself if I omitted thanks and acknowledgement to Jesus Christ my Lord, who has loved me, comforted me, healed me, and faithfully led me. Dedicating my work, life, and love to Him is the greatest privilege of all.

ABSTRACT

Biological materials possess highly sophisticated material properties that are intrinsically connected to their molecular and intermolecular design. In recent decades, engineers have designed creative synthetic material platforms that translate these properties to tunable material systems in order to address emerging challenges facing society. One intriguing biological property to mimic is the ability of protein to molecularly recognize and bind to specific targets, which could be repurposed to address key challenges such as resource recovery from water or detecting harmful aqueous contaminants. However, tunable bio-inspired material platforms with this function are rare. Here, this thesis presents the design, synthesis, and characterization of a material platform based on peptide amphiphile micelles that exploits the natural binding ability of protein and selectively and reversibly binds to phosphate. By utilizing a stimuli-responsive pH trigger, this material is engineered for resource recovery and detection of phosphate by incorporating a protein-extracted binding sequence into the material framework. In Chapter 2, the prototype design, synthesis, and characterization of single-component peptide amphiphile micelles are described. The fundamental phosphate binding characteristics are probed, including the pH-dependence of binding, selectivity over nitrate and nitrite, and reusability of the material. Molecular dynamics simulations are also employed to gain further insight into the molecular mechanism of binding in this system. Chapter 3 describes an enhanced design based on multi-component peptide amphiphile micelles and single peptide resin systems. This work provides additional insight into design principles for mimicking protein-inspired binding of phosphate in synthetic materials. Chapter 4 describes an unexpected intrinsic fluorescence property that was discovered in these peptide amphiphile micelles according to the aggregation-induced emission (AIE) effect. The fundamental fluorescent properties are characterized, and the ability of this material to signal

phosphate binding is described. Chapter 5 summarizes the work and discusses future directions. Overall, this work presents a rational design and thorough study of a novel synthetic material platform that harnesses the targeting ability of proteins, offering valuable insight for future protein-inspired synthetic materials designed to this end.

CHAPTER 1.

INTRODUCTION

1.1 BIOMIMETIC BINDING MATERIALS: MOTIVATION AND BACKGROUND

Biologically inspired materials have received intense interest in recent decades,[1–3] and for good reason—Nature's materials have evolved to perform certain functions extremely well and with exact precision.[4] Since these functions are intrinsically related to their material design and inter- and intra-molecular interactions, scholars have been wise to learn from biological materials and then harness this insight to engineer advanced functions into informed synthetic materials, resulting in important advances in fundamental insight and practical application. These applications of biomimetic materials can be directly derived from native protein functionality,[1] such as materials for cellular adhesion,[2,5] collagen-based mechanical properties,[6] or antimicrobial activity.[7–9] Functionality of biomimetic materials can also be repurposed for an engineered application distinct from their native design, such as designing materials for targeted drug delivery,[10] stimuli responsiveness,[11] nerve regeneration,[12,13] or treatment for atherosclerosis.[14,15]

One intriguing protein-inspired function to repurpose is the ability of proteins to target and sequester a specific molecule. It is well known that proteins have the ability to recognize and reversibly bind to a specific target, and many biological functions hinge upon this key protein trait. Molecular-recognition materials engineered to mimic this function could access unique design traits of proteins to perform precise protein-inspired binding, with applications in resource reclamation,[16] sensing applications,[17,18] or biomedical use, including targeted removal of excess nutrients affiliated with certain diseases, such as a high concentration of phosphate for patients with chronic kidney disease.[19]

Several biologically inspired materials have already been engineered with derived protein-binding function. Chuan He and coworkers engineered a protein that was able to bind to uranyl with femtomolar affinity through using a computational screening process to identify repurposed uranyl-binding sites.[20] This group also repurposed molybdate-binding protein to bind to perrhenate with increased affinity through selective mutation.[21] Using a similar computational design approach used to design the uranyl-binding protein, Dan Tawfik and coworkers designed de novo β-α repeat proteins that binds to phosphate, using as few as 55 amino acid residues which is well below the typical size of a protein.[22] Biomimetic binding materials have also been identified using a combinatorial library approach, with Abigail Knight and coworkers successfully designing peptoid-based materials that selectively bound to chromium[23] and cadmium.[24] While the examples described so far have all been *in situ*, several groups have found success in tethering a bio-inspired binding moiety to a surface. Julie Renner and coworkers immobilized a peptide to a metal surface to develop an adsorbent material. When the peptide selectively bound to cerium, it was also able to selectively adsorb phosphate.[16] In a similar manner, Rui Zhao and coworkers immobilized a peptide to a nanointerface to capture circulating tumor cells.[25]

While these works represent important progress in designing bio-inspired binding materials, there are among the very limited number of engineered systems designed to this end. Mimicking protein-binding offers enticing potential to achieve heightened specificity, but it is nevertheless quite difficult to successfully translate this protein behavior into a synthetic material. This discrepancy between potential and reality prompts a call for newly engineered protein-analogous materials to be repurposed for this function, employing a feedback design scheme of complementary experimental and computational results for optimized molecular design and mechanistic insight.

1.2 Phosphate as a Strategic Target for a Biomimetic Binding Material

1.2.1 Motivation for Resource Recovery and Phosphate Sequestering and Sensing

A protein-inspired binding material would be uniquely suited for the emerging need to recover and conserve resources from water. Essential resources are being unsustainably depleted while the global demand increasingly rises, and society is turning towards wastewater as a new source for reclaiming valuable products or toxic chemicals,[26–29] including rare metals,[30] critical fertilizer ingredients,[31] and pharmaceutical products.[32,33] Our ability to harvest these, however, is limited by several infrastructural, societal, and technological challenges.[26] In particular, the emerging field of resource reclamation lacks versatile materials that are molecularly engineered to recognize, capture, and release their targets in a controllable and practical manner for recovery and detection.

A strategic target compound for development of a prototype capture-and-release material is phosphate, a commodity widely targeted by technologies for reclamation.[16,31,34–41] This limited resource is an essential ingredient in many fertilizers,[42,43] but at its current rate of extraction, it is projected to be expended in 50 to 100 years.[44] Paradoxically, this highly coveted resource is also being discarded in large amounts in agricultural runoff streams, thereby causing severe eutrophication and vastly disrupting natural ecosystems.[45] An effective, capture-and-release material could be strategically employed to target and recover phosphate from where it is detrimental and reinsert it where it is depleted yet greatly needed.

There has also been complementary interest in designing phosphate-specific sensors to detect phosphate concentration in soil in real-time.[46] This data would be highly valuable to farmers who could adjust their fertilizer distribution accordingly, preventing large fertilizer excesses from entering runoff and damaging local ecosystems.

1.2.2 Current Bio-Inspired Approaches for Phosphate Recovery

Several techniques already exist that rely upon bio-inspired targeting to reclaim phosphate for reuse. Natural abilities of phosphate-processing organisms have been harnessed in their raw form to reclaim phosphorus,[40] including the prokaryotic processes of enhanced biological phosphorus removal or eukaryotic technologies such as floating algae farming. A challenge for these technologies is that of grappling with complex operating conditions required for optimized resource reclamation.[31,35,38–40] On a larger scale, engineered wetlands systems have also been employed to reclaim nutrients, but thus far they have not gained momentum in use due to a limited resource return rate.[35] Since these technologies employ organisms in their raw form, they face the innate restrictions imposed by the organism's metabolism, thereby restricting opportunities for optimization. This unique biological sequestering ability could be fully realized if it were intentionally designed into a synthetic materials platform. However, attempts to develop a hierarchically driven, biomimetic materials design scheme for resource capture and release have been limited.

1.2.3 Insights from Phosphate-Binding in Proteins and Synthetic Derivatives

Phosphate is a strategic target for a bio-inspired molecular recognition material not just because there is a clear need for its selective recovery and detection, but also because there is a rich body of literature that has uncovered critical mechanistic insights into phosphate binding by phosphate-binding proteins (PBPs), thus making material design and development feasible. To design a synthetic phosphate-binding material inspired by these proteins, one must identify the key binding factors utilized by proteins and consider how to best translate them into a tunable synthetic material.

Phosphate-binding behavior by PBPs was first studied with intent interest in the 1980s[47] and early 1990s[48] and have been further characterized since then, with three key binding traits being identified: electrostatic stabilization, hydrogen bonding, and local nested cavity conformation.[49] The first studies identified that the majority of PBPs possess a conserved sequence, denoted the P-loop[48,50] or later the Walker A motif,[22] that has the amino acid sequence of GXXXGK(T,S), where X could be any amino acid. This motif was found to adopt an LRLR nested cavity formation that usually served as a turning point in the structure of proteins between an alpha helix and a beta-sheet on either side of this sequence, with "L" and "R" referring to angles that the local structure adopts.[49,51–54] This discovered nest was termed a "giant anion hole" in the 1980s.[47] The conserved glycine and lysine residues have also been emphasized as key factors in facilitating phosphate binding.[55] The positively charged amine of the lysine side chain likely plays a critical role in stabilizing the negatively charged target molecule, and the flexibility of the glycine residues facilitates the Walker A motif to readily adopt the angles necessary to form the nested cavity conformation to bind to phosphate. In addition to charge and conformation playing critical roles in binding, the final identified contributor for binding is the hydrogen bonding that occurs through the amide bonds in the backbone of the peptide, which are displayed to the anion in the nest.

This functional motif is simple and quite short compared to other binding schemes that proteins employ, which often incorporate complex tertiary and quaternary structures that utilize amino acid residues from remote locations in a protein for binding.[4] As such, several studies have sought to deploy this shorter motif in engineered systems to bind to phosphate, with promising preliminary success. As previously mentioned, Dan Tawfik and coworkers performed a thoughtful study to engineer a phosphate-binding protein-inspired material that utilized this Walker A motif while incorporating alpha helices and beta sheet segments on either side to more closely mimic

the native state.[22] Several other studies further reduced the native structure to isolate only the P-loop sequence, SGAGKT, and found that this short peptide sequence was able to bind to phosphate as well.[56,57] However, though these initial studies offer promise and important insight, they are limited in their ability to be practically implemented for reclamation purposes given that they are small molecules, and there is additional room for optimization of the binding methodology. Thus, one can harness the three key identified binding factors—charge, hydrogen bonding, and local nest conformation—along with the promise of the initial studies, and engineer an optimized, responsive system that can molecularly recognize phosphate through mimicking protein behavior for practical application, with promise to readily adapt the binding motif to target other molecules of interest.

1.3 Peptide Amphiphile Micelles: Strategic Platform for Biomimetic Binding

Peptide amphiphiles (PAs) are a strategic platform for design of a novel biomimetic molecular-recognition material due to their protein-mimicking features and their precise control over molecular and macroscopic design for practical application. PAs consist of a short peptide sequence "headgroup" conjugated to a hydrophobic "tail" that causes spontaneous self-assembly into micelles in water. The PAs can be precisely designed and synthesized to feature multiple functional "building block" segments,[58,59] such as protein-derived binding amino acid sequences that are systematically displayed upon assembly in the micelle coronae,[60] or segments to promote protein secondary structure conformations in the headgroup,[61] a well-known critical component in biological binding. Indeed, PAs have previously harnessed this specific targeting ability of biological molecules for use in targeted drug delivery[14,62] and cell adhesion,[5] making this platform well-positioned to transition in application towards specified targeting of selected resources. Along those lines, PAs have recently been studied for macromolecular harvesting of proteins,[63] which exploits similar concepts but could have differences in its practical implementation due to

molecular size and transport phenomena. Novel material design is easily accomplished through use of well-studied, sequence-specific synthesis techniques to produce environmentally benign materials, an advantage over other novel capture and release materials such as metal organic frameworks that have complex synthetic routes, can be toxic, and are unstable in water.[64–66]

In addition to possessing advantages in synthesis and targeted binding, PAs also feature unique material characteristics with precise control over multiple length scales as well as stimuli-responsiveness. The micelle architecture of PA spontaneous self-assembly can be precisely tuned according to well-studied strategies to direct the PAs towards self-assembly into wormlike micelles that form an entangled, dense suspension.[67] This network can then be designed to host a multitude of phosphate-binding sites on its exposed surfaces, providing a physical structure for capture of phosphate. PAs have also been designed for pH-related stimuli responsive behavior,[11] making this platform promising for reclamation of phosphate once it is bound or for stimuli-responsive sensing for detection of phosphate in water. Although the initial PA prototype will target phosphate, the versatility and breadth of PAs allows for straightforward modification of peptide binding sequences to target, sequester, and reclaim, with potentially high avidity and selectivity, a large number of other valuable resources such as heavy metals, pharmaceuticals, or bioplastics.

1.4 Peptide Amphiphile Micelles for Sequestering and Sensing of Phosphate

In this thesis, I present a newly engineered peptide amphiphile material that targets phosphate for harvesting and detection, exploiting the natural ability of proteins to bind and incorporating it into a tunable synthetic material. In Chapter 2, I present the prototype design, synthesis, and characterization of a single-component PA micelle that was shown to selectively and reversibly bind to phosphate through pH-responsive binding behavior. This work translated

the insights from protein binding behavior into a deployable material for selective harvesting of critical nutrients, and it employed molecular dynamic simulations to elucidate critical insight into the binding mechanism within the peptide micelle corona. With this work, ion recognition was successfully bridged from proteins to synthetic material.

In Chapter 3, I describe the advanced engineered design of a multi-component PA micelle aimed to further enhance selectivity and binding efficacy. By combining experimental and computational results, this work derived intriguing insights into ion binding within a PA micelle that was found to perform binding mechanisms unavailable in native proteins. This chapter also describes binding to isolated peptides on a solid support resin, which provides additional insight into the mechanism of binding within a densely packed peptide micelle corona. This work is an important step towards determining which features are required to translate protein functionality into the PA micelle material platform, offering insights for future rounds of design and optimization.

In Chapter 4, I describe an unexpected intrinsic fluorescence property that was discovered in this PA micelle material attributed to the aggregation-induced emission (AIE) effect. I characterize this fluorescence for three PA systems, which offers preliminary insight on how to further optimize emission effects in future rounds of design. I then show preliminary results describing its promise as a sensing material for phosphate detection in water. Concluding remarks are then presented in Chapter 5.

CHAPTER 2.

DESIGN, SYNTHESIS AND CHARACTERIZATION OF SINGLE-COMPONENT PEPTIDE AMPHIPHILE MICELLES TO CAPTURE AND RECLAIM PHOSPHATE

This chapter is modified and reprinted with permission from Fowler, W. C.; Deng, C.; Griffen, G. M.; Teodoro, T.; Guo, A. Z.; Zaiden, M.; Gottlieb, M.; Pablo, J. J. De; Tirrell, M. V. Harnessing Peptide Binding to Capture and Reclaim Phosphate. *J. Am. Chem. Soc.* **2021**, *143*, 4440–4450. https://pubs.acs.org/doi/10.1021/jacs.1c01241.

2.1 INTRODUCTION

In this work, we present a prototype of a novel materials platform that relies on self-assembled peptide amphiphiles to controllably capture, release, and reclaim phosphate through a pH-responsive trigger, exploiting the natural binding ability of proteins. The micelle architecture of PA spontaneous self-assembly was tuned according to well-studied strategies to direct the PAs towards self-assembly into wormlike micelles that form an entangled, dense suspension.[67] This network hosts a multitude of phosphate-binding sites on its exposed surfaces and provides a physical structure through which phosphate-rich water can flow, capturing the phosphate ions on the strands of the network. The ions can later be controllably released by a pH trigger. The self-assembled network thereby inherently offers a practical means to reclaim this valuable resource. To develop the proposed materials and gain a mechanistic understanding of the molecular processes through which phosphate is captured, we have relied on molecular simulations of the molecules and self-assembled structures of interest. Although the initial prototype will target phosphate, the versatility and breadth of PAs positions us to modify peptide binding sequences to target, sequester, and reclaim, with potentially high avidity and selectivity, a large number of other

valuable resources such as heavy metals, pharmaceuticals, or bioplastics, with the potential to truly become a modular materials platform for wastewater resource recovery.

2.2 Experimental Methods

2.2.1 Synthesis and Purification of Peptide Amphiphile Micelles and Micelle Preparation Procedure

Two peptide sequences (GGGSGAGKT and SGAGKTSSSGGK(dde-protected)GGHHHSGAGKT) were synthesized on 0.25 mmoles of rink amide resin (Novabiochem) through standard FMOC solid phase peptide synthesis using an automated Prelude X Benchtop Synthesizer (Protein Technologies, Tuscon, AZ, USA). For each coupling step, the FMOC protecting group was first removed from the resin using 20% piperidine in dimethylformamide (DMF). Separately, the amino acid was activated with N,N,N',N'-Tetramethyl-O-(1H-benzotriazol-1-yl)uranium hexafluorophosphate (HBTU) and N,N-Diisopropylethylamine (DIPEA) in a molar ratio of 1:4:3.95:8 of resin: amino acid: HBTU: DIPEA. The activated amino acid cocktail was then added to the deprotected resin and then allowed to mix to conjugate.

After the amino acid couplings were completed, each peptide was then coupled with a palmitic acid tail. For the GGGSGAGKT peptide, the palmitic acid was simply conjugated to the deprotected glycine N-terminus. For the SGAGKTSSSGGK(dde-protected)GGHHHSGAGKT peptide, the palmitic acid was conjugated to the side chain of the 10^{th} residue lysine, ensuring first that the FMOC protecting group on the 1^{st} residue serine was not removed in the standard coupling procedure. The deprotecting cocktail for the dde-protecting group of the lysine was prepared by dissolving 1.8 mmol $NH_2OH.HCl$ and 1.35 mmol Imidazole in 5 mL N-Methyl-2-pyrrolidone (NMP), sonicating until dissolved. Just before adding the solution to the resin, Dichloromethane

(DCM) was added in a 1:5 DCM to cocktail by volume proportion. The cocktail was then added to the resin and the solution was shaken for 3 hours to deprotect the side chain lysine. The solution was drained and washed with DCM and DMF. The palmitic acid was coupled to this free amine using the standard coupling cocktail described previously. After palmitic acid coupling, the FMOC of the serine was deprotected with 20% piperidine in DMF to leave a positively charged N-terminus.

After drying the resin under nitrogen, the peptide amphiphiles were then cleaved from the resin using a 95:2.5:2.5 by volume trifluoroacetic acid: triisopropylsilane: MilliQ water cleavage cocktail for 2 hours while shaking. The cleaved peptide amphiphiles were then precipitated through dropwise addition of the cleavage solution in a 50:50 by volume hexanes: -80 ºC diethyl ether solution. The peptide amphiphiles were dried under nitrogen and dissolved in water.

The peptide amphiphiles were purified using reverse-phase HPLC (Prominence, Shimadzu, Columbia, MD, USA) on a C8 column (Waters, Milford, MA, USA) at 50 ºC using acetonitrile and water with 0.1% formic acid as gradient mobile phases. The molecular weight of the products in the HPLC fractions were characterized by MALDI-TOF mass spectral analysis (Biflex III, Bruker, Billerica, MA, USA). The product-verified fractions were lyophilized and stored as powders at -20 ºC. The purity was analyzed using a similar gradient method on an Agilent 6130 LCMS system in the University of Chicago's Mass Spectrometry Facility, using a Waters column, C8, XBridge, 4.6 mm × 150 mm, 5 μm particle size, and 130 Å pore size. The purity was calculated by integrating the area under the peaks during the elution time and dividing the area of the product peak by the area of all peaks, excluding peaks that were artifacts of the method. The purity was confirmed to be greater than 95% for both PAs.

Finally, the PA micelles were fabricated through dissolving the lyophilized powder in MilliQ water at the desired concentration, heating at 70 °C for 1 hour on a mechanical shaker, and letting the solution cool down and equilibrate at room temperature for at least 2 hours before experimental use.

2.2.2 Critical Micelle Concentration (CMC) Determination

The CMC was calculated by marking an increase of fluorescence intensity, corresponding to an increased micelle concentration, of a dissolved dye that fluoresces in the presence of hydrophobic micelle cores. To execute this experiment, 1,6-diphenyl-1,3,5-hexatriene (DPH) dye was dissolved in tetrahydrofuran at a concentration of 100mM and then diluted in water to a final concentration of 1 μM. Each PA was dissolved in 1 μM DPH solution and serially diluted by half to range from 0.001 μM to 1000 μM, performed in triplicates for each PA. The dilutions were allowed to equilibrate for one hour while covered with aluminum foil at room temperature. They were then transferred to a 96-well plate in triplicates to minimize instrument error. Their fluorescence intensity was measured using a Tecan Infinite 200 plate reader (Mannedorf, Switzerland) with an excitation wavelength of 360 nm and an emission wavelength of 430 nm. The data were plotted with a log-transformed concentration and fit with two linear lines of best fit, one corresponding to the zero-slope portion and one fitting the data with increased fluorescence intensity. The CMC was identified as the intersection of these two fitted lines, approximating the inflection point of increased fluorescence intensity.

2.2.3 Negative-stain Transmission Electron Microscopy (TEM) Imaging

Carbon film 200 mesh copper grids were glow discharged with a Gatan Solarus plasma cleaning system for 30 s. They were then loaded with 3.5 μL of PAs for 1 minute, and then the excess was removed through blotting with filter paper. The grids were negatively stained with

0.75% uranyl formate for 45 s, blotted off to remove excess stain, and then were allowed to air dry before imaging. All transmission electron microscopy (TEM) imaging was performed on either the FEI Tecnai TF30 300 kV TEM (Hillsboro, OR, USA) or the FEI Tecnai Spirit 120 kV TEM (Hillsboro, OR, USA). The images were processed and measured digitally using ImageJ software, and the average dimensions were calculated from a sample size of at least 10 micelles.

2.2.4 Molybdenum Blue Assay for Analyzing Phosphate in Solution

To determine the amount of phosphate in solution, a spectrophotometric assay referred to as the molybdenum blue reaction was employed, which emits a blue color linearly proportional to the amount of phosphate present in solution. The reaction involves the following steps:

$$PO_4^{3-} + 12\ MoO_4^{2-} + 27\ H^+ \rightarrow H_3PO_4(MoO_3)_{12} + 12\ H_2O \quad (1)$$

$$H_3PMo(VI)_{12}O_{40} + \text{reductant} \rightarrow [H_4PMo(VI)_8Mo(V)_4O_{40}]^{3-}. \quad (2)$$

The first step consists of the reaction between phosphate, ammonium molybdate, and acid, producing a product that is then reduced in the second step to produce the final blue-colored product. Our procedure was modified from previous molybdenum blue assay designs.[68,69] For our procedure, the following reagents were prepared: 0.10 M ammonium molybdate (VI) tetrahydrate (ACS reagent, Acros Organics) in MilliQ water, 10%wt thiourea (99+%, for analysis, Acros Organics) in MilliQ water, 0.9 M sulfuric acid, and Na_2HPO_4 anhydrous (Fisher Scientific) in water at two concentrations of 1mM and 250 ppm phosphate. To conduct the assay for the calibration curve samples, 5 µL of ammonium molybdate, 10 µL of thiourea, and 5 µL of sulfuric acid were added in that order to 230 µL of a phosphate-containing solution with a concentration ranging from 0 to 50 ppm in MilliQ, diluted from the 250 ppm phosphate stock. Note that the reaction is catalyzed by acid, so the acid was added last and the time was recorded at this step to designate the start time of the reaction. The solution was vortexed and allowed to react for 45

minutes. Slightly before the reaction was completed, 75 µL of the molybdenum blue reaction solution was transferred in triplicates to a 96-well clear round-bottom plate. This was injected into a Tecan Infinite 200 plate reader (Mannedorf, Switzerland) so that it would be ready to be characterized precisely at the 45-minute mark. The spectrophotometric absorbance was measured at a wavelength of 700 nm and averaged between the three samples to minimize measurement error. The ammonium molybdate and phosphate stock solutions were recreated biweekly, to account for their shorter shelf life.

Each time this method was employed to derive the phosphate concentration of an unknown solution, a calibration curve with three samples of known phosphate concentration (0, 25, and 50 ppm) was created. A new curve was created each time to account for small fluctuations in absorbance depending on the age of reagents or time allowed to react. The data were fit with a linear line of best fit and were used the calculate the phosphate concentration of the unknown sample. The curve was rejected and recreated if the R-squared value was less than 0.99.

2.2.5 Analysis of pH-Dependent Phosphate Binding

The binding experiments consisted of combining PA and PO_4 solutions, adjusting the pH, physically separating the PA micelles from the solution with unbound phosphate, and analyzing the phosphate concentration of the filtrate. To perform a single measurement pH-dependent binding experiment, 62.5 µL of 1 mM Na_2HPO_4 stock was combined with 62.5 µL of a PA solution in MilliQ at a predetermined concentration to achieve the desired molar ratio of PA binding unit: PO_4, with a final phosphate concentration of 0.5mM for all binding experiments. Because C_{16}SGKGHhex has two binding units per molecule and C_{16}GGGhex only has one, the concentration of C_{16}SGKGHhex was half that of C_{16}GGGhex to achieve the same molar ratio to phosphate. Upon combining the solutions, the pH was adjusted to the desired pH condition using

minimal 0.25 M HCl and 0.25 M NaOH, vortexting between additions, and the pH was measured using a Fisher Scientific Accumet XL500 pH/ISE/Conductivity Benchtop Meter (Vernon Hills , IL, USA) and a Fisherbrand Accumet Micro Glass Mercury-Free Combination Electrode. Upon reaching the target pH, the PA/PO_4 solution was centrifuged at 9000 g^{-1} for 2 minutes to collect any viscous PA material that had accumulated on the side of the container, then transferred to a 1mL disposable pipette and filtered using a 13 mm 0.22 μm GHP Acrodisc syringe filter, collecting the filtrate sans PA in another vial. 75 μL of the filtrate was withdrawn and analyzed using proportional volumes of the spectrophotometric assay reagents (1.63 μL ammonium molybdate, 3.26 μL thiourea, and 1.63 μL sulfuric acid) and adhering to the rest of the assay protocol. For pH 2, 10, and 11 samples, the amount of added 0.25M NaOH and HCl for pH adjustment was recorded per sample, and the pH of each of the calibration point samples was adjusted to the same pH using an equivalent proportional volume of the NaOH and HCl that was added to the binding sample. The phosphate concentration of the assay sample was calculated using the calibration curve generated with each sample. The original phosphate concentration of the filtrate was then determined by accounting for the volume of the added spectrophotometric reagents which diluted the reading. This was repeated in duplicates or triplicates for each pH condition.

2.2.6 Analysis of Kinetics of Binding

This experiment was conducted similarly to the single measurement pH dependent binding experiments, but the total volume was increased to account for multiple samples being withdraw and multiple measurements taken. The total volume was calculated according to the following scheme: 125 μL * (number of samples) + 200 μL, with the last term ensuring that enough sample was retained. A solution of 5:1 ratio of C_{16}GGGhex to PO_4 at the desired volume was prepared such that the final concentration of PO_4 was 0.5 mM. The pH of the solution was adjusted using

minimal HCl and NaOH to the desired pH condition. At each time point, beginning from the moment the desired pH was attained, the pH of the sample was recorded using Hydrion pH paper and 125 µL of solution was withdrawn, filtered, and analyzed as described previously.

2.2.7 Analysis of Selectivity over Nitrate and Nitrite

Samples were prepared in MilliQ in molar ratios of 1:1:1:1, 2:1:1:1, and 3:1:1:1 of PA:PO_4:NO_3:NO_2 equivalent to 10 ppm PO_4. The pH was adjusted and measured as previously described, and the solutions were mixed for 30 minutes to ensure the samples reached equilibrium in the more dilute regime. The samples were filtered as previously described to partition out the PA, and the filtrate was analyzed using ion chromatography.

Ion chromatography was preformed using a Thermo Scientific Dionex ICS-5000+ equipped with a Dionex AS-DV autosampler and using a Dionex IonPac AS22 column (Product No 064141, Thermo Scientific, California, USA). The analysis was run using an eluent of 4.5 mM Sodium Carbonate and 1.4 mM Sodium Bicarbonate (Product No 063965 from Thermo Scientific, California, USA) and a Dionex AERS 500 Carbonate 4 mm Electrolutically Regenerated Suppressor (Product No 085029 from Thermo Scientific, California, USA).

2.2.8 Analysis of Cycles of Capture and Release

The capture and release method was designed to simulate usage conditions of filtration through a packed bed reactor, collecting the released phosphate at designated release intervals. To simulate this, a 520 µL solution of C_{16}GGGhex and PO_4 was prepared in a 5:1 ratio such that the final concentration was 0.5 mM. To capture the phosphate, the pH was adjusted to pH 6 as described previously and left to equilibrate in a shake plate at 200rpm for 30 minutes. 500 µL of this solution was transferred to the filter compartment of an Amicon Ultra 0.5 mL 3K MWCO centrifugal filter and centrifuged for 4 minutes at 9,000 g^{-1}. This filtrate was analyzed using the

spectroscopic assay as described previously. A new reclamation vial was switched out, and the retained PA was then washed with 200 µL Milli-Q water 6 times, centrifuging each time at the previous conditions, to ensure all unbound phosphate was removed from the dense PA suspension. The PA material was then recovered by inverting the filter compartment and collecting in a new collection vial by centrifuging at 1,000 g^{-1} for 10 minutes, or until all sample was recovered.

To perform the phosphate release and reclamation, 100µL of Milli-Q water was added to the filtration compartment and vortexed until well mixed with the PA. The now more dilute PA solution was transferred to a new binding analysis vial, and the total volume transferred was recorded. The volume of the recovered solution was raised to 480 µL using Milli-Q water, and the pH was adjusted to the desired release pH as previously described and left to equilibrate in a shake plate at 200rpm for 30 minutes. The amount of added acid and base was recorded. Upon reaching the target pH, Milli-Q water was added to reach a final volume of 500 µL. The released phosphate was then collected by transferring the solution to a centrifugal filter and centrifuging at 9,000 g^{-1} for 4 minutes. This filtrate was then analyzed using the spectrophotometric assay, adjusted for pH as previously described. The PA solution was washed as previously described. To prepare the solution for a recapture process, phosphate was added to the solution based on the amount of retained phosphate ions in the material as determined from the assay to obtain a 5:1 ratio of PA:PO_4 at a 0.5 mM concentration of PO_4 and a final volume of 500 µL. The solution was adjusted to pH 6, and the process was repeated as many times as desired.

2.2.9 Analysis of the Effect of NaCl on Binding and the Molybdenum Blue Assay

Samples were prepared in a 5:1 ratio of C_{16}GGGhex:PO_4 and varying NaCl concentrations such that the final PO_4 concentration was 0.5 mM and the final NaCl concentrations ranged from 2 µM to 40 µM. The samples were then adjusted to pH 6, filtered, and analyzed as described

previously. To assess whether increased NaCl influences the reading of this assay, molybdenum blue calibration curves were constructed with varying amounts of NaCl added to match the final NaCl concentrations tested in the binding experiments. These curves were then compared to a standardized curve with no NaCl added.

2.2.10 Simulation Model and Force Field Parameters

Atomistic Model: The simulations used the GROningen MAchine for Chemical Simulations (GROMACS)[70] package and the ABF enhanced sampling methods implemented in SSAGES.[71] The PAs were modeled using the CHARMM forcefield[72] and water was modeled using the TIP3P model.[73] Custom force field parameters used for phosphate ions are listed in Tables 2.1-2.4. The Lorentz-Berthelot mixing rule was used for unlike non-bonded interactions involving phosphate atoms. Nonbonded interactions were calculated using a 12 Å cutoff distance. Long-range electrostatic interactions were handled using fast smooth Particle-Mesh Ewald (SPME)[74] with a 0.12 nm Fourier spacing. Covalent bonds involving hydrogens were constrained using the LINCS algorithm.[75] All simulations were integrated using the leap-frog algorithm with a 2-fs timestep. All temperature-coupling used was Nosé–Hoover thermostat with a time constant of 0.1 ps used to maintain the temperature at 300 K.

Phosphate Force Field Parameters: Atom types in phosphate were assigned in the following way. In $H_2PO_4^-$, the phosphate atom is PMHP; the unprotonated oxygen atom is OPMH; OHMH and HOMH are the hydrogen atoms and the protonated oxygen atoms, respectively. In HPO_4^{2-}, the phosphate atom is PDHP; the unprotonated oxygen atom is OPDH; OHDH and HODH are the hydrogen atoms and the protonated oxygen atoms, respectively.

The nonbonded interactions include Lennard-Jones interactions and Coulombic interactions. For atoms i and j, their nonbonded interaction is:

$$u_{nb}(r_{ij}) = 4\epsilon_{ij}\left[\left(\frac{\sigma_{ij}}{r_{ij}}\right)^{12} - \left(\frac{\sigma_{ij}}{r_{ij}}\right)^{6}\right] + \frac{q_i q_j}{4\pi\varepsilon_0 r_{ij}}, \quad (1)$$

where r_{ij} is the separation distance between atoms i and j, σ_{ij} is the Lennard-Jones diameter, σ_{ij} is the Lennard-Jones interaction strength, ε_0 is the vacuum permittivity. q_i and q_j are the partial charges of atoms i and j. See Table 2.1 for nonbonded interaction parameters.

Table 2.1: Nonbonded interaction potential parameters for phosphate atoms.

atom	m	σ_{ii}	ϵ_{ii}	q
PMHP	30.974	0.3296	0.6904	1.17
OPMH	15.999	0.2494	0.418	-
OHMH	15.999	0.2672	0.418	-
HOMH	1.008	0.04	0.192	0.28
PDHP	30.974	0.3296	0.6904	1.2
OPDH	15.999	0.2494	0.418	-
OHDH	15.999	0.2494	0.418	-
HODH	1.008	0.04	0.192	0.34

The 1-2 bonded atoms interact via a harmonic bonding potential in the form:

$$u_{bond}(r_{ij}) = \frac{k_{bond}}{2}\left(r_{ij} - {r_{ij}}^{(0)}\right)^2, \quad \textbf{(2)}$$

where r_{ij} is the separation distance between atoms i and j, k_{bond} is the force constant and ${r_{ij}}^{(0)}$ is the equilibrium bond length. The bonding interaction parameters are listed in Table 2.2.

Table 2.2: Bonding potential parameters for phosphate atoms.

bond	$r_{ij}^{(0)}$(nm)	k_{bond}
PMHP-	0.154	485344
PMHP-	0.167	198322
OHMH-	0.0965	456056
PDHP-	0.154	485344
PDHP-	0.167	198322
OHDH-	0.0965	456056

The 1-2-3 bonded atoms interact via a harmonic bending potential in the form:

$$u_{bend}(\theta_{ijk}) = k_{bend}\left(\theta_{ijk} - \theta_{ijk}^{(0)}\right)^2, \quad \textbf{(3)}$$

where k_{bend} is the force constant, θ_{ijk} is the angle between united atoms i, j, and k, and $\theta_{ijk}^{(0)}$ is the equilibrium angle. The bending interaction parameters are listed in Table 2.3.

Table 2.3: Bending potential parameters for polymer atoms.

Angle	$\theta_{ijk}^{(0)}$(deg)	k_{bend}
OPMH-PMHP-	114.23°	1004
OPMH-PMHP-	104.1°	827.6
PMHP-OHMH-	107.9°	836.8
OPDH-PDHP-	120°	1004
OPDH-PDHP-	108.7°	827.6
OHDH-PDHP-	102.9°	827.6
PDHP-OHDH-	107.9°	836.8

The torsional potentials for 1-2-3-4 bonded united atoms take the form:

$$u_{tors}(\phi_{ijkl}) = k_{\phi}\left[1 + \cos\left(n\,\phi_{ijkl} - \phi_{ijkl}^{(0)}\right)\right] \quad \textbf{(4)}$$

where k_ϕ is the coefficient and ϕ_{ijkl} is the dihedral angle defined by atoms $i,\ j,\ k$, and l. n is the integer multiplicity and ${\phi_{ijkl}}^{(0)}$ is a refence dihedral angle. The torsional interaction parameters are listed in Table 2.4.

Table 2.4: Torsional interaction parameters for polymer atoms.

dihedral	${\phi_{ijkl}}^{(0)}$(deg)	k_ϕ ($\frac{\text{kJ}}{\text{mol}}$)	n
OPMH-PMHP-OHMH-	0°	1.26	3
OHDH-PDHP-OHDH-	0°	1.26	3
OPDH-PDHP-OPDH-	0°	1.26	3
HODH-OHDH-PDHP-	0°	1.26	3

1.

2.2.11 Simulations of Phosphate Binding to Single-Chain

Simulation Protocols**:** For the unbiased molecular dynamics simulations, a single C_{16}GGGhex chain and a single phosphate ion were placed in a cubic box (7 nm side length). At each pH condition, the phosphate ion was initialized at 9 different starting positions relative to the PA. For each replica, 20 ns of simulation under NVT ensemble in vacuum was performed to obtain a PA-phosphate bound structure. Then the system was solvated in water and a 10-ns NVT simulation for equilibration. Subsequently, another 10-ns MD trajectory under NVT ensemble was collected for analysis.

For ABF advanced sampling, two distance CVs identified in the cluster analysis, d_{SGAGKT} and d_{GGG}, were used to describe single-chain binding. Specifically, d_{SGAGKT} is defined as the distance between the center of mass of the phosphate and the center of mass of the following atoms:{Backbone N on 8GLY, backbone N on 9LYS, sidechain N on 9LYS, backbone N on 10THR, sidechain O on 10THR}. d_{GGG} is defined as the distance between the center of mass of the phosphate and the center of mass of the following atoms:{Backbone N on 2GLY, backbone N

on 3GLY, O on 3GLY, backbone N on 5SER, and sidechain O on 5SER}. Note that the C_{16} region was counted as the first residue, and the following GGGSGAGKT peptide corresponded to residues 2-10. Each CV was bound within the interval [0.05 nm, 2.0 nm] and divided into 50 bins. Each ABF simulation used 4 parallel walkers under NVT ensemble. Restraints were placed foreach CV at values of 0.0 nm and 2.5 nm with a spring constant of 500 kJ mol^{-1} nm^{-2} to ensure that the configurations explored remained in the CV space of interest. For each ABF bin, a minimum visit of 400 was required before forces are estimated. ABF was carried out and output monitored at intervals of 40 ns until the free energy features no longer changed between the two most recent outputs, resulting in 240 ns total simulation time per walker for both pH conditions.

Cluster Analysis**:** Cluster analysis was employed to identify the most frequently occurring PA-phosphate bound configurations. At each pH condition, snapshots from all nine trajectories were first rotationally and translationally aligned based on the peptide coordinates. Then the aligned snapshots were analyzed using the GROMACS cluster tool, using the gromos clustering algorithm[76] with a cutoff of 0.27 nm. The snapshots are clustered based on the peptide coordinates.

2.2.12 Simulations of Phosphate Binding to Peptide Amphiphile Micelle

Starting Configuration**:** The starting configuration for the PAM simulation was generated using a procedure in existing literature.[77] Briefly, nine PA molecules were packed in the *x*-*y* plane with the C_{16} tail pointing inwards, with 40° angle between adjacent chains. Then 24 layers were stacked in the *z*-direction with 20° offset and 5 Å distance between layers, resulting 216 PAs in total in the simulation box. Forty phosphate ions were inserted at random positions avoiding position overlap with the PA molecules. The simulation box was 16 nm in *x* and *y* direction (periodic) and 12 nm in *z* direction (non-periodic). The simulation box was solvated using the GROMACS solvate tool. Sodium (Na^+) or chloride (Cl^-) ions were added to neutralize the system.

Simulation Protocol**:** The starting configuration was energy-minimized using a steepest descent algorithm with a force tolerance of 10 kJ mol^{-1} $nm^{-1}$and a step size of 0.01 nm. The minimized configuration was then equilibrated under NVT ensemble for 4 ns. During this NVT simulation, for each PA chain, the position of the first carbon atom (closest to the micelle center) was restrained using a harmonic potential with a spring constant of 1000 kJ mol^{-1} nm^{-1} in each direction. Subsequently, the position restraint was removed, and the system was simulated for 50 ns under NPT ensemble, where the pressure in the *x*-*y* direction and the pressure in the *z* direction were coupled independently. For each direction, the pressure was maintained at 1.0 bar using Berendsen barostat with a time constant of 1.0 ps. Figure 2.5C displays the time evolution of the solvent accessible surface area (SASA) over the total 50-ns NPT trajectory, in which the SASA are shown to stabilize by 30 ns. As a result, the last 20 ns of MD trajectory was used for analysis.

Analysis**:** For the hydrogen bond (H-bond) analysis, the GROMACS hbond tool was used to identify H-bonds formed between PA chains and phosphate ions. The H-bond criterion used a distance cutoff of 0.35 nm and an angle cutoff of 30°. Note that the GROMACS hbond tool uses the hydrogen-donor-acceptor angle instead of the donor-hydrogen-acceptor angle. The SASA was computed using the GROMACS sasa tool.[78] The entire micelle was selected for the SASA calculation.

2.3 Results and Discussion

2.3.1 Design of the Peptide Amphiphile Prototype Material

With strategic design from the molecular level up, each PA molecule can be individually tuned to dictate its bulk self-assembled and phosphate binding properties (Figure 2.1). Here, we designed two different molecules to evaluate, denoted C_{16}GGGhex and C_{16}SGKGHhex, each consisting of three key design regions intended to optimize both functionalities: (1) producing

wormlike micelles to create an entangled network and (2) optimizing phosphate binding performance. Each of these molecules was synthesized using FMOC solid phase peptide synthesis with precise monodisperse control and promise in scalability.[79]

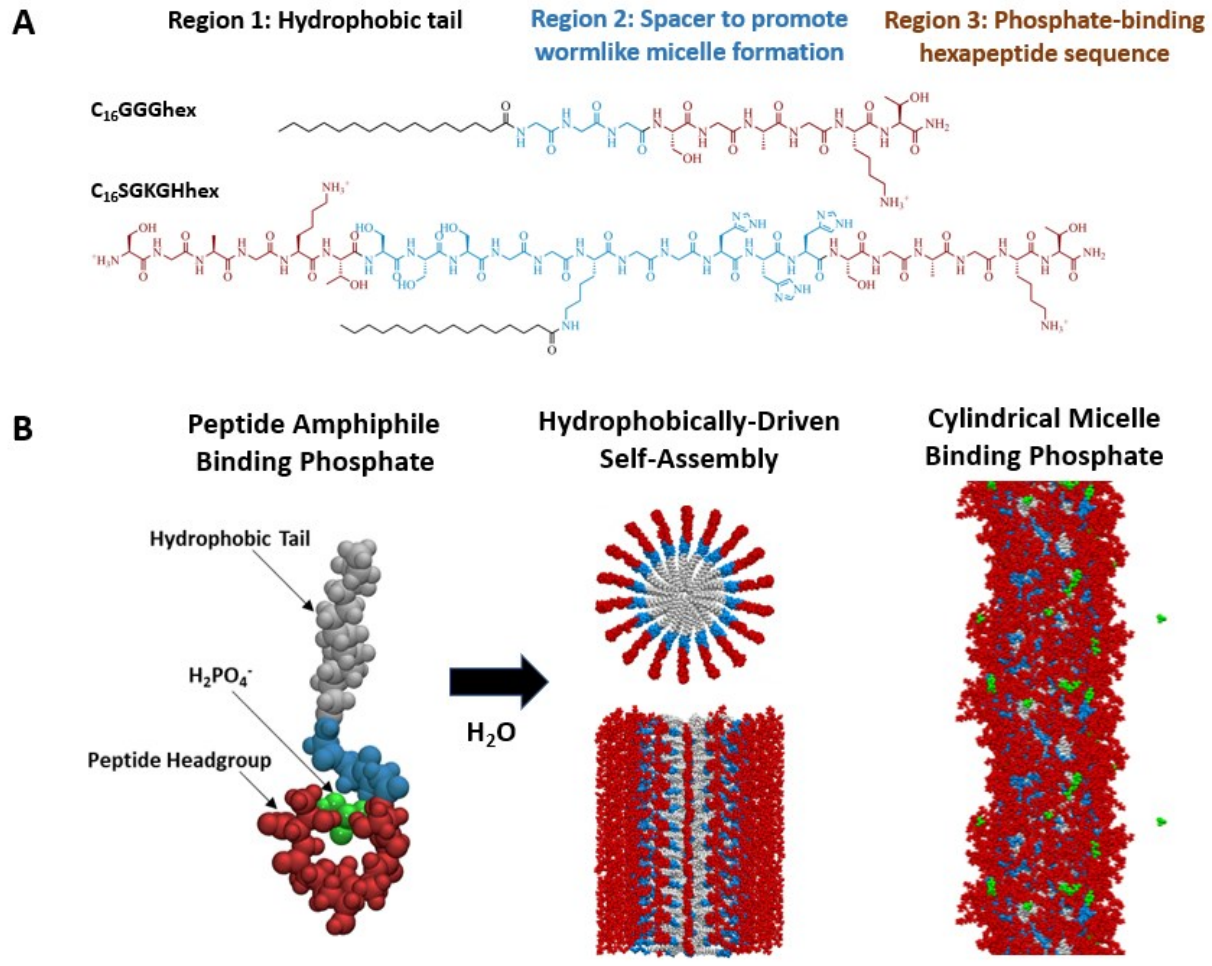

Figure 2.1. (A) PAs denoted C_{16}GGGhex andC_{16}SGKGHhex. (B) Simulation snapshots of C_{16}GGGhex. On the left, an individual PA binds to a phosphate ion in the peptide headgroup through utilizing the P-loop mechanism of hydrogen bonds of the peptide backbone and nested cavity promoted by the side chain lysine. When submerged in water, the PAs spontaneously self-assemble into a micelle to shield the cores from the aqueous solution (middle). The PA micelle binds to phosphate in the corona (right).

The critical binding moiety of our material platform (Region 3) is the protein-derived phosphate-binding sequence that protrudes into the aqueous environment, coating the surface area of the entangled wormlike micelle network with readily accessible binding sites for phosphate.

The phosphate binding of proteins has been thoroughly studied in other works,[80,81] but here we extract a specific well-known sequence to molecularly engineer a new system for targeted harvesting of phosphate in a self-assembled network. The binding sequence we chose, namely SGAGKT, is taken from the P-loop motif which is common in phosphate-binding proteins. It consists of a sequence of GXXXXGK[S,T], where X is any amino acid residue and the final residue is either serine or threonine.[48] The P-loop motif stabilizes the phosphate group of proteins, commonly of ATP or GTP, by creating a nest around the phosphate of hydrogen bonds from the amines in the P-loop backbone and utilizing the positively charged lysine side chain, as depicted in Figure 2.1. We selected this specific SGAGKT hexapeptide binding sequence because it was a commonly repeated motif among myosin-heavy chains, as opposed to other P-loop sequences that had more variation between proteins,[48] and it was previously synthesized and found to bind phosphate in a pH-dependent manner.[56,82]

Equally essential to our material design is Region 1 of the PA, the "tail" which drives the PAs to self-assemble according to the hydrophobic effect, driving the hydrophilic peptide "headgroup" to be systematically displayed to the environment in the micelle corona. For both molecules, we selected the tail to be palmitic acid (C_{16}) for its use in previous systems that adopted a wormlike micellar assembly.[11]

Finally, we incorporated Region 2 of our PAs, which we call the "spacer" here, for two purposes: i) to extend the binding moiety further into the aqueous solution and thus make the binding pocket more accessible, and ii) to produce intramolecular hydrogen bonding that in turn induces wormlike micelle formation, the desired architecture for our entangled material design. For the latter purpose, we tested two designs. The "GGG" in the name C_{16}GGGhex corresponds to three glycine residues between the tail and the binding sequence, which have been shown

previously to produce hydrogen bonded beta sheets that encourage the assembly into a wormlike micellar structure.[83] Similarly, the "SGKGH" notation for C_{16}SGKGHhex corresponds to serine, glycine, and histidine residues on either side of the lysine, whose side chain amine is used to construct the branched PA junction through its direct conjugation to the tail. This double-headed branched design, without the hexapeptide, was previously shown to promote crosslinked, self-supported gelation at pH > 6.5 due to hydrogen bonding between the hydroxyl groups of the serine residues and the deprotonated imidazole side chains of the histidine residues.[11] It was chosen here with the intent to further increase the robustness of our entangled wormlike micelle network through these engineered physical crosslinks. Thus, by keeping PA design Regions 1 and 3 constant, we could directly evaluate the impact of each strategy for hydrogen bonding in Region 2 on the two overall design aims of (1) producing a robust wormlike micelle network and (2) optimizing phosphate binding performance.

2.3.2 Analysis of Self-Assembled Micelle Properties

To characterize our capture-and-release material, we first analyzed the self-assembly properties of the PAs. To begin, we measured the critical micelle concentration (CMC), that is, the concentration at which the PAs begin to self-assemble. The CMCs were 8.43 μM and 130.1 μM for C_{16}GGGhex and C_{16}SGKGHhex, respectively (Figure A.3). These values are in the expected range for PA molecules, but this ten-fold difference is noteworthy and is explained by the packing parameter, *P*, for these amphiphilic molecules. *P* relates the chemistry of the molecule, most notably the area of the headgroup, to the packed self-assembled state (see SI for further discussion).[84] In our binding materials, the lower CMC value of C_{16}GGGhex is advantageous because it corresponds to a lower concentration of unimer PAs in solution when the system is assembled above the CMC. To minimize the ratio of unimer to assembled micelle and to ensure

that we are always working with assembled materials, we conducted all future experiments at a concentration of PA at least 10 times greater than the value of the CMC, unless otherwise noted.

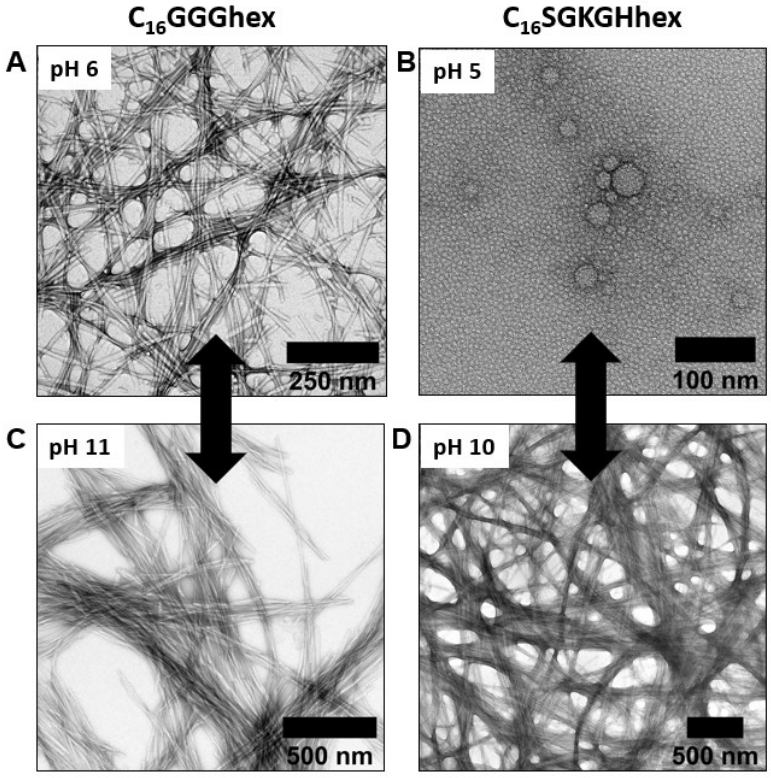

Figure 2.2. TEM images of C_{16}GGGhex and C_{16}SGKGHhex at neutral and high pH values. Both systems exhibit a reversible pH micelle transition when switching from neutral/acidic to high pH. C_{16}GGGhex clumps together at high pH, while C_{16}SGKGHhex assembled into spheres at pH 5 and clumped wormlike micelles at high pH.

We performed negative stain transmission electron microscopy (TEM) to visualize the micellar architectures and calculate the length scales of the micelle assemblies. For each system, we see a pH dependence of micelle formation. For C_{16}GGGhex, we observe entangled wormlike micelles with an average diameter of 11.5 nm that extend tens of microns in length at neutral pH (Figure 2.2A).[85] This is the desired micelle architecture for our capture and release material to provide a solid support through which phosphate-rich solution can flow. At high pH (Figure 2.2C), we observe that the wormlike micelles cluster together. This phenomenon is likely due to the lysine

side chain being deprotonated, resulting in assemblies that are less soluble and then stabilize through aggregation. Overall, C_{16}GGGhex is well-suited to form a dense suspension for the retention and release of phosphate.

For C_{16}SGKGHhex, we also observe reversible pH dependence on micelle formation. At pH 5 and below, C_{16}SGKGHhex assembles into spherical micelles with a diameter 7.2 nm (Figure 2.2B), but by pH 10, it has transitioned into wormlike micelles that are also clumped together and extend for tens of microns (Figure 2.2D). This transition from sphere to wormlike micelles has been noted previously for pH-dependent materials.[86,87] For C_{16}SGKGHhex, the effective headgroup area decreases when the histidine imidazole groups are deprotonated at high pH, reversibly pushing the assembly to be most stabilized as wormlike micelles. Overall, this PA micelle platform showcases the unique tunability of small molecular variations on microscale properties, and though it does not produce the desired entangled network for the full pH range, it will allow us to determine how this micelle shape transition affects binding.

2.3.3 Analysis of Fundamental Phosphate-Binding Properties

We evaluated and compared the phosphate binding functionality of the two PA micelles. We employed a spectrophotometric assay to quantify phosphate binding which emits a blue color linearly proportional to the amount of phosphate in solution.[68,69] To perform the binding process, we combined the phosphate and PA at the desired concentrations, adjusted the pH using minimal HCl and NaOH, physically separated the PA from the unbound phosphate in solution, and then performed the spectrophotometric assay on the filtrate containing unbound phosphate. The PO_4 feed concentration was chosen to be 0.5mM (47.5ppm) for all experiments to simulate a comparable phosphate concentration to that of municipal wastewater influent streams.[88] For this preliminary fundamental testing, we evaluated the phosphate binding dependence on three factors:

(i) the pH of the solution, (ii) the ratio of the hexapeptide binding unit to phosphate, and (iii) length of time permitted to bind.

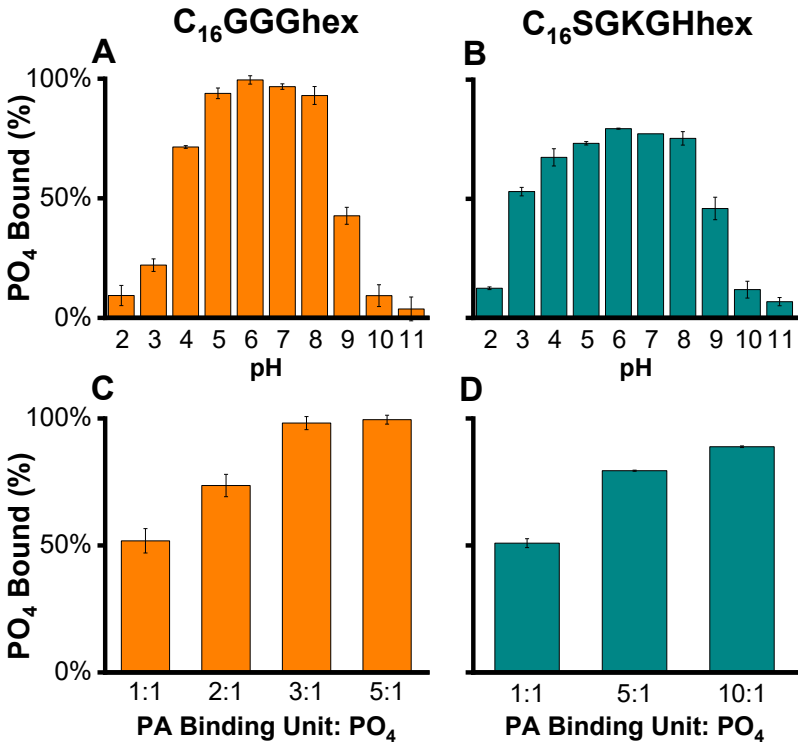

Figure 2.3. (A-B) pH-dependent phosphate binding of the PA micelles (A) C_{16}GGGhex and (B) C_{16}SGKGHhex at a molar ratio of 5:1 PA binding unit: PO_4 and a PO_4 feed concentration of 0.5 mM (47.5 ppm). For C_{16}GGGhex, essentially 100% of phosphate (within measurement error) was bound to the micelle at pH 6, representing the ideal "capture" conditions, while only 5% and 10% of PO_4 was bound at pH 2 and 10, respectively, becoming ideal "release" conditions. For C_{16}SGKGHhex, a similar trend of maximum and minimum binding was observed, although complete binding was not achieved. (C-D) Phosphate binding at pH 6 when the ratio of PA binding unit: PO_4 was varied while keeping the concentration of PO_4 constant at 0.5 mM. (C) For C_{16}GGGhex, 92% and 100% of binding were achieved at a ratio of 3:1 and 5:1 PA binding unit: PO_4, respectively. (D) For C_{16}SGKGHhex, only 89% binding was achieved even when the ratio was increased to 10:1.

The results in Figure 2.3 depict how phosphate binding depends on pH and the ratio of binding unit to phosphate. For both C_{16}GGGhex and C_{16}SGKGHhex, the optimal phosphate binding occurs at pH 6, with minimal binding occurring at low and high pH extremes. Intuitively, as the ratio of PA to phosphate increases, the amount of captured phosphate in solution also

increases. C_{16}GGGhex achieved phosphate capture of 92% and 100% at pH 6 and a molar ratio of 3:1 and 5:1 PA binding unit to phosphate, respectively. Comparatively, C_{16}SGKGHhex only achieved 79% binding at identical 5:1 ratio conditions. Additionally, increasing the ratio further to 10:1 did not achieve the complete phosphate capture as exhibited by C_{16}GGGhex. The superior performance of C_{16}GGGhex places this material on par to meet the strict phosphate effluent limits, which can be as low as 0.1 mg/L of phosphorus.[35]

The kinetics experiments (see Figure A.11) demonstrated that C_{16}GGGhex sequestered and released phosphate within seconds to minutes of reaching the target pH, and the material maintains its unbound or bound state as long as the pH remains constant. This rapid succession between capture and release states eliminates any need for equilibrating binding time, an additional process design advantage. In light of these binding results, we chose to continue additional characterization only for the superiorly performing PA micelle, C_{16}GGGhex, at a ratio of 5:1 PA:PO_4 with a capture pH of 6 and two potential release pH's of 2 and 11.

The superior binding ability of C_{16}GGGhex over C_{16}SGKGHhex illuminates three interesting binding implications. First, it appears that binding is notably impacted by the entire PA molecule design, even though both designs utilize the same binding moiety. Second, binding is not maximized by increasing charged interactions. C_{16}SGKGHhex has a +6 charge at neutral pH (from 3 histidines, 2 lysines, and 1 amine N-terminus), while C_{16}GGGhex only has a charge of +1. Nevertheless, C_{16}GGGhex achieves maximal binding of the anion, presumably from superiorly employing the P-loop binding mechanism for targeted capture. Third, binding is achieved by both spherical and wormlike micelle architectures, with no notable differences in performance. C_{16}SGKGHhex transitions from spheres to worms, but the binding profile follows a comparable trend as C_{16}GGGhex.

The most notable implication, however, was that the binding properties appear to be significantly impacted by the self-assembled state of the PAs compared to unassembled hexapeptides not conjugated to a tail. Contrary to the results of our micelle material, namely maximal binding at pH 6 and minimal binding as pH increases, previous experimental studies of the free peptide observed the opposite, with highest phosphate binding at high pH and minimal binding at and below pH 6.[32] A simulation study on the same peptide, in its lysine-protonated, zwitterionic state, confirmed that binding with HPO_4^{2-} is favored over H_2PO_4.[89] Moreover, as the pH rises above the pK_a of lysine sidechain at 10.5, Bianchi et al. observed that the unprotonated lysine side chain had an important role in wrapping around the phosphate to stabilize the bound complex. These works combined indicate that both protonation states of the free hexapeptide stabilize HPO_4^{2-} by forming a nested cavity and incorporating the side chain, performing the P-loop mechanism for phosphate binding.

We hypothesize that the assembled structure induces a pH shift in the binding trigger, fundamentally altering the capture and release functionality of the peptide. This is supported by the results of our simulations. The TEM images at high pH for both PAs already alluded to an intriguing macroscopic phenomenon, namely the spontaneous bundling of wormlike micelles correlated to deprotonation of lysine, that could feasibly impact phosphate binding. We propose that while the free peptide is unconstrained and able to adopt any conformation to stabilize binding of the phosphate ion at the full pH range, the peptide in our system, which already is more constrained in the micelle, becomes even more confined as pH rises and approaches the pK_a of lysine. As the lysine charges in the headgroup are neutralized and no longer repel each other, the micelle headgroup collapses and thereby eradicates any conformational freedom that previously allowed the free peptides to sequester the phosphate ions. The collapse of micelle coronae is later

quantitatively confirmed by our simulations. Therefore, although previous results show that high pH is the optimal binding state for this peptide, our self-assembled micelle system distorts the peptide binding conformation within each micelle, eliminates further conformational freedom by the micelles collapsing together upon each other, and fundamentally alters the binding ability at high pH.

Interestingly, we do not simply observe zero binding at the full pH range, as would be expected in light of the collapsed micelle morphology at high pH; instead, we see a pH shift of binding. Whereas other systems observed decreased-to-no binding below pH 6, we observe pH 6 as our maximal binding condition, with binding occurring in decreased efficacy until reaching pH 2. As our simulation results later confirm, phosphate is bound at this pH condition by the densely packed, positively charged headgroup in the micelle corona that attracts and conformationally stabilizes the negatively charged $H_2PO_4^-$ through nested hydrogen bonding. Not only is this binding pH shift induced by peptide aggregation scientifically intriguing and useful for informing future material designs, but it also has beneficial implications for resource reclamation. It is much more convenient to operate the phosphate collection conditions near the equilibrium pH of the system, which rests around neutral pH, and to perform the release conditions at the more unstable pH extremes, compared to vice versa. Overall, this system proved to capture phosphate completely and release phosphate at low and high pH values within minutes, while maintaining reversible structural stability to facilitate practical phosphate reclamation, which we were positioned to evaluate next.

2.3.4 Simulation Results Elucidate Binding Properties

To investigate the nanoscale mechanisms for the pH shift, we applied unbiased molecular dynamics (MD) simulations and the adaptive biasing force (ABF) enhanced sampling method [71,90]

to study phosphate binding of both the unimer and self-assembled C_{16}GGGhex at pH 6 and 11. The pH states are represented by the differing protonation states of the phosphate ion and the PA lysine sidechain, with pH 6 consisting of phosphate as $H_2PO_4^-$ and a protonated lysine amine, and pH 11 consisting of phosphate as HPO_4^{2-} and a deprotonated lysine amine. We studied the unimer PA first to determine whether the molecular alterations of the PA were the cause of the pH binding shift. Then we tested the assembled micelle system to further examine how binding is impacted by a dense, assembled peptide environment.

2.3.4.1 Phosphate-binding to Unimer PA

Compared to the free hexapeptide with natural C and N termini, the hexapeptide in the PA is conjugated with three additional glycine residues on the N terminal and is amidated on its C terminal, which could likely disrupt binding behavior compared to that of the free peptide. To determine this, we screened the bound PA-phosphate structures using unbiased MD. For each pH condition, 9 unbiased MD trajectories with different starting configurations were collected. Snapshots were collected every 10 ps for a total of 9009 snapshots for each pH condition. The snapshots were rotationally and translationally aligned by the peptide coordinates and were subsequently analyzed using the GROningen MAchine for Chemical Simulations (GROMACS) cluster tool.[70,76] The unbiased MD information was later used to define collective variables (CVs) to describe the system dynamics, which were then used in ABF enhanced sampling simulations to study the thermodynamics of binding at each pH condition.

For each pH condition, the phosphate interacted with the PA through various mechanisms, with the top five most commonly observed clusters presented in Figure 2.4A. At pH 6, phosphate was found to be bound only in the third cluster and unbound in the other clusters shown. In contrast, at pH 11, the phosphate was bound by C_{16}GGGhex in all of the top five most common clusters,

but the binding was stabilized at multiple locations, some of which included the GGG spacer in addition to the hexapeptide. In regards to observing the proposed P-loop mechanism of binding, we identified several clusters at both pH's in which the phosphate was surrounded by a 3-pronged "claw" formed by the hexapeptide backbone and its lysine side chain. This is consistent with the previously studied "nested cavity" P-loop mechanism for binding. These results agree with previous characterizations in that the hexapeptide prefers to bind phosphate at high pH rather than at low pH, and indicate that the physics built into our models are consistent with past reports for single molecules.

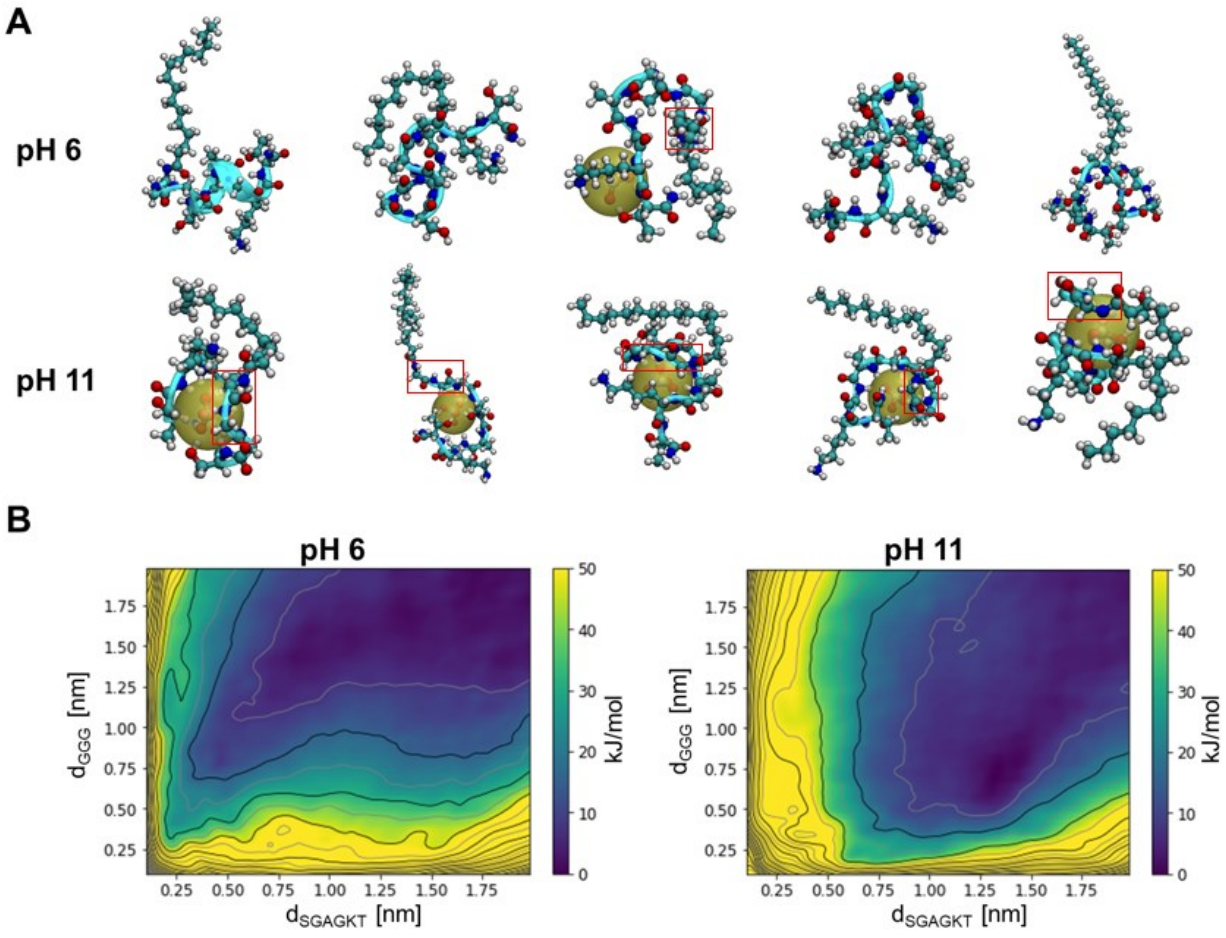

Figure 2.4. Single-chain binding simulations of C_{16}GGGhex show that binding is preferred at pH 11. (A) Snapshots of the top five populated clusters obtained in unbiased MD simulations. Populations of clusters decrease from left to right. The snapshots reveal the GGG spacer (boxed

in red) and hexapeptide are the two major regions of phosphate binding along the PA chain. (B) Free energy surface obtained via ABF sampling for single-chain PA binding to one phosphate. At pH 6, free energy is lowest for the unbound state (upper right corner). At pH 11, a bound state at d_{SGAGKT}=1.34nm, d_{GGG}=0.74nm is preferred with a binding free energy of -2.8 kJ/mol.

These snapshots also highlight that the spacers, incorporated into the molecular design to tune the micellar architecture, are not passive participants in binding but rather play an active role in stabilizing the phosphate. To qualify this phenomenon further, we calculated free energy surfaces in terms of two distance CV's to characterize binding of the unimer PA to phosphate: (1) d_{SGAGKT}, distance from the phosphate to the center of the 3-prong SGAGKT binding pocket; and (2) d_{GGG}, distance from the phosphate to the center of the GGG binding region (additional details provided in SI). We used these two CVs to perform ABF simulations to calculate the free energy landscape of one phosphate ion binding to a unimer PA at each pH condition. The results are shown in Figure 2.4B.

Our simulations confirm that phosphate is unbound at pH 6 and that it binds to the unimer PA utilizing the GGG spacer in addition to the hexapeptide. For pH 6, the free energy minimum, corresponding to the most stable binding state, is located at the top right corner of the free energy surface. This location corresponds to a phosphate ion far from both binding regions of the PA, simply stable in aqueous solution, suggesting that C_{16}GGGhex fails to sequester phosphate at pH 6. At pH 11, however, a minimum is found at d_{SGAGKT}=1.34, d_{GGG}=0.74 with a free energy difference of -2.8 kJ/mol with respect to the unbound state. This free energy minimum occurs at low d_{GGG} values, suggesting that interaction with the GGG linker is important for phosphate binding to the PA at pH 11. The free energy results confirm the finding that, unlike phosphate-binding to the SGAGKT hexapeptide, phosphate-binding to this PA exhibits more flexible binding structures, where the bound phosphate can interact with both the spacer and hexapeptide regions.

2.3.4.2 Phosphate-binding to Peptide Amphiphile Micelles

Having verified that the molecular alterations did not shift the pH binding conditions of the unimer PA, we simulated a micelle system to probe how the densely packed self-assembled environment impacts binding. We used unbiased MD simulations to characterize the phosphate binding behaviors of the micelle at an approximate PA:PO_4 ratio of 5:1. For each pH condition, 40 phosphate and 216 PA chains were simulated in water. Sodium (Na^+) or chloride (Cl^-) ions were added to neutralize the simulation box. The last 20-ns of the 50-ns MD trajectory under an isothermal-isobaric ensemble were used for analysis (details in SI). The simulated micelle was periodic along its cylindrical axis, which is aligned in the z-direction.

Our micelle simulations confirm the experimental shift in binding pH that is induced when the PA molecules systematically self-assemble. We corroborated this simulated binding shift using three complementary approaches: a histogram analysis of the radial distance of the phosphate to the micelle core, a potential of mean force (PMF) estimation, and a hydrogen bond (H-bond) analysis. Visually, we observe in Figure 2.5A two top-down snapshots of the simulated system, depicting the majority of phosphate ions being bound at pH 6, while most phosphate ions were unbound at pH 11. The visual analysis was further corroborated using a histogram of the radial distance of the phosphate ions to the micelle core (Figure 2.5B). These distances were then compared to the distance to the possible PA binding sites that were observed in the single-molecule PA analysis, namely the hexapeptide and the GGG spacer. Indeed, at pH 11, the distance of the phosphate to the center of the micelle was not localized anywhere, signifying an unbound state. But for pH 6, the majority of phosphate ions were located at the same distance from the core as the hexapeptide sequence, confirming localized binding to the hexapeptide.

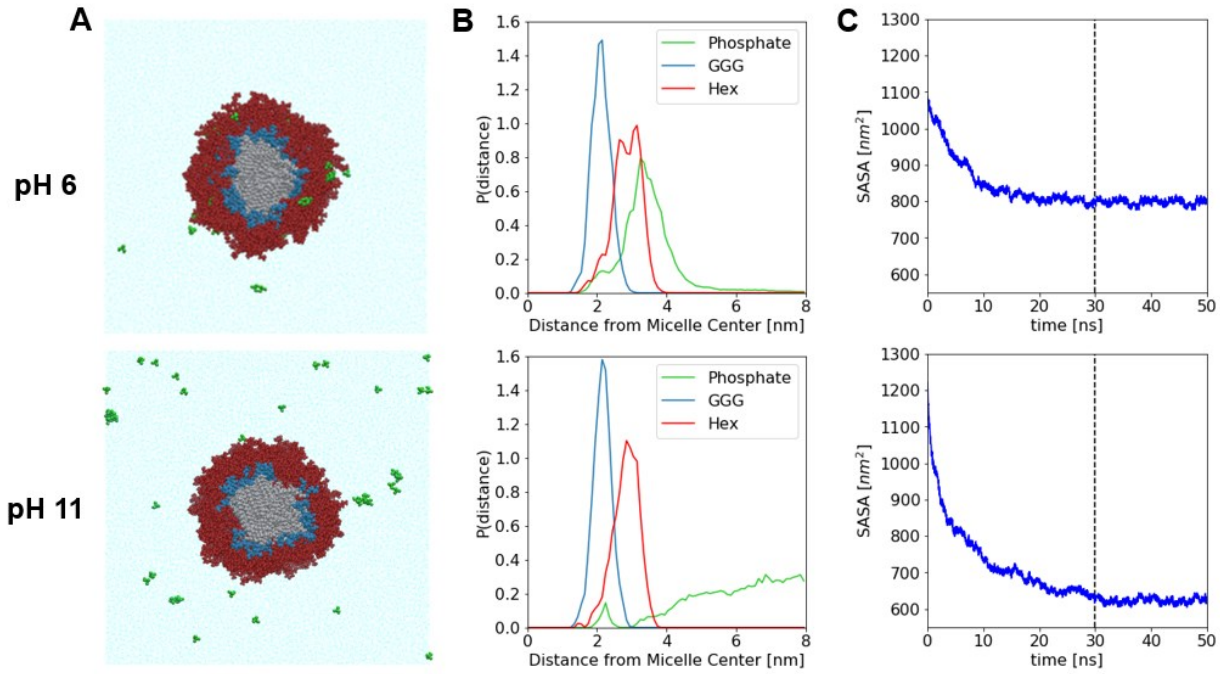

Figure 2.5. Simulations of phosphate binding to the C_{16}GGGhex micelle at pH 6 and 11. (A) Top-down snapshots of the simulated micelles at the end of the production run. (B) Normalized histograms of radial position from the micelle central axis for different components in the systems. The GGG spacer is noted as 'GGG' and the SGAGKT hexapeptide as 'Hex' in the legend. (C) Solvent-accessible surface area (SASA) of the micelle as a function of simulation time. The dash lines indicate the start of the time-averaging interval. The average SASA values are 798 ± 9 $nm^2$and 623 ± 8 nm^2 at pH 6 and 11, respectively.

The potential of mean force (PMF) offers insight into the free energy of binding of phosphate to the micelle compared to the unimer PA, with a lower free energy signifying a more stabilized bound state. The PMF along the radial CV was estimated by computing the Boltzmann inversion on the corresponding probability distribution via the equation $PMF(r) = kTln(P(r))$, where k is the Boltzmann constant and T is the temperature. Here, the PMF was computed as a function of distance from the micelle center, and $P(r)$ is the normalized histogram of the radial position of phosphate ions. From the PMF results (Figure A.14), we estimated that the PMF for a phosphate to bind to the micelle at pH 6 was -11.7 kJ/mol, which is lower by a factor of four than the binding free energy for phosphate binding to a single PA at pH 11 (-2.8 kJ/mol). Interestingly,

this result highlights that binding at pH 6 in the assembled state is even more stabilized compared to binding to the unimer PA at pH 11.

Finally, an H-bond analysis was performed to quantify the binding percentage of phosphate to the micelle at both pH states. We define the binding percentage to be the percent of time that a phosphate forms at least one H-bond with the micelle, averaged over the simulation time and phosphate samples. This was found to be 59% and 0.4% at pH 6 and 11, respectively. Though the simulated binding percentage at pH 6 is lower than the experimental measurement of complete capture, these values qualitatively capture the significant difference between binding performances at pH 6 and 11.

Having quantified that the pH shift is in fact occurring, we probed the fundamental reason for why. For pH 11, we noted two phenomena that caused this decrease in binding, one pertaining to a per-molecule analysis and the other pertaining to a newly emergent and noteworthy bulk property. The per-molecule insight was derived from the radial histogram data. When binding did occur at pH 6 (Figure 2.5B), we observed that GGG no longer interacted with the phosphate in the assembled state, even though previously GGG played an active role in stabilizing phosphate as a unimer PA, especially for pH 11. It is likely that the densely packed corona prohibited the phosphate from penetrating deep enough into the corona to fully utilize the additional hydrogen bonds of the GGG backbone. With these key components of binding now inaccessible in the micelle state, phosphate was unable to be bound and stabilized at high pH.

Second, we were motivated by the TEM images of clustered PA micelles (Figure 2C) to probe how the lysine side chain deprotonation influences binding according to a bulk micellar mechanism. As discussed previously, the micelle was apparently teetering on the edge of insolubility, so simply approaching the pK_a and deprotonating a small fraction of lysine amines

causes to micelles to clump together. To quantify the impact of this phenomenon on binding, we relied on the solvent-accessible surface area (SASA) for the entire micelle to measure the extent of headgroup presentation to the aqueous environment, and thereby to the phosphate ions. Using the GROMACS SASA tool,[78] the time-averaged SASA was found to be 798 ± 9 and 623 ± 8 nm^2 at pH 6 and 11, respectively. These results suggest that the deprotonation of lysine leads to a statistically significant decrease in micellar surface area, and with that a decrease in access to binding sites. Thus, as more of the lysine amines become deprotonated, the micelle corona gradually collapses and expels more and more phosphate, corresponding to the decreased binding in Figure 2.3A as pH rises. The simulated system of all deprotonated lysine amines shows this to the extreme, when the micelle is fully collapsed and phosphate is completely expelled or "squeezed" out of the micelle. Thus, compared to a unimer PA, under assembled conditions, phosphate is no longer able to penetrate the even denser micellar headgroup, and binding becomes impossible, explaining the first part of the pH shift.

To understand the increase in binding stability at pH 6, we utilized data from the H-bonding analysis. In the assembled system, we observed multiple chains involved in binding to stabilize the phosphate in the headgroup in the densely packed corona (Figure A.15). The multi-chain binding behavior is a direct result of the PA micelle assembly, where multiple binding opportunities are simultaneously presented to the phosphate ions. This result is also corroborated by our ratio of PA:PO_4 experiments (Figure 2.3C), which elucidated that multiple chains per phosphate were necessary to achieve complete bulk phosphate capture. This binding mechanism is not available for a single peptide, nor has it been previously remarked on in single-chain binding studies, presenting an additional advantage of this self-assembled binding system where increased binding stability is introduced.

2.3.5 Selectivity Over Nitrate and Nitrite

With knowledge of the fundamental binding properties, we experimentally evaluated the selectivity of C_{16}GGGhex to bind to phosphate in the presence of competing oxyanions, probing the molecular recognition of this material. We chose nitrate and nitrite as the competing anions since those would be the primary competitors in agricultural runoff streams that are rich in these three fertilizer components.[35] In our experiments, we introduced equimolar amounts of nitrate, nitrite, and phosphate to systems with 1x, 2x, and 3x molar excess of C_{16}GGGhex at pH 6, equivalent to 10 ppm phosphate. The results are shown in Figure 2.6.

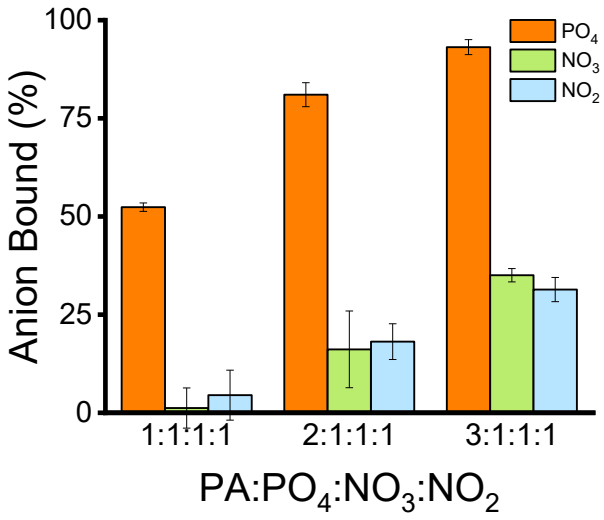

Figure 2.6. Selectivity results for C_{16}GGGhex at pH 6 with molar ratios equivalent to 10 ppm phosphate. Phosphate is bound more than nitrate and nitrite in all cases. In the case of equimolar PA to phosphate, C_{16}GGGhex binds 52% of the phosphate present and less than 5% of nitrate and nitrite, exhibiting excellent selectivity in these conditions. As the concentration of PA increases, C_{16}GGGhex begins to bind to nitrite and nitrate in a linearly increasing trend, while still binding phosphate most.

In all cases, we observe that C_{16}GGGhex binds to phosphate significantly more than to either of the competing oxyanions. In the 1:1:1:1 case, C_{16}GGGhex binds less than 5% of nitrate and nitrite but is still able to sequester 52% of phosphate, consistent with its binding performance without competing ions (see Figure 2.3C). Thus, at this lower concentration of PA, we observe

excellent selectivity and see C_{16}GGGhex performing its designed-in molecular recognition functionality. As we increase the amount of PA in the system, C_{16}GGGhex continues to bind phosphate aligned with the previously observed amounts in Figure 2.3C, but it discriminates phosphate less, following a linear trend of binding increasing amounts of nitrate and nitrite up to 35% and 31%, respectively. This trend could be indicative of the molecular-recognition P-loop being less exclusively employed to capture phosphate through the signature selective nested cavity formation. Instead, C_{16}GGGhex is likely indiscriminately binding nitrite and nitrate by electrostatic attraction to the positively charged lysine, whose abundance increases as the PA concentration increases. It could also be that the densely packed corona prohibits the peptides from adopting the molecular-recognition P-loop nested cavity formation as readily, decreasing its designed-in means to select only phosphate. However, because we do not simply observe proportionate binding of anions in each case but rather observe a linear binding trend that ends in nearly zero binding of competitors, a strong case can be made for P-loop molecular recognition in the 1:1:1:1 conditions.

While these preliminary results present opportunities for optimizing exclusive binding to phosphate even with excess binding sites present, we nonetheless observe molecular preference for phosphate in all cases, with particular success in discriminating between phosphate and its competitors with equimolar amounts of binding sites and phosphate. To harken back to our previous findings in considering routes for optimization, the unique multi-chain binding observed in our micelle simulations presents an intriguing starting point, specific to the versatility PA micelles, to design increased molecular selectivity in future rounds of synthesis.

2.3.6 Cycles of Capture and Release

Finally, we evaluated the capture, release, and reclamation functionality of this material, as well as its durability upon cycles of reuse, providing valuable information for the practical phosphate reclamation potential of our material platform. We sequentially adjusted the pH from 6 to the acidic or basic release pH, collecting and analyzing the filtrate at each step. After filtration at the release pH, we added phosphate to re-achieve a starting concentration of 50 ppm, as calculated from the phosphate concentration of the filtrate.

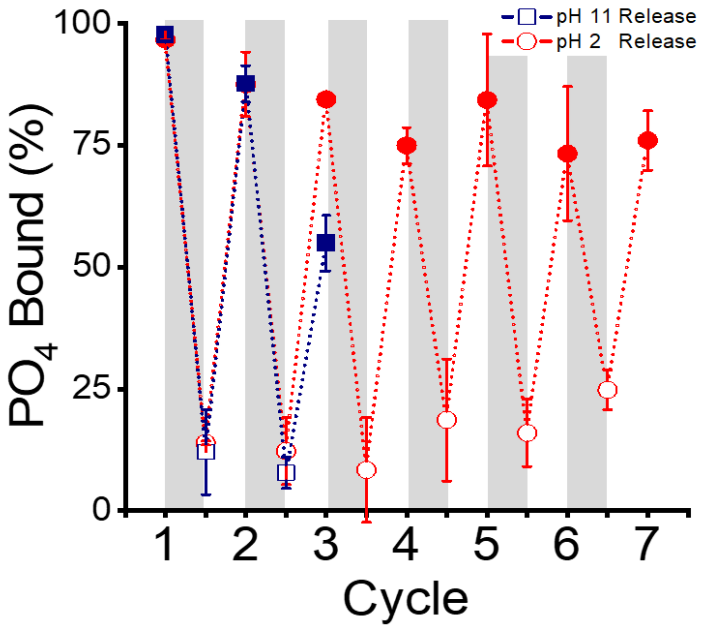

Figure 2.7. Capture and release results for C_{16}GGGhex. The filled-in markers represent the pH 6 capture condition, while the open markers represent the release condition of either pH 2 or 11. The gray rectangle depict the release step from pH 6 to either pH 2 or 11. The material demonstrates an ability to reversibly capture and release phosphate for both the release pH 2 and pH 11. For the pH 11 release condition, the material becomes unable to rebind nearly half of the present phosphate after 3 cycles. It was noted that the solution turns notably cloudy, highlighting how the PA aggregation at high pH likely contributed to a decreased ability to rebind phosphate. For the pH 2 release condition, the material could rebind greater than 73% of phosphate and release up to 75% of phosphate for up to 7 cycles, becoming the superior release condition.

The cycles of capture and release data in Figure 2.7 demonstrate that our material does indeed perform sequential binding and release, and it also highlighted interesting material properties at pH 11. For pH 2 triggered release, the material was able to expel and rebind phosphate for up to the 7 cycles tested, rebinding up to 73% each time and releasing up to 75%. The capture and release performance both diminish as the number of cycles increases, which could be a function of increased time required to achieve equilibrium after successive cycles, highlighting the potential for optimization of this process. The material using a pH 11 triggered release, on the other hand, exhibited a sharp decrease in ability to rebind after only 3 cycles, binding only 55% of the added phosphate in solution. Since this performance was markedly worse, we ceased performing further cycles under this release condition after this point. We believe that this trend is occurring due to the clumping of micelles observed at high pH, which was visually supported by a significant increase in cloudiness of the sample after successive cycles. Thus, it appears that the fundamentally altered binding ability at pH 11, as observed in the simulation results, also negatively impacts the functionality of the material when operating repetitively at these basic release conditions. The decrease in binding for both systems could also be due to loss of unimer PAs upon wash steps. This loss could be averted by locking the assemblies through internal covalent crosslinks, a straightforward design change that has been employed previously,[59] which could increase the robustness and recyclability of the PA micelle network.

In sum, these data demonstrate that our material is capable of successive capture and release of phosphate, as opposed to remaining permanently bound like many adsorbents,[91–93] with promise for further process optimization. More broadly, they highlight the feasibility of using an entangled wormlike micelle structure with phosphate binding units coating the fibers to practically catch,

retain, and separate out the phosphate from water, an advantage over the free-floating peptides which would be difficult to partition out from the solution.

2.4 CONCLUSIONS

We have designed, synthesized, and characterized a prototype of a materials platform to capture and reclaim phosphate, utilizing self-assembled peptide amphiphiles that easily incorporate specific protein-inspired binding sequences to molecularly recognize their specific targets. These peptide amphiphile wormlike micelles form a dense entangled suspension that becomes a solid support for straightforward collection of phosphate in response to a pH trigger. The PA material C_{16}GGGhex sequestered 100% of phosphate at pH 6 and released up to 75% at pH 2 for up to seven cycles. C_{16}GGGhex also was found to selectively bind to phosphate over nitrate and nitrite. Detailed atomistic simulations with advanced sampling confirm that the assembled state of the material fundamentally alters the pH binding functionality compared to the free peptide, shifting the maximal binding conditions from pH 10.5 to 6 due to the micellar headgroup becoming conformationally constrained at high pH, thereby expelling the phosphate. At pH 6, simulations indicate that unimer PAs do not bind phosphate, but they are able to do so via multi-chain binding when assembled into a micelle. Our simulations serve to highlight the important role of PA packing in phosphate binding behavior and suggest a new multi-chain phosphate-binding mechanism that is unique to PA micelles, reminiscent of the tertiary structure adopted by proteins for targeted binding. These findings indicate that PA packing in micelles is an important design factor, thus opening up a new avenue of relying upon multi-chain binding motifs for the design of selective ion-sequestering materials.

This work represents a first step in our aim to incorporate protein-inspired design into a tunable synthetic material for practical resource reclamation from wastewater. Since this material

platform so naturally incorporates protein-inspired binding sequences, we are positioned to easily modify the binding sequence to target a wide array of other valuable resources in wastewater.

CHAPTER 3.

ENHANCED DESIGN: PHOSPHATE-BINDING BY MULTI-COMPONENT PEPTIDE AMPHIPHILE MICELLES AND RESIN-PEPTIDE SYSTEMS

This chapter will be submitted in modified form as a journal article.

3.1 INTRODUCTION

To enhance the prototype phosphate-binding peptide amphiphile (PA) micelle system, we designed a second generation of PA micelles that feature multi-component design. Through this study, we aimed to further probe the effect of charge, hydrogen bonding, and peptide conformation on binding to gain insight on how to optimize protein-binding-inspired engineered materials.

The multi-component PA systems were designed to create a local environment in which the phosphate-binding hexapeptide could more readily utilize its LRLR nested cavity formation to bind to phosphate.[48,49] In this work, we sought to determine if providing the PA system greater access to protein-derived conformation would further optimize phosphate binding, both in selectivity and also greater efficiency of binding at a 1:1 ratio of peptide to phosphate. Multi-component PA systems are well poised to evaluate this, where a second filler PA component can be added to the micelle to decrease the density of the micelle corona and facilitate greater conformational freedom for the hexapeptide-binding-unit. Overall, the design of this study is well suited to evaluate the importance of the three binding parameters for phosphate-binding—amide backbone hydrogen bonding, charge interaction, and LRLR nested conformation—and provide further mechanistic insight on design principles to mimic protein binding by synthetic materials.

3.2 EXPERIMENTAL METHODS

3.2.1 SYNTHESIS AND PURIFICATION OF PEPTIDE AMPHIPHILE MICELLES AND RESIN-PEPTIDE SYSTEMS

The peptide amphiphiles with peptide sequences GGGGGK and GGGGGSGAGKT conjugated to a palmitic acid tail were synthesized, cleaved, and purified as described in Chapter 2. The PS-PEG-Peptide systems were synthesized on 0.25 mmoles of TentaGel® S NH2 Resin (90 μm) for the following peptide sequences: K, KGK, KGGK, KGKGK, and KGGKGGK. The synthesis protocol was identical to that of the rink amide resin systems, with the exception that a double coupling step was performed for each amino acid to ensure complete conjugation. The peptides were not cleaved from the resin. After the coupling steps were completed, the resin was rinsed with dichloromethane, dried under nitrogen, weighed on an analytical balance, and submerged in MilliQ water to reach the desired molar concentration of peptide given the loading (mmol/g) of the TentaGel resin.

3.2.2 Micelle Fabrication Procedure

The multi-component PA micelles were fabricated to ensure homogenous mixing of both PA components in each micelle. To do this, the purified single-component PAs were lyophilized, and the lyophilized powder was dissolved in hexafluoroisopropanol (HFIP), which is a good solvent for PAs that does not promote hydrophobically driven self-assembly into micelles. The PA-in-HFIP solutions of each PA were combined to achieve the desired ratio and molar concentration. The HFIP was evaporated until nitrogen flow, leaving behind a thin film. The film was dissolved in MilliQ water at the desired concentration, heated at 70 ºC for 1 hour on a mechanical shaker, and allowed to equilibrate to room temperature before experimental use.

3.2.3 Critical Micelle Concentration (CMC) Determination

The CMC experiments were performed in an identical manner as in Chapter 2. However, in this case due to a non-linear increased fluorescence regime, the CMC was identified as the

concentration at which the fluorescence value is greater than that of 20% above the zero-slope baseline region.

3.2.4 Cryogenic Transmission Electron Microscopy (Cryo-TEM) Imaging

Cryo-TEM samples were flash-frozen in liquid ethane onto Quantifoil R1.2/1.3 grids (copper, 200 mesh; Q210CR1.3, EMS, Hatfield, PA) using a Vitrobot Mark IV (FEI, Hillsboro, OR). Grids were imaged at 300kV accelerating voltage on a Titan Krios (Thermo Scientific, Hillsboro, OR). The images were processed and measured digitally using ImageJ software.

3.2.5 Analysis of pH-Dependent Phosphate Binding

Samples were prepared in MilliQ water in molar ratios of 1:1, 2:1, and 4:1 of Peptide:PO_4 for the phosphate-only experiments, and 1:1:1:1, 2:1:1:1, and 4:1:1:1 of Peptide:PO_4:NO_3:NO_2 for the selectivity experiments, all equivalent to 10 ppm PO_4. The salts used were Na_2HPO_4, $NaNO_3$, and $NaNO_2$. The pH was adjusted to the desired pH condition using minimal HCl and NaOH, and the pH was measured using a Fisher Scientific Accumet XL500 pH/ISE/Conductivity Benchtop Meter (Vernon Hills , IL, USA) and a Fisherbrand Accumet Micro Glass Mercury-Free Combination Electrode. Upon reaching the target pH, the solution was filtered using a 13 mm 0.22 μm GHP Acrodisc syringe filter to separate the unbound anions from the PA-anion bound complexes. The filtrate was analyzed using ion chromatography using a Thermo Scientific Dionex ICS-5000+ equipped with a Dionex AS-DV autosampler and using a Dionex IonPac AS22 column (Product No 064141, Thermo Scientific, California, USA). The analysis was run using an eluent of 4.5 mM Sodium Carbonate and 1.4 mM Sodium Bicarbonate (Product No 063965 from Thermo Scientific, California, USA) and a Dionex AERS 500 Carbonate 4 mm Electrolutically Regenerated Suppressor (Product No 085029 from Thermo Scientific, California, USA). The experiments were performed in duplicate for each condition.

3.3 Results and Discussion

3.3.1 Multi-Component Peptide Amphiphile Design Scheme

A series of multi-component peptide amphiphile micelles were designed to isolate the relative contributions of conformation, hydrogen bonding, and electrostatic attraction on peptide binding of phosphate in a PA micelle (Figure 3.1). This rational design was informed by a key insight derived from our previous work, namely that the phosphate ions were stabilized through hydrogen bonding and electrostatic attraction from multiple peptide chains in the micelle corona, reminiscent of tertiary binding.[94] However, in this high-density environment of the peptide micelle corona, the peptide binding motifs were conformationally constrained, and the protein-derived LRLR nested cavity conformation was limited.

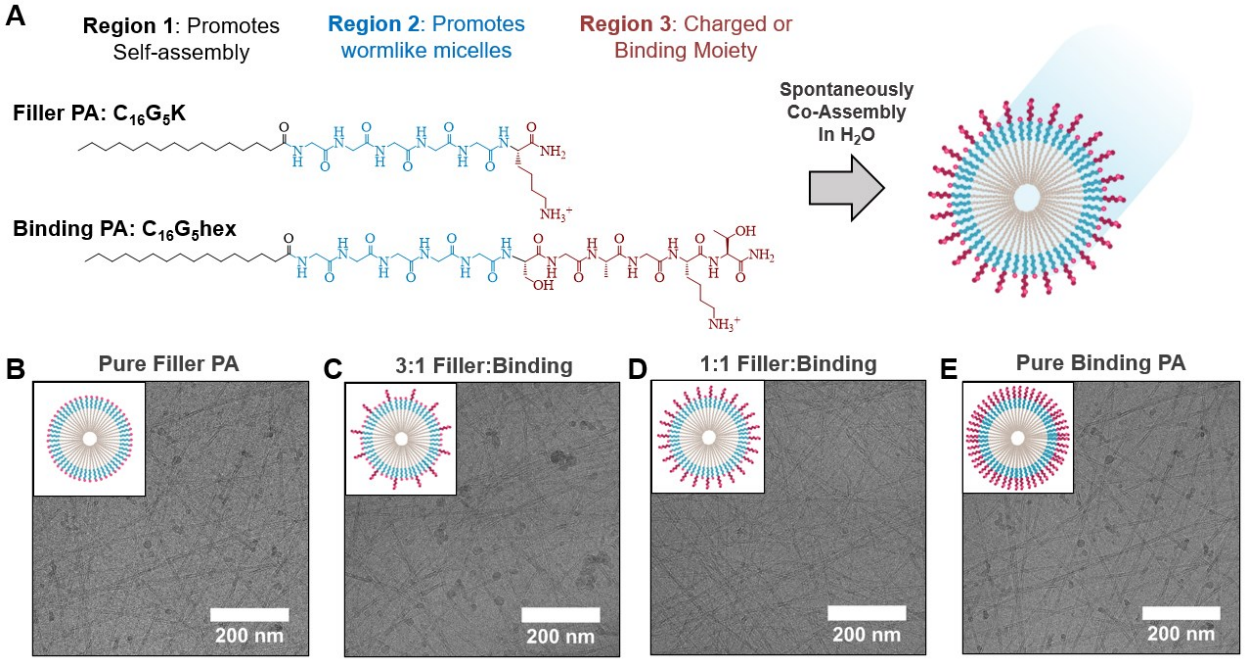

Figure 3.1. (A) Molecular structures of the Filler PA and the Binding PA that feature three building block regions, which spontaneously co-assemble into a micelle in water due to the hydrophobic effect. (B) Cryo-TEM images of the four PA systems with varying ratios of Filler PA to Binding PA, which reveal extended wormlike micelles for all systems.

Here, we aimed to reinsert the protein-derived conformation into the system design by sequentially decreasing the density of the peptide binding motifs in the micelle corona, making the motifs less conformationally constrained. We hypothesized that increasing the conformational freedom of the phosphate-binding motifs would further optimize phosphate binding, allowing the protein-analogous micelle to more closely mimic P-loop binding by accessing the three established binding parameters: hydrogen bonding, charge attraction, and nested cavity conformation.

Multi-component PA systems are well poised to evaluate this. The peptide density can be precisely tuned by spontaneous co-assembly of a Binding PA and a Filler PA into multi-component supramolecular structures as predetermined compositions. Here, we designed a series of four PA micelle systems using both components, with the composition of Binding PA sequentially reduced by half from 100% to 50% to 25%. A pure Filler PA system was also evaluated as a control for non-sequence-specific binding. A similar design scheme was used by Honggang Cui and co-workers. They designed a two-component PA micelle to bind to monoclonal antibodies, and they found that decreased composition of the binding moiety corresponded to increased antibody capture.[63]

Each PA was designed with tunable "building block" regions with individualized function.[2,67] The Binding PA, denoted $C_{16}G_5$hex, is derived from the prototype phosphate-binding PA micelle with nearly identical design.[94] Region 1 is a hydrophobic tail required to facilitate self-assembly. Region 2 is a five glycine spacer region to promote wormlike micelle formation,[83] which is the desired micelle architecture to create an entangled network of PA micelles to capture and release phosphate. The number of glycine residues was increased from three to five in this study to further extend the binding motif into the environment and access greater conformational freedom, as well as increase the solubility of the Filler PA counterpart. Region 3 is the protein-

derived P-loop hexapeptide binding moiety, SGAGKT, that has previously been shown to bind phosphate.[56,57,94] The Filler PA, denoted $C_{16}G_5K$, has identical Regions 1 and 2 to ensure that it homogenously co-assembles with $C_{16}G_5$hex. The binding moiety in Region 3 is substituted with a lysine residue, which was required for solubility.

We synthesized the PAs using FMOC solid phase synthesis and purified them to greater than 95% purity (Figure B2). All PAs were found to self-assemble into wormlike micelles using cryogenic transmission electron microscopy (cryo-TEM) imaging (Figure 3.1B-E) with similar dimensions, which will allow for direct comparison between systems.

3.3.2 Experimental Phosphate-Binding Results by Multi-Component PA Micelles

The phosphate-binding abilities of the multi-component PA micelles were evaluated at key conditions derived from our previous study. In that work, phosphate was nearly completely bound at pH 6 and a molar ratio of 3:1 PA:PO_4. We used simulations to probe why this ratio was needed to achieve complete binding, and we observed that two to three PA chains were always required to bind to phosphate in the multi-chain binding effect observed. In our re-engineered multi-component design, we wanted to determine if we could achieve higher binding at a lower ratios of Binding PA to PO_4 if the nested cavity conformation was employed, which would also further elucidate binding mechanistic insight. Thus, we evaluated phosphate binding at pH 6 at ratios of 1:1, 2:1, and 4:1 PA:PO_4. Here the PA is total PA, rather than Binding PA, to keep the PA concentration constant across all systems tested. These ratios nicely complement the Binding PA multi-component compositions chosen and would easily facilitate a direct per-molecule binding analysis. For example, a 4:1 PA:PO_4 ratio for the 3:1 Filler:Binding system would have a 1:1 ratio of binding motif to phosphate.

In our previous work, we also described how phosphate-binding in the micelle at high pH was restricted due to a "squeezing" effect of the micelle corona when the amine lysine side chain was deprotonated at high pH, which is contrary to phosphate binding trends of the free hexapeptide.[56,57] Thus, we evaluated binding at pH 10 and 11 again here to determine if decreased density of the micelle corona would mitigate this squeezing effect and replenish the ability to bind at high pH.

The phosphate binding performance of the four PA systems are shown in Figure 3.2. The results are surprising, revealing similar binding trends across all four systems for identical conditions. At pH 6, we observe essentially complete binding of phosphate at 4:1 ratio of PA:PO_4 for all systems, with incomplete binding at lower ratios. These PA:PO_4 ratio trends are consistent with our previous work. We also see similar trends across pH conditions as in our previous study, namely that binding was still prohibited at pH 10 and 11 but maximized at pH 6. The only noticeable difference between systems is that there is marginally higher binding for the Pure Filler PA and the 1:1 Filler:Binding PA systems at pH 6 and 1:1 ratio of PA:PO_4, which bound nearly half of the phosphate compared to a quarter in the other two systems.

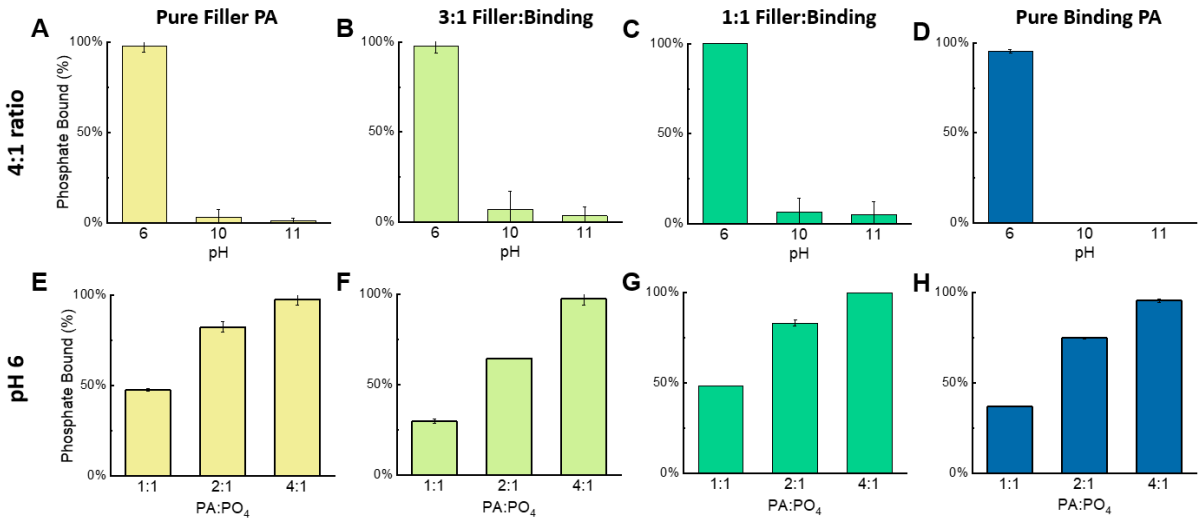

Figure 3.2. Phosphate-binding results of the multi-component micelle systems, with a concentration of 10 ppm phosphate for all systems. (A-D) Phosphate-binding performance of each PA system at a 4:1 ratio of PA_{total}:PO_4 and pH conditions of 6, 10, and 11. (E-H) Phosphate-binding performance at pH 6 of increasing ratios of PA_{total}:PO_4. The binding trends are nearly identical across all systems, contrary to expectation.

These unexpected results lead to several conclusions. First, as the density of the phosphate-binding motif decreases from 100% to 50% to 25%, there is no noticeable effect on binding, suggesting that increased conformational freedom of the unit in this design does not correlate with more efficient 1:1 binding of phosphate. What is more surprising is that the trend remains intact even for the pure Filler PA system, which was designed to be a control system. Thus, apparently the binding contributors from this system, which are limited to hydrogen bonding from the amide backbone and electrostatic charge, are sufficient to achieve binding in this densely packed corona. Second, the similar PA:PO_4 ratio trend for binding suggests that multi-chain binding is retained in these systems, where complete capture of phosphate only occurs at a 4:1 ratio of PA:PO_4. Finally, we determined that binding at high pH is not restored as the density is reduced, also suggesting that a similar binding mechanism is employed in these systems as was observed in the prototype single-component PA system.

These results indicate that the LRLR sequence-specific nested cavity conformation has negligible impact on binding in the densely packed micelle corona; instead, hydrogen bonding and electrostatic attraction contribute more significantly. As such, we are poised to translate these design insights and physical principles to engineer *de novo* peptide sequences to determine if we can mimic protein binding of phosphate without the predetermined conformational restrictions that are characteristic of protein binding.

3.3.3 Case Study: Evaluating Design Principles through Single-Peptide Binding of Phosphate

To engineer *de novo* peptide sequences for phosphate binding, we designed a series of simplified motifs to manipulate the effects of hydrogen bonding and electrostatic interaction. We chose only to build the motifs using glycine and lysine residues. Those residue were the only residues present in the Filler $C_{16}G_5K$ PA micelle that bound phosphate, and they have been determined to play an essential role in phosphate-binding proteins (PBPs) since they are highly conserved in the P-loop sequence of PBPs.[55] We also wanted to more precisely isolate the individual molecular mechanistic binding principles, so we switched material platforms from the highly interactive peptide micelle corona to a polystyrene-polyethylene-peptide Tentagel resin system that has been used to characterize single-peptide binding.[24]

Using glycine and lysine residues, we constructed five peptide motifs. The first was a single lysine (K) residue, to determine if binding could be achieved by a single charge alone, without significant hydrogen bond contributions. The other four motifs varied two design variables: (i) charge number, through controlling the number of lysine residues, and (ii) charge spacing and their corresponding conformational freedom, adjusted through the number of glycine residues that spaced the lysine residues. From these guiding principles, the four synthesized sequences were

KGK, KGGK, KGKGK, and KGGKGGK. Their phosphate binding performance is shown in Figure 3.3 at pH 6 and 1:1, 2:1, 4:1, and 8:1 peptide:PO_4 molar ratios, all at a phosphate concentration of 10 ppm.

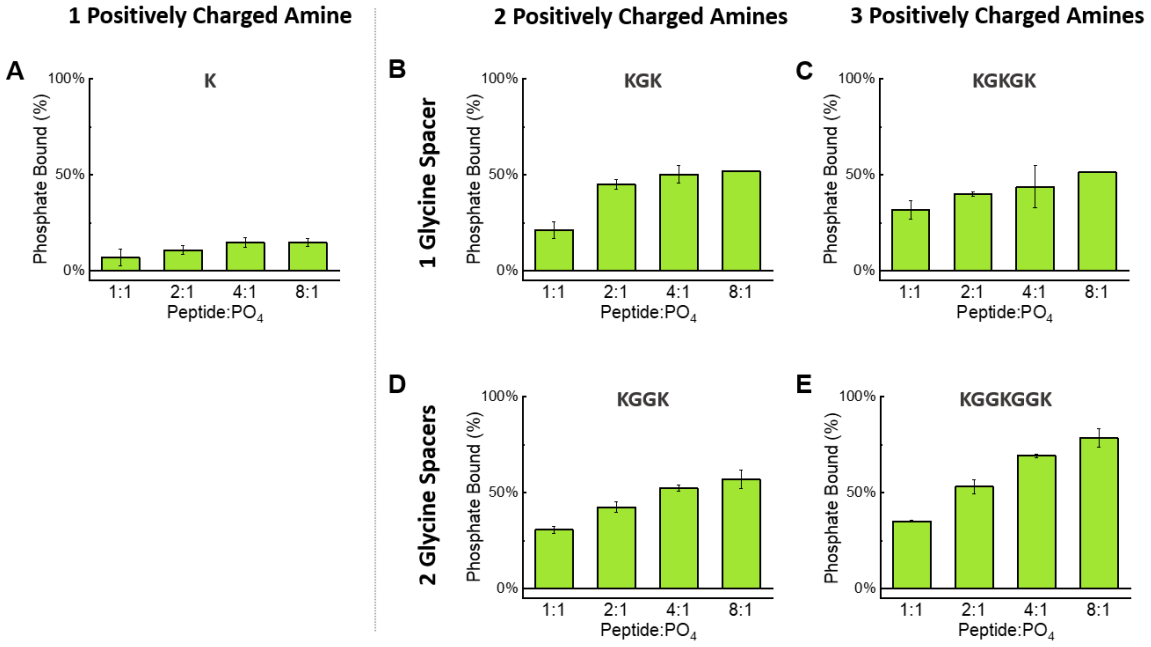

Figure 3.3. Phosphate-binding results of five single-peptide motifs, (A) K, (B) KGK, (C) KGKGK, (D) KGGK, and (E) KGGKGGK, at pH 6, 10 ppm PO_4, and 1:1, 2:1, 4:1, and 8:1 peptide:PO4 molar ratios.

Significantly, the phosphate-binding results demonstrate that binding can be achieved by *de novo* peptide systems. All systems excluding the K system bound phosphate to a noteworthy degree as the ratio of peptide increased. The KGK, KGGK, and KGKGK systems all performed similarly, with roughly half of phosphate bound at 4:1 and 8:1 ratios of peptide to phosphate. KGGKGGK bound the highest percentage of phosphate at 78%±4.8% for an 8:1 ratio of peptide:PO_4. The K system shows minimal binding, indicating that a single charge alone is insufficient to bind to phosphate. None of the systems achieved 100% binding of phosphate at the ratios tested.

The *de novo* systems also offer a valuable conformational design insight towards synthetic mimicking of protein-binding. Comparing KGKGK to KGGKGGK, we see that increased spacing and conformational freedom between charges promotes higher binding performance. This finding can be considering alongside the PA micelle binding results. In PA micelles, the charges and hydrogen bonding donors are highly flexibly and can readily adopt a specific conformation in the densely packed corona that is required to bind to phosphate. These two systems together suggest that although binding occurs independent of the specific LRLR nested cavity conformation, there is still a conformation factor that needs to be optimized to achieve binding.

Binding in these systems is also likely correlated to entropy maximization of the chains, where chains are not forced to adopt a specific constrained conformation to bind, but rather can bind through multiple flexible binding factors. The flexible PA micelle and the KGGKGGK systems are better poised to adopt a favorable binding conformation than the other three more rigid counterparts. The finding that increased flexibility corresponds with specific protein binding is corroborated by a recently published paper in *Nature*. Tae Su Choi & F. Akif Tezcan deliberately designed an artificial protein to be flexible, which enabled the protein to adopt conformational structures needed to bind to metal ions.[95] It is also possible that none of the single-peptide chains could achieve 100% binding at the conditions tested because they were more conformationally limited compared to the flexible peptide arrangement within the PA micelle.

Despite not achieving complete binding in these single-peptide resin systems, we were nevertheless able to demonstrate that synthetic binding sequences can still be employed to bind to phosphate. This intriguing result indicates that we no longer need to be limited to protein-derived sequences and particular tertiary and quaternary structures to mimic protein binding. While these systems present a reduced design approach, we are positioned to translate these features and

principles to more sophisticated sequences and systems in the effort to engineer precise biomimetic materials.

3.3.4 Selectivity of PA Micelles and Resin-Peptide Systems

Finally, we sought to compare not just the ability of both systems to bind, but also their abilities to perform selective binding. We tested against nitrate and nitrite, since that would be a key competing anion in fertilizer runoff. Unfortunately, we only report selectivity for nitrate for the Resin-Peptide systems, since there was an artifact peak in the ion chromatograms for the resin systems that interfered with the nitrite peak.

The selectivity results for the PA micelles are shown in Figures 3.4. Surprisingly, the selectivity is conserved across all systems, even though the LRLR nest is removed from the Pure Filler PA system. One might have expected the selectivity performance to decrease as the hexapeptide binding motif is removed, even if the overall phosphate binding performance is retained across systems. This similarity again suggests that a similar binding mechanism is employed across all four PA systems. Compared to the prototype C_{16}GGGhex system, the ratio of phosphate bound compared to nitrate and nitrite is similar (Figure 2.6).

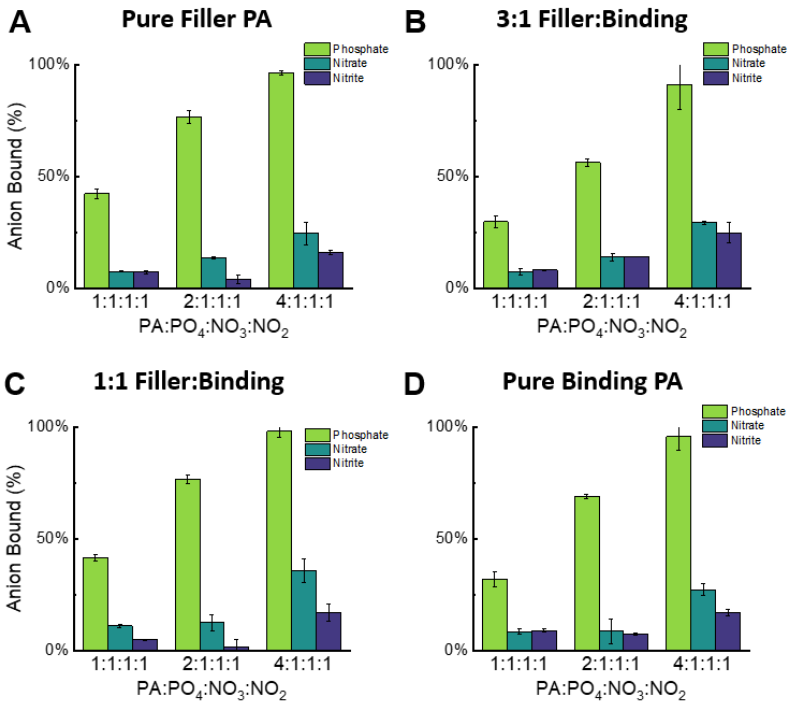

Figure 3.4. Selectivity phosphate-binding results over nitrate and nitrite of four PA micelle systems at pH 6. The phosphate concentration is 10 ppm and the molar ratios of PA:PO_4:NO_3:NO_2 evaluated were 1:1:1:1, 2:1:1:1, and 4:1:1:1. The performance across the systems shows similar trends.

The selectivity results for the Resin-Peptide systems are shown in Figure 3.5. In another surprising result, selectivity was not as pronounced for these systems as it was for the PA micelle, with more nitrate being bound by these systems. This result is unexpected in another manner, because if binding was solely achieved by charge and hydrogen bonding, then one might expect a similar selectivity trend as was seen in the PA micelle system.

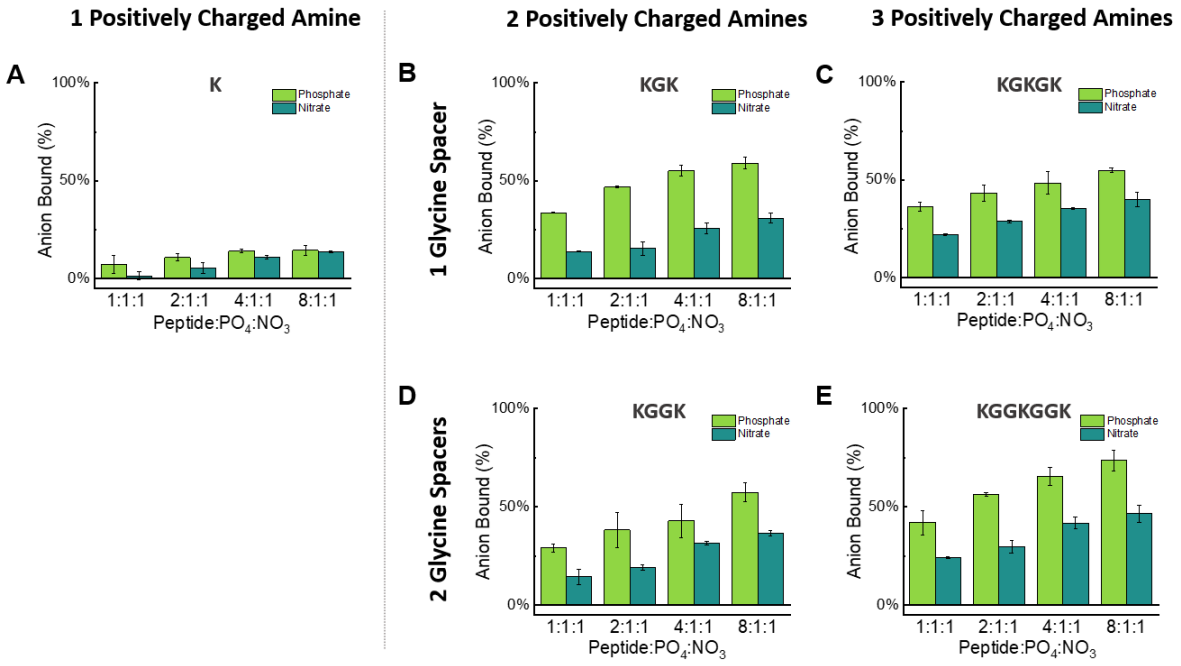

Figure 3.5. Selectivity phosphate-binding results over nitrate of five single-peptide motifs at pH 6. The phosphate concentration is 10 ppm and the molar ratios of PA:PO_4:NO_3 evaluated were 1:1:1, 2:1:1, 4:1:1, and 8:1:1.

While further study is merited to understand this difference in selective performance between peptide systems, one potential explanation could be related to the nature of the ions. While both ions have a single negative charge at pH 6, they have different geometries: phosphate is tetrahedral, and nitrate is planar. It could be that because the micelle is a highly interactive and flexible platform, it may be more conducive for the peptide chains of the micelle to form a three-dimensional structure that binds to a tetrahedral ion rather than being more conformationally limited to assuming a planar binding conformation. It is not entirely clear why selectivity is worse for the Resin-Peptide system, but perhaps the single-chain conformation is not as able to be as discriminatory in possible conformations as the micelle system can, thereby reducing the its ability to bind selectively.

3.4 CONCLUSIONS

Overall, we determined that complete and selective binding by peptides can be achieved independent of sequence when facilitated by the densely packed, highly flexible micelle peptide corona environment. This micelle platform has the unique advantage of presenting a high density of adaptable hydrogen bonding donors that can readily adopt the conformation necessary to bind to phosphate. Whereas proteins must rely on adopting a specific conformation, the protein-analogous micelle can adapt more readily to achieve binding conformations within the headgroup that utilize both charge and hydrogen bond donors. We started out the study with three design parameters—hydrogen bonding, charge, and conformation—and now we can add a fourth to the list, entropy maximization, which is often non-accessible in naturally occurring proteins which have to resort to a highly constrained conformation to bind. These results make the peptide micelle platform highly intriguing for future rounds of protein-inspired binding design, presenting a high concentration of highly flexible and tunable binding contributors in one local environment. Finally, we demonstrated that *de novo* phosphate-binding peptide sequences can be engineered from these design principles, opening intriguing opportunity for biomimetic materials to overcome the highly complex binding mechanisms of proteins to outperform them through informed engineered design.

CHAPTER 4.

UNEXPECTED INTRINSIC FLUORESCENCE IN PEPTIDE AMPHIPHILE MICELLES WITH PROTEIN-INSPIRED PHOSPHATE SENSING

This chapter will be submitted as a journal article.

4.1 INTRODUCTION

Engineering functional biomimetic materials has become a rich field of study that harnesses insights from evolutionarily optimized biological materials and translates these findings to functionalized synthetic materials. One quintessential biomimetic material is peptide amphiphile micelles (PAMs).[59,96–98] Peptide amphiphiles consist of a peptide headgroup conjugated to a hydrophobic tail that spontaneously self-assemble into micelles in water to systematically display the peptide to the aqueous environment. PAMs fuse strategic material design and fundamental study with a diverse and creative array of applications including targeted drug delivery,[99] protein purification,[63] nutrient reclamation,[94] nerve regeneration,[12] and tissue scaffolding for spinal cord recovery.[13] This wide breadth of functionality is directly linked to tunable material design advantages. The precisely controlled synthesis yields a monodisperse product for sequence-specific biomimetic applications; the PA-to-PA interactions within the micelle can be tuned to control the self-assembled architecture and conformational secondary structure;[60,61,100,101] and multi-component composite materials can be easily fabricated to engineer in advanced multi-faceted use in one material platform.[102,103]

Interestingly, despite their thorough study and diverse use over the past two decades, to my knowledge no one has reported that this class of materials, without a fluorescent tag, possesses unexpected intrinsic fluorescence. This exciting discovery adds an additional desirable feature to this already robust material platform that pairs well with many current uses of PA micelles, such

as bioimaging and sensing, fueling even more routes of study and application for this biomimetic material.

This discovery emerged when I connected similarities between the molecular and self-assembled features of PAMs and features of other recently reported materials that unexpectedly fluoresce.[104,105] These other unexpectedly fluorescent systems similarly did not contain aromatic rings to suggest fluorescence *a priori*; instead, they featured electron-rich moieties in lone pairs of oxygens[106,107] or the double bond of an amide.[108] Nevertheless, these materials possessed two parameters required to exhibit fluorescence through a phenomenon known as aggregation-induced emission (AIE): that (1) electron-rich moieties be "space conjugated," rather than covalently conjugated, to be close enough to create emission pathways between subfluorophoric molecules, and that (2) these moieties be restricted in vibrational or rotational motion to minimize energy loss through those modes. One study by Liu et al. reported unexpected fluorescence for a material with remarkably similar features to PAMs, namely surfactant micelles with closely packed amide bonds at the hydrophobic/hydrophilic corona interface.[108] PAMs likewise possess closely packed amide bonds in the micelle corona, so I evaluated PAMs at the identical excitation and emission conditions, which unveiled their undiscovered intrinsic fluorescence.

While AIE has yet to be reported for PAMs to my knowledge, there have been reports of aggregation-induced emission of bio-inspired materials as far back as 2001,[109,110] coinciding with the discovery of AIE itself. AIE was first reported by Tang, et al. for 1-methyl-1,2,3,4,5-pentaphenylsilole that by itself was weakly emissive but upon aggregation exhibited a sharp increase in fluorescence,[111] sparking many aromatic AIE materials to be designed and characterized. That same year, Swaminathan et al. reported fluorescence of a highly concentrated L-Lys solution, a feature that was attributed to AIE.[109] In 2006, amyloid-like fibers were found to

fluoresce,[112] prompting numerous studies to understand and optimize biological or biomimetic AIE materials,[113–115] with exciting developments in sensing applications.[116–119] However, AIE materials historically have possessed several distinct disadvantages to overcome in order to be practically viable, including poor solubility in water due to aromatic components, a lack of hierarchical self-assembling control,[120] complicated synthetic routes, and challenge in functionalization for application.[114] Peptide amphiphile micelles inherently overcome all of these limitations in one highly tunable platform.

In this work, I present fundamental characterization of this newly discovered intrinsic fluorescence in peptide amphiphile micelles and highlight their promise as a new bioinspired sensing platform with preliminary phosphate detection results. Overall, this discovery of AIE in a well-studied, highly tunable, widely applicable, and easily functionalized material unveils a controllable approach for systematic study of the mechanism of AIE and a strategic platform for rationally designed protein-inspired sensing applications.

4.2 Experimental Methods

4.2.1 Synthesis and Purification of Peptide Amphiphile Micelles and Micelle Preparation Procedure

Three peptide sequences (GGGGGK, GGGGGSGAGKT, and SSSSSSGAGKT) were synthesized on 0.25 mmoles of rink amide resin (Novabiochem) through standard FMOC solid phase peptide synthesis using an automated Prelude X Benchtop Synthesizer (Protein Technologies, Tuscon, AZ, USA). For each coupling step, the FMOC protecting group was first removed from the resin using 20% piperidine in dimethylformamide (DMF). Separately, the amino acid was activated with N,N,N',N'-Tetramethyl-O-(1H-benzotriazol-1-yl)uranium hexafluorophosphate (HBTU) and N,N-Diisopropylethylamine (DIPEA) in a molar ratio of

1:4:3.95:8 of resin: amino acid: HATU: DIPEA. The activated amino acid cocktail was then added to the deprotected resin and then allowed to mix to conjugate. After the amino acid couplings were completed, the deprotected glycine N-terminus was then coupled with a palmitic acid tail.

After drying the resin under nitrogen, the peptide amphiphiles were then cleaved from the resin using a 95:2.5:2.5 by volume trifluoroacetic acid: triisopropylsilane: MilliQ water cleavage cocktail for 2 hours while shaking. The cleaved peptide amphiphiles were then precipitated through dropwise addition of the cleavage solution in a 50:50 by volume hexanes: -80 ºC diethyl ether solution. The peptide amphiphiles were dried under nitrogen and dissolved in water.

The peptide amphiphiles were purified using reverse-phase HPLC (Prominence, Shimadzu, Columbia, MD, USA) on a C8 column (Waters, Milford, MA, USA) at 50 ºC using acetonitrile and water with 0.1% formic acid as gradient mobile phases. The molecular weight of the products in the HPLC fractions were characterized by MALDI-TOF mass spectral analysis (Biflex III, Bruker, Billerica, MA, USA). The product-verified fractions were lyophilized and stored as powders at -20 ºC. The purity was analyzed using a similar gradient method on an Agilent 6130 LCMS system in the University of Chicago's Mass Spectrometry Facility, using a Waters column, C8, XBridge, 4.6 mm × 150 mm, 5 μm particle size, and 130 Å pore size. The purity was calculated by integrating the area under the peaks during the elution time and dividing the area of the product peak by the area of all peaks, excluding peaks that were artifacts of the method. The purity was confirmed to be greater than 95% for all PAs. The precise PA concentration for the purified samples was calculated by Amino Acid Analysis (AAA), which was performed by the Molecular Structure Facility at the University of California Davis. The PA samples were then lyophilized in fractions for storage until later use. To fabricate the micelles, the lyophilized PAs were dissolved

in MilliQ water at the desired concentration, heated at 70ºC for 1 hour on a mechanical shaker, and equilibrated to room temperature before experimental use.

4.2.2 Negative-Stain Transmission Electron Microscopy (TEM) Imaging

Carbon film 200 mesh copper grids were glow discharged with a Gatan Solarus plasma cleaning system for 30 s. They were then loaded with 3.5 µL of PAs for 1 minute, and then the excess was removed through blotting with filter paper. The grids were negatively stained with 0.75% uranyl formate for 45 s, blotted off to remove excess stain, and then were allowed to air dry before imaging. All TEM imaging was performed a Technai G2 F30 (FEI) electron microscope operating at 300kV. The images were processed digitally using ImageJ software. For the PA samples with phosphate, before sample incubation and staining, equal volume (2uL) of sample and PO_4 were mixed on parafilm for 1 minute. After 1 minute, all 4 uL was transferred onto the grid and stained as previously described.

4.2.3 Confocal Fluorescent Microscopy Imaging

The PA samples were loaded on a transparent microscope slide and imaged with a Leica Stellaris 8 FALCON (Buffalo Grove, IL, USA) on a DMI-8 stand and a 63x/1.40 oil objective. The white light laser was set to 460nm with reflection mode to the HyD detector and pinhole of 0.2 Airy units. The scan rate was 2kHz, and line average was 48. The reflection method used was based on a previously published method.[1] Fluorescence images were taken with 405 nm laser illumination. The images were process using ImageJ.

4.2.4 UV-Vis Absorbance Measurements

The measurements were recorded using a Shimadzu UV-3600 Plus UV-VIS-NIR spectrophotometer (Columbia, MD, USA). The samples were transferred to a quartz crystal cuvette with a 10 mm path length, and the absorbance was scanned from 200 nm to 800 nm for PA samples

at concentrations of 100 μM, 250 μM, 500 μM, and 1000 μM and quinine sulfate in 0.1 M H_2SO_4 at concentrations of 1 μg/mL, 5 μg/mL, and 7 μg/mL.

4.2.5 Excitation and Emission Measurements Using Fluorescence Spectrometry

The measurements were recorded using a Horiba Fluorolog-3 (Irvine, CA, USA) equipped with a dual monochromator to minimize light scattering from the micelles, which produces additional noise. For the pure PA experiments, a quartz crystal cuvette with a 10 mm path length was loaded with PA sample and transferred to the instrument. The emission scans were recorded for PA samples at concentrations of 100 μM, 250 μM, 500 μM, and 1000 μM at an excitation wavelength of 355 nm and emission values ranging from 370 nm to 650 nm, with an excitation slit width of 5 nm and an emission slit width of 14 nm. The emission scans of the quinine sulfate were recorded at concentrations of 1 μg/mL, 5 μg/mL, and 7 μg/mL at identical conditions. The excitation scans were recorded for PA samples of 11 mM at an emission wavelength of 430 nm and excitation values ranging from 200 nm to 405 nm with an excitation slit width of 3 nm and an emission slit width of 10 nm. The excitation and emission intensities in Figures 4.3C, B.4C, and B.5C are scaled to display comparable peak heights, since the fluorescence intensities are arbitrary. For the PA plus phosphate experiments, phosphate was added to a PA solution in a 1.5 mL centrifuge tube to achieve a final concentration of 1000 μM $C_{16}G_5$hex and final phosphate concentrations ranging from 10 μM to 1000 μM. The solutions were centrifuged using a benchtop 1.5 mL centrifuge at high speed for 5 minutes. The supernatant was collected and transferred to the 10 mm path length quartz crystal cuvette. The emission scans were performed as described.

4.2.6 Critical Micelle Concentration (CMC) Determination using DPH Dye

The true CMC was calculated by marking an increase of fluorescence intensity, corresponding to an increased micelle concentration, of a dissolved dye that fluoresces in the

presence of hydrophobic micelle cores. To execute this experiment, 1,6-diphenyl-1,3,5-hexatriene (DPH) dye was dissolved in tetrahydrofuran at a concentration of 100mM and then diluted in water to a final concentration of 1 μM. Each PA was dissolved in 1 μM DPH solution and serially diluted by half to range from 0.05 μM to 500 μM, performed in triplicates for each PA. The dilutions were allowed to equilibrate for one hour while covered with aluminum foil at room temperature and then were transferred to a 384-well plate. Their fluorescence intensity was measured using a Tecan Infinite 200 plate reader (Mannedorf, Switzerland) with an excitation wavelength of 360 nm and an emission wavelength of 430 nm. The data were plotted with a log-transformed concentration. The CMC was identified as the concentration at which the fluorescence value is greater than that of 20% above the zero-slope baseline region.

4.2.7 Fluorescence Critical Micelle Concentration (FCMC) Determination

The fluorescence critical micelle concentration was calculated simply by serially diluting the PA stock concentration by half to range from 2 μM to 4000 μM. The dilutions were transferred to a 384-well plate. The fluorescence intensity was measured and calculated as for the CMC calculations, but with an excitation wavelength of 355 nm. When plotted with the CMC data, the FCMC data were shifted down by 1500 a.u. and scaled by 10 to emphasize the inflection point comparison.

4.2.8 Circular Dichroism Spectroscopy Measurements

A quartz crystal cuvette with a 0.1 cm pathlength was loaded with 200 μL of PA samples at100 μM. Samples were measured at room temperature using a Jasco J-815 Circular Dichroism Spectropolarimeter (Easton, MD, USA). Three scans were performed for each sample from 190 nm to 250 nm with 0.1 nm step size, and the data were averaged between scans. The data were

converted to mean residue ellipticity and fit according to a minimum-energy calculation of a linear combination of alpha helix, beta sheet, and random coil models.

4.2.9 Gel Fluorescence Imaging

The samples were prepared by depositing 16 µL of 5 mM $C_{16}G_5$hex onto a non-fluorescent black plate, and then adding 4 µL of a given combination of MilliQ water and 20 mM Na_2HPO_4 stock to achieve final concentrations of 4 mM $C_{16}G_5$hex and 0 mM, 1 mM, 2 mM, and 4 mM PO_4. When the phosphate was added to the PA droplet, the droplet was gently stirred with the tip of the pipette to ensure complexation of the PA with phosphate. The samples were prepared in triplicate. The plate was transferred to a BioRad ChemiDoc MP Molecular Imager (Hercules, CA, USA), and fluorescent images were taken using a 530/28 emission filter and an exposure time of 10 s. The integrated fluorescence density of each sample droplet was calculated using ImageJ imaging software.

4.2.10 Phosphate Binding Experiments

Samples were prepared in MilliQ water in molar ratios of 1:1:1:1, 2:1:1:1, and 4:1:1:1 of PA:PO_4:NO_3:NO_2, equivalent to 10 ppm PO_4. The salts used were Na_2HPO_4, $NaNO_3$, and $NaNO_2$. The pH was adjusted to the desired pH condition using minimal HCl and NaOH, and the pH was measured using a Fisher Scientific Accumet XL500 pH/ISE/Conductivity Benchtop Meter (Vernon Hills , IL, USA) and a Fisherbrand Accumet Micro Glass Mercury-Free Combination Electrode. Upon reaching the target pH, the solution was filtered using a 13 mm 0.22 µm GHP Acrodisc syringe filter to separate the unbound anions from the PA-anion bound complexes. The filtrate was analyzed using ion chromatography using a Thermo Scientific Dionex ICS-5000+ equipped with a Dionex AS-DV autosampler and using a Dionex IonPac AS22 column (Product No 064141, Thermo Scientific, California, USA). The analysis was run using an eluent of 4.5 mM

Sodium Carbonate and 1.4 mM Sodium Bicarbonate (Product No 063965 from Thermo Scientific, California, USA) and a Dionex AERS 500 Carbonate 4 mm Electrolutically Regenerated Suppressor (Product No 085029 from Thermo Scientific, California, USA). The experiments were performed in duplicate for each condition.

4.3. Results and Discussion

4.3.1 Design of the Peptide Amphiphile Materials for AIE Insight

Peptide amphiphile (PA) micelles have boasted of facile incorporation of sequence-specific molecular building block regions to precisely control biomimetic function.[67,121] Here, I designed three PA micelles with three building block regions each (Figure 4.1). The goals of this design were two-fold: (1) to directly compare the impact of the tightly packed Region 2 building block on AIE performance, since this region has previously been proven to interact at the micelle interface so significantly that it dictates overall self-assembled micelle architecture[121] and secondary structure,[101] thus likely also strongly impacting AIE function; and (2) to determine the impact of incorporating a functional binding sequence on AIE performance, to probe the potential for designing dual-function PAMs with AIE and bio-inspired targeting.

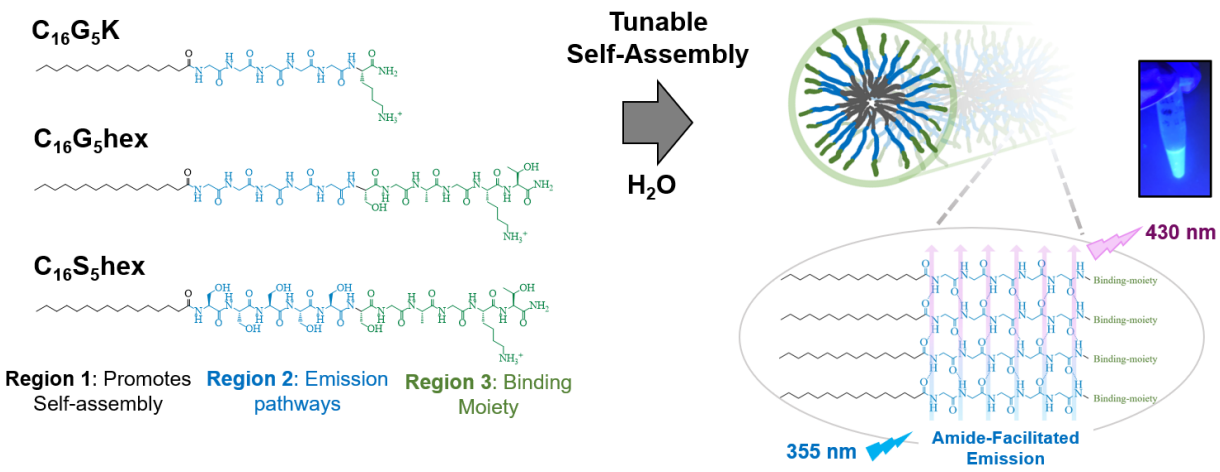

Figure 4.1. Molecular structures of $C_{16}G_5K$, $C_{16}G_5$hex, and $C_{16}S_5$hex with three building block regions to control self-assembly, AIE, and bio-inspired binding function (left). The PA molecules spontaneously self-assemble in water, yielding intrinsically emissive PA micelles that are proposed to fluoresce due to tightly backed peptide amides in the micelle corona. The photo (right) depicts bulk solution fluorescence of $C_{16}G_5$hex.

Two pairs of PAs were rationally designed to meet these aims. First, a strategic principal PA molecule was selected, and then design alterations to this PA were performed on Regions 2 and 3 to directly isolate their relative impacts on AIE. The principal PA, denoted $C_{16}G_5$hex, was derived from a recently engineered PA material that selectively sequesters phosphate.[94] It consists of a sixteen-carbon hydrophobic tail, Region 1, to drive self-assembly; a glycine spacer, Region 2, which has strong intermolecular interactions within a micelle headgroup;[83] and a hexapeptide phosphate-binding moiety, Region 3, that was extracted from a class of phosphate-binding proteins in the protein data bank.[48,56] The majority of the PA design was conserved between studies, but here, the number of glycine spacers in Region 2 was increased from three to five to amplify this region's potential intermolecular AIE effect.

From here, $C_{16}G_5$hex was directly compared to $C_{16}G_5K$ to determine the impact of incorporating a protein-derived binding sequence on AIE. They have identical Regions 1 and 2,

but the hexapeptide binding sequence of $C_{16}G_5$hex was replaced with a single lysine residue in $C_{16}G_5K$, which was required for solubility.

The second pair, $C_{16}G_5$hex and $C_{16}S_5$hex, was designed to probe the impact of Region 2 on AIE. Regions 1 and 3 are identical, but the glycine residues of $C_{16}G_5$hex were replaced with serine residues in $C_{16}S_5$hex. Glycine residues in Region 2 have been reported to promote wormlike micelle formation in PAMs due to being able to pack tightly,[83] which could amplify AIE. Alternatively, serine residues could provide numerous lone pair electrons from the oxygen atom of the hydroxyl group, which could enhance AIE in a similar manner as in other AIE materials with an excess of lone pair electrons.[106,107] Region 2 of PAs has also been determined to strongly impact the secondary structure that peptides adopt within the headgroup,[61,101] a factor that has also been reported to affect AIE.[122,123]

Each of these molecules was synthesized using FMOC solid-phase peptide synthesis, a technique that enables precise synthetic control through step-wise amino acid coupling. Precise control is essential to incorporating these functional building block regions and is a noteworthy advantage of PA micelles.

4.3.2 Self-Assembly Verification through Imaging

PA micelles not only possess synthetic tunability; they also can be designed to self-assemble into a predictable range of micellar constructs by controlling two properties: (i) the packing parameter for surfactant molecules[84,124] and (ii) the inter-peptide interactions, particularly in Region 2 of the molecular design. The packing parameter, P, relates the chemistry of the molecule to its packed self-assembled state in the micelle by using the ratio $P = v/al$, where (v) and (l) are the volume and maximum extended length of the tail, respectively, and (a) is the area of the headgroup at the interface. These molecular design variables can be tuned to achieve different

ratios that correlate to given self-assembled architectures, such as $P < 1/3$ corresponding to spherical micelles and $1/3 < P < 1/2$ corresponding to wormlike micelles. Second, design of inter-peptide interactions also strongly impacts the self-assembled architecture. Densely packable glycine, alanine, and valine residues have been shown to promote wormlike micelle formation,[121] while charged residues such as lysine or glutamic acid have been shown to repulsively interact and drive self-assembly into spherical micelles.[86,94] This aggregation control further elevates PA micelles as a desirable platform to systematically elucidate mechanistic insight of AIE, leading to AIE design insights for optimized functional use.

In this study, the interactions of Region 2 were designed to yield consistent micellar architecture to enable direct comparison of AIE features between systems. It was also hypothesized that wormlike micelles may be more emissive than spherical micelles since the PA molecules are more closely packed. Hence, glycine and serine residues were chosen for the Region 2 residues, which both interact with nearby chains in a packed state and would be likely to yield wormlike micelles upon self-assembly.

The self-assembly properties of the systems were visualized using both negative-stain transmission electron microscopy (TEM) and confocal fluorescent microscopy (Figure 4.2). The TEM images indicated that the PA micelles all self-assemble into wormlike micelles that extend microns in length, yielding the desired consistency between systems. The reflective imaging technique used for confocal microscopy uniquely captures the fluorescent properties of the individual PA micelles.[125] It was also able to construct a 3-D rendering of the micelles in the droplet, which allows one to reconstruct how the extended micelles are arranged in their native liquid state. Overall, while these wormlike micelle systems constitute a consistent preliminary study between like systems, the aggregation properties of this platform can be readily tuned in

future studies to directly probe how the self-assembled architecture impacts AIE properties in PAMs.

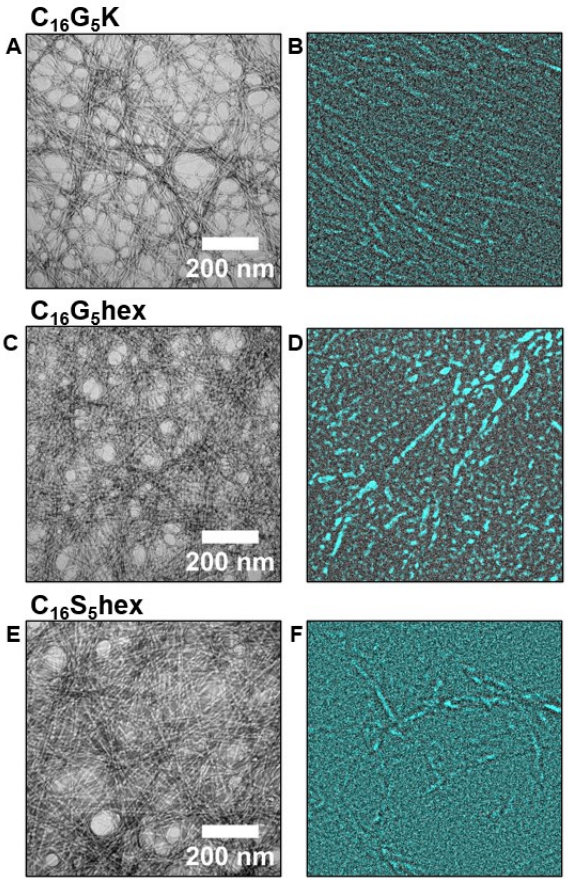

Figure 4.2. Negative-stain TEM images (left) and confocal fluorescent microscopy images (right) of $C_{16}G_5K$, $C_{16}G_5$hex, and $C_{16}S_5$hex. Both visualize self-assembly into wormlike micelles. The scale bar for the confocal images is omitted because the imaging technique used magnifies the constructs beyond true scales. The reader is instead referred to the TEM images for correct scaling.

4.3.3 Fundamental AIE Properties in PA Micelles

After visualizing individual micelle fluorescence, the bulk fundamental fluorescence features were characterized for all three systems. Figure 4.3 depicts results for $C_{16}G_5$hex. The reader is referred to Figures B.4 and B.5 for data for $C_{16}G_5K$ and $C_{16}S_5$hex respectively, which exhibit nearly identical properties for these fundamental experiments. Experiments were performed at room temperature and in MilliQ water. All three systems possess a shoulder in the

absorbance spectra (Figure 4.3A), blue-shifted after the characteristic 220nm absorbance peak for peptides. The maximum excitation and emission occur at 355nm and 430nm respectively (Figure 4.3B). The fluorescence emission intensity increases as concentration is increased from 100 µM to 1000 µM, with no peak shifting or additional shoulders appearing as concentration increases (Figure 4.3C). All of these results are consistent with previous studies that reported AIE of molecules with amide bonds.[108] This suggests a similar proposed emission mechanism, namely that emission occurs across stabilized amide bonds in close proximity within the peptide corona of the micelle.

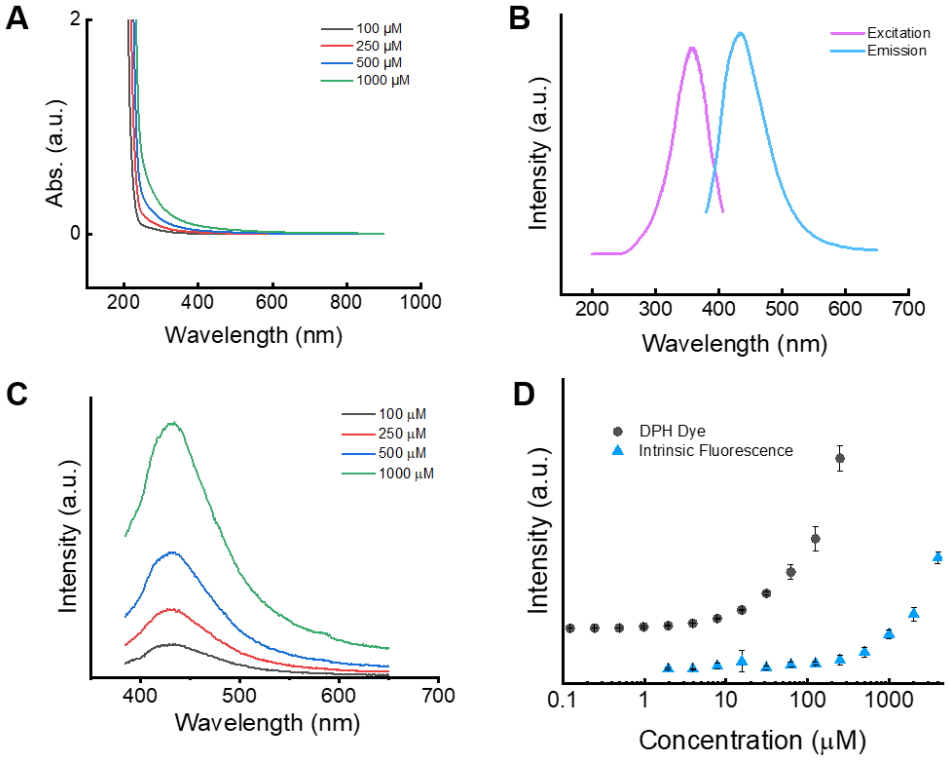

Figure 4.3. Fundamental fluorescence characterization data for $C_{16}G_5$hex, including (A) absorbance intensity, (B) an excitation scan at 430 nm emission and emission scan at 355 nm excitation, (C) the fluorescent emission intensity at an excitation of 355 nm, and (D) the critical micelle concentration (CMC) using 1,6-diphenyl-1,3,5-hexatriene (DPH) dye and the intrinsic fluorescence critical micelle concentration (FCMC). Note: the FCMC data are shifted down by 1500 a.u. and scaled by 10 to emphasize the inflection point shift.

To investigate the aggregation conditions required for AIE, the true critical micelle concentration (CMC) of the micelles, which is the concentration at which PA molecules begin to self-assemble, was compared to the fluorescence critical micelle concentration (FCMC), the concentration at which AIE begins to occur (Figure 4.3D). The true CMC was determined using 1,6-diphenyl-1,3,5-hexatriene (DPH) dye, a standard procedure for calculating CMCs for surfactant molecules.[126] Serial dilutions of PAs were dissolved in an aqueous solution with DPH dye, which fluoresces only when the dye partitions into hydrophobic cores. Thus, an increase in fluorescence indicates that hydrophobic-core micelles are beginning to form, yielding the CMC. The intrinsic fluorescence data was measured without any added dye at an excitation wavelength of 355 nm and an emission wavelength of 430 nm. Both the CMC and the FCMC values were calculated as the concentration value at which the fluorescence intensity value was greater than 20% above the baseline value.

The true CMCs were calculated to be 2 μM, 1 μM, and 1 μM for $C_{16}G_5K$, $C_{16}G_5$hex, and $C_{16}S_5$hex, respectively. The FCMC for all systems was 60 μM. This order of magnitude increase indicates that a critical number of PA unimers must be present and closely packed enough in order to demonstrate AIE. It is also assumed that the PA micelles near the CMC more closely resemble spherical micelles or short rods compared to the extended wormlike micelles visualized in Figure 4.2, which are well above the CMC. It seems feasible that extended wormlike micelles could be more emissive than smaller aggregates, as they provide a less interrupted emission pathway and more closely packed components. Future studies are required to determine the precise impact of micelle architecture on the PAM AIE effect.

It is worth noting that the DPH dye excitation and emission wavelengths are 360 nm and 430 nm respectively, nearly identical to the PA system. In this case, the fluorescence intensity

increase is offset enough to not interfere with the CMC calculation at low concentrations, but this might not always be the case for other PA systems. Interference seems inevitable at concentrations equal to and higher than the FCMC. For future DPH CMC experiments, this interference could be minimized by increasing the DPH concentration several-fold in order to nullify the less emissive AIE effect at higher concentrations.

The quantum yields (QYs) of these PAMs were calculated to normalize and compare the emissive properties between PAM systems, which revealed the first major discrepancy. The QYs were determined by comparing linear fluorescence intensity vs. absorbance curves to a standard solution of quinine sulfate in 0.1 M H_2SO_4 solution (Figure B.6).[127,128] $C_{16}G_5$hex had the highest QY at 1.30%, while $C_{16}G_5$K and $C_{16}S_5$hex had QYs of 0.85% and 0.82%, respectively. To understand the nearly doubled QY for $C_{16}G_5$hex compared to the other systems, the intermolecular interactions were probed using circular dichroism (CD) spectroscopy (Figure 4.4). The CD spectra revealed a predominantly random coil arrangement of peptide chains within the micelle corona for $C_{16}G_5$K and $C_{16}G_5$hex, indicated by the characteristic minima near 200 nm. On the other hand, the spectra for $C_{16}S_5$hex indicated that beta-sheet hydrogen bonding occurred between peptides in the corona, with a negative band near 220 nm and a maximum near 190 nm. This is likely facilitated through the hydrogen-bonding hydroxyl groups of the serine residues.

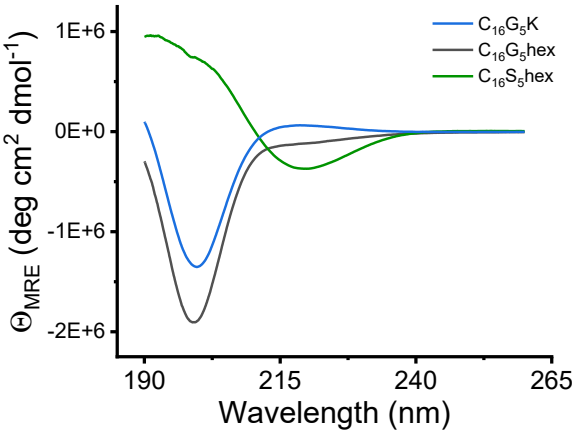

Figure 4.4. Circular dichroism spectra for $C_{16}G_5K$, $C_{16}G_5$hex, and $C_{16}S_5$hex. $C_{16}G_5K$ and $C_{16}G_5$hex display characteristic properties of a random coil configuration with no secondary structure or ordering. $C_{16}S_5$hex largely adopts an ordered beta-sheet structure within the peptide headgroup.

To understand the QY difference, the CD conformational data is paired with molecular design insight as we consider two PAM pairs separately. The first pair, $C_{16}G_5$hex and $C_{16}S_5$hex, have otherwise identical peptide designs apart from Region 2 spacer residues. The exchange of glycine to serine residues in this region had a noteworthy effect on the secondary structure, shifting the inter-peptide interactions from disordered to ordered hydrogen-bonded beta-sheets. Several previous studies have probed the effect of secondary structure on AIE,[122,123] and Lin et al. found that the random coil conformation facilitated the largest AIE properties compared to both alpha helices and beta sheets.[122] The lack of structure enabled the peptide chains to pack more tightly, leading to the not necessarily intuitive conclusion that close proximity of subfluorophores is more important in enhancing emission than adopting ordered emission pathways through beta-sheet hydrogen bonding. This previous finding aligns well with these results. This QY difference between the glycine and serine systems also yields the interesting conclusion that the excess lone electron pairs of the hydroxyl groups do not translate to a higher QY for $C_{16}S_5$hex, even though other systems relied exclusively on this functional group to achieve AIE.[106,107] Either the hydroxyl

groups are not densely packed enough to significantly contribute to AIE in the micelle compared to solid oxygen-based AIE materials like fluorescent rice and starches,[106] or the AIE due to the amide bonds is a much greater contributor in this system.

The QY discrepancy between the second pair, $C_{16}G_5$hex and $C_{16}G_5$K, can be understood by considering molecular design differences since they both exhibit random coil conformation. $C_{16}G_5$K has five fewer amino acid residues than $C_{16}G_5$hex and is otherwise identical. This implies that the emissive pathways for AIE are not just limited to Region 2 but also likely occur across the amide bonds of Region 3 as well, suggesting that further increasing peptide building block length would enhance AIE intensity in future iterations of design. Overall, these findings highlight the direct effect of molecular engineering on AIE performance, indicating the significant potential to optimize the QY of PAMs.

4.3.4 PAM Design Utilizing Second-Order Aggregation AIE to Sense Phosphate

Peptide amphiphile micelles have also been referred to as "protein analogous micelles,"[129] a name that encompasses their unique biomimicry functionality. Here, the phosphate-binding ability of $C_{16}G_5$hex is combined with this newly discovered AIE to engineer a new sensing platform that readily leverages the targeted molecular-recognition ability of proteins.

The predecessor material to $C_{16}G_5$hex was originally engineered to be a capture-and-recovery platform to sequester phosphate for reuse from agricultural runoff.[94] This runoff is often rich in excess fertilizer, which causes severe eutrophication in downstream bodies of water.[45] Concurrently, the global supply of phosphate is being rapidly depleted, prompting calls for creative methods to reclaim and conserve it.[37,42] There has also been complementary interest in designing phosphate-specific sensors to detect phosphate concentration in soil in real-time.[46] This data would be highly valuable to farmers who could adjust their fertilizer distribution accordingly, preventing

large fertilizer excesses from entering runoff and damaging local ecosystems. Phosphate-binding PAMs are well-positioned to be evaluated as phosphate sensors to this end.

$C_{16}G_5$hex was selected for sensing evaluation since it had the highest emissive properties of the three PAMs, likely increasing its sensitivity. The binding and selectivity ability of $C_{16}G_5$hex was evaluated over nitrate and nitrite, the key competing ions in agricultural runoff. $C_{16}G_5$hex was confirmed to bind to phosphate selectively over nitrate and nitrite in a similar fashion as the prototype C_{16}GGGhex material (Figure 3.4). At a 4:1:1:1 molar ratio of PA to each anion, 96% of phosphate was bound while nitrate and nitrite were only bound at 27% and 17%. As the ratio of PA decreases to equimolar, the amount of nitrate and nitrite bound decreased to 8% and 9% respectively while 32% of phosphate was bound. It is also interesting to note that self-assembly was found to enhance the binding and selectivity of phosphate in the original study, so this controllable self-assembly now plays a dual role of enhancing binding and triggering intrinsic fluorescence emission.

With the binding ability confirmed, the triggered AIE sensing mechanism was then designed. Several AIE sensing mechanisms have been developed,[130] and the mechanism utilizing phase-separation enhanced emission complements PAMs particularly well. In this mechanism, binding of an AIE material to its target triggers second-order aggregation, likely due to a decrease in solubility of the AIE material upon binding. This phase-separation causes increased emission intensity since the vibrational and rotational motion is decreased for the more tightly packed subfluorophores. Interestingly, two recent PAMs have reported similar binding-triggered aggregation, including the $C_{16}G_5$hex predecessor. In my previous work, when the PAM bound to phosphate, macroscopic aggregates appeared in solution. Another recent PAM was designed by Dr. Honggang Cui's group to selectively bind to monoclonal antibodies.[63] Upon binding, the

PAMs also phase-separated into a solid-like precipitate, and this was leveraged to extract and purify the target protein.

This second-order aggregation was evaluated and confirmed for $C_{16}G_5$hex. The negative-stain TEM images (Figure 4.5) visualize the clumping effect at the nanoscale level, with second-order aggregates becoming more pronounced as more phosphate was added. By pairing this inherent aggregation with the newly discovered AIE, $C_{16}G_5$hex is intrinsically positioned to become a highly tunable bio-inspired AIE sensing platform.

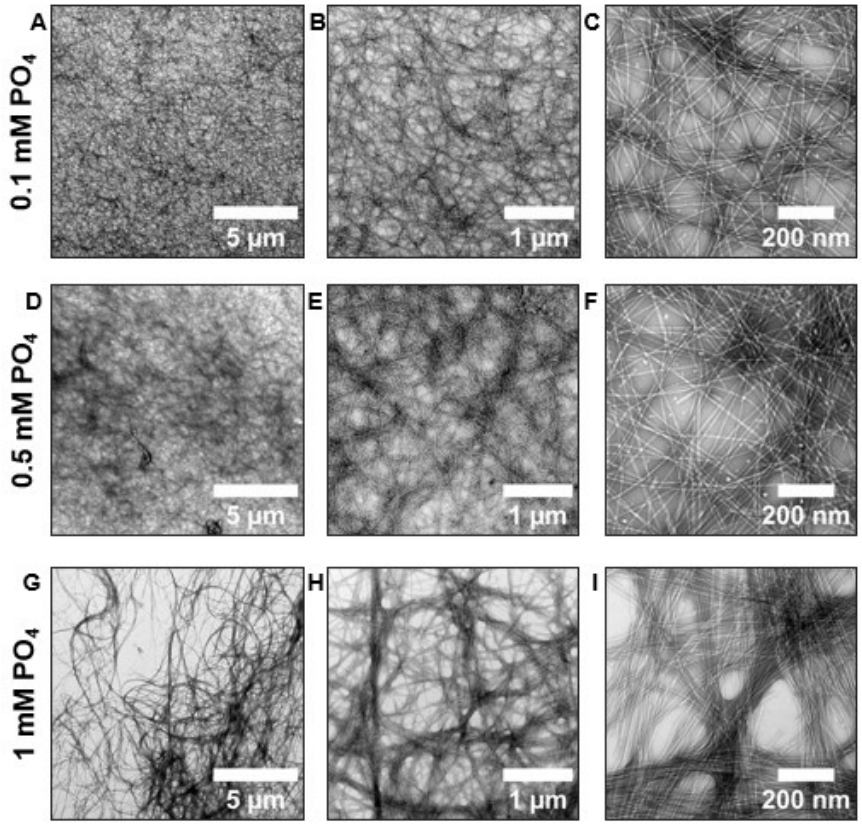

Figure 4.5. TEM images of $C_{16}G_5$hex show second-order aggregation of the self-assembled micelles. As more phosphate is bound, the aggregation becomes more pronounced. The concentration of $C_{16}G_5$hex is constant at 1 mM.

4.3.5 Phosphate Sensing Performance

The preliminary phosphate-sensing characteristics were quantified using gel fluorescence microscopy and fluorometry (Figure 4.6). The gel fluorescence microscopy images visualized how fluorescence intensity increases as more phosphate is added (Figure 4.6A), with the phosphate-PA clumps being the more strongly emissive components in the sample droplets. When the ratio of PA:PO_4 is 1:1, the second-order aggregates are noticeably emissive across the three trials. The remaining solution was no longer visibly emissive, with likely most of the peptide amphiphile partitioning into the macroscopic aggregate. The fluorescence intensity of the samples was quantified using Image J analysis (Figure 4.6B), confirming that emissive intensities indeed were enhanced when phosphate was added. However, the sensitivity provided by this technique is limited, with the lowest phosphate concentration tested being 1 mM, or 95 ppm. Useful levels of phosphate detection would be in the low ppm range.[130]

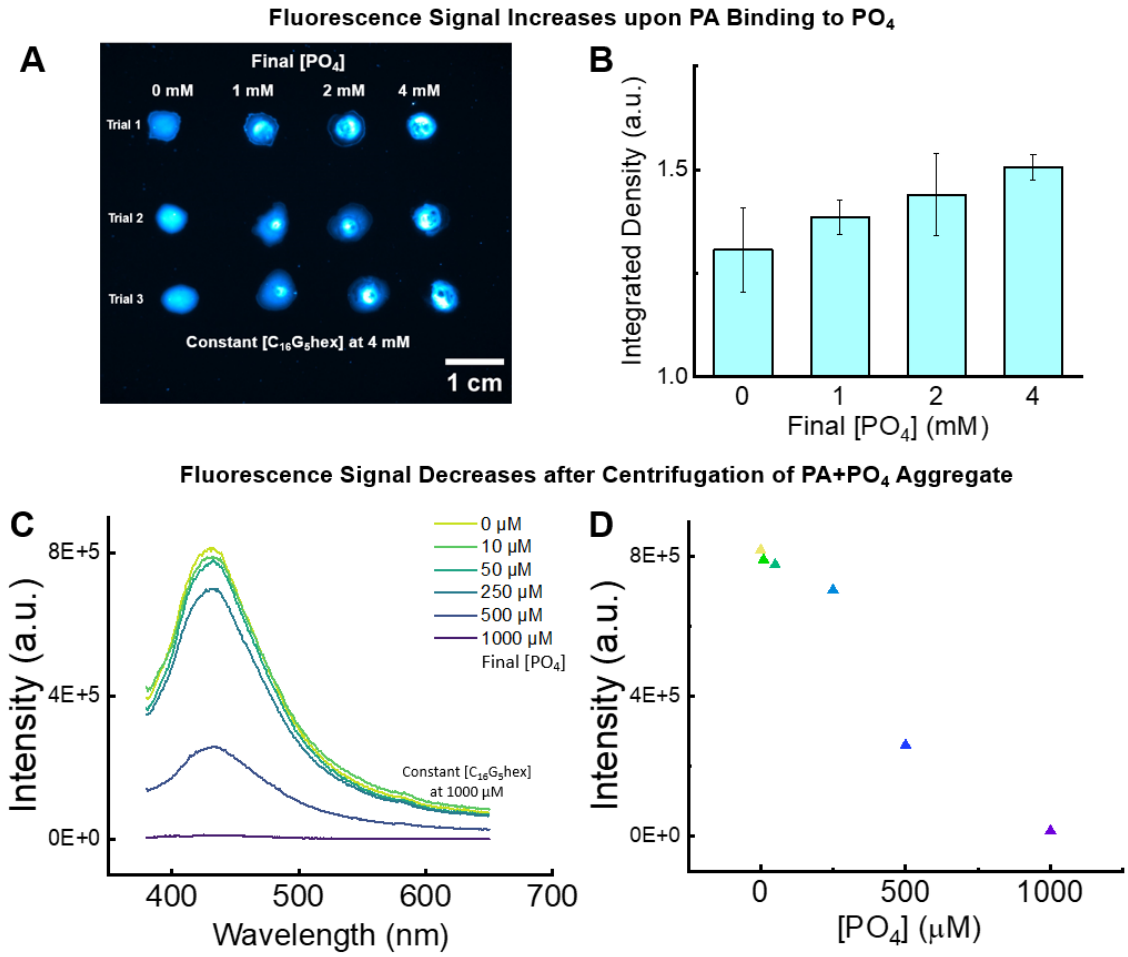

Figure 4.6. (A) Fluorescence gel microscopy images of 4 mM $C_{16}G_5$hex droplets with increasing final concentration of phosphate, with fluorescence intensity increasing as gelled aggregates form when $C_{16}G_5$hex binds to phosphate. (B) Integrated fluorescence density of the droplet images averaged across three trials quantifies the increase in fluorescence intensity. (C) Emission spectra of the supernatant after centrifugation of 1000 µM $C_{16}G_5$hex with increasing amounts of phosphate. As more phosphate complexes with $C_{16}G_5$hex, the supernatant is depleted of $C_{16}G_5$hex and the emission decreases. (D) The fluorescence intensity of the peak maximums at 430 nm for each phosphate concentration, which linearly decreases as added phosphate increases.

To probe the sensitivity limits of this PA platform, emission studies using a dual-monochromator fluorometer were performed. The samples with the macroscopic aggregates could not be measured directly, since the heterogeneity of the samples would produce inconsistent readings. To obtain reliable data using the fluorometer, the aggregate solutions were centrifuged, and the supernatant containing the unbound PA was measured. With increasing $C_{16}G_5$hex being

removed through centrifugation as it bound to more phosphate, the fluorescence of the supernatant was expected to decrease in intensity as more phosphate was added, which was the effect observed in the gel fluorescence microscopy images. This effect was confirmed in Figures 4.6C and 4.6D. With the final $C_{16}G_5$hex concentration held constant at 1 mM, phosphate was added to reach final concentrations ranging from 10 μM to 1000 μM, or 0.95 ppm to 95 ppm. The peak maxima at 430 nm were plotted versus phosphate concentration in Figure 4.6D, showing a linear trend. The emission spectra had a noticeable decrease in fluorescence intensity even for the 0.95 ppm PO_4 sample, positioning the platform to be competitive with other anion AIE sensors that measure down to the micromolar range.

4.3.6 Discussion Comparing PAMs to Current AIE Materials

It is worthwhile to briefly discuss how PAMs as a new AIE material compare to and enhance the robust AIE material landscape, particularly for bio-related and sensing AIE materials. For a more thorough background, the reader is referred to a recently published review on biomacromolecule AIE platforms which includes a section on bio-related sensing.[114] A primary difference is the lower QY of these initial PAM systems compared to some other AIE systems, especially those with aromatic components, which can be 10% and higher. The PAM QY of future designs could be enhanced through several means, including increasing the peptide segment length, optimizing the packed state of Region 2, covalently tethering the micelle cores through straightforward click chemistry to reduce molecule motion, or incorporating aromatic amino acids such as tryptophan to enhance AIE. An enhanced QY would make PAMs more readily usable for bioimaging or visualizing targeted drug delivery, and it would likely further enhance the sensitivity for sensing applications.

In terms of advantages, the precise synthetic and structural design control of PAMs are significant. The aforementioned review states, "To date, polymers with precise number of AIEgens are rare… Development of precise and defined AIE-active biomacromolecules can greatly speed up their biorelated applications."[114] Traditional synthetic approaches add AIEgens as side-chain pendants to polymer backbones, often with a lack of specificity and control.[131] The sequence-specific synthesis of PAMs and their precise tunability to control aggregate structure uniquely sets PAMs apart as an AIE platform.

AIE future directions also largely hinge upon functionalization and stimuli-responsiveness. Other AIE materials have demonstrated stimuli-responsive behavior through unique avenues such as reaction moieties placed in the polymer backbone.[132] PAMs allow for protein-inspired function to be seamlessly incorporated directly into the AIE material, opening up exciting avenues related to many known peptide-targeting moieties. PAMs are also water-soluble, highly stable, environmentally benign, and biocompatible, all forward-looking goals for AIEgen development.

4.4. Conclusions and Future Outlook

Peptide amphiphile micelles, a material that has been widely studied and applied for more than two decades, were discovered to be a new AIE material platform that features precise synthetic control, self-assembling tunability, and bio-inspired functionality. The absorbance, excitation, and emission properties were consistent with previously identified AIE systems that utilize amides as the emission pathways. The fluorescence critical micelle concentration was found to be approximately 1.5 orders of magnitude higher than the true critical micelle concentration, suggesting that a critical number of PAs must be assembled into the micelle to display AIE. $C_{16}G_5$hex had the highest quantum yield of the three peptide amphiphile micelles tested, which was attributed to the random coil arrangement of the peptide chains in the micelle corona and the

increased number of emission pathways due to a higher number of amino acid residues being present. This direct impact of tuning molecular factors to impact AIE presents peptide amphiphile micelles as a highly engineerable AIEgen. $C_{16}G_5$hex was then evaluated as a phosphate-sensing AIE material by harnessing a protein-extracted binding sequence, and it was able to detect phosphate by utilizing a second-order aggregation stimulus down to a sensitivity of 1 ppm phosphate. Overall, this work demonstrates that pairing synthetic protein mimicry with intrinsic AIE fluorescence opens up a wide array of new AIE applications for this already well-characterized and highly tunable material.

CHAPTER 5.

SUMMARY AND FUTURE OUTLOOK

5.1. SUMMARY AND CONCLUSIONS

This thesis described the design, synthesis, and characterization of a novel protein-inspired material platform based on peptide amphiphile micelles that was able to selectively and reversibly bind to phosphate. The prototype design was put forth in Chapter 2. From there, a more thorough fundamental understanding of the binding mechanisms of the system was described in Chapter 3. Then Chapter 4 described a newly discovered material property of the system and its natural application in stimuli-responsive sensing. The primary conclusions from this work are as follows: (1) binding mechanisms used by proteins can be repurposed and engineered in to synthetic materials, (2) there is opportunity to enhance this design using flexible and interactive peptide material designs that not restricted by traditional protein binding mechanisms, and (3) this protein-inspired binding material is also intrinsically fluorescent and can signal phosphate binding through emission signal changes. A more detailed summary of each conclusion is presented below.

In Chapter 2, a binding motif called the P-loop was derived from phosphate binding proteins and incorporated into the headgroup of the peptide amphiphile. These PAs self-assembled into wormlike micelles that formed a dense entangled suspension. This network was found to sequester phosphate at pH 6 and release it at pH 2 and 11. It was selective over nitrate and nitrite, and it could be reused up to the seven cycles tested. By using molecular dynamics simulations, we observed that binding at pH 6 was able to be achieved because multiple chains were employed to stabilize the phosphate ion.

Using this multi-chain binding insight, in Chapter 3 we designed multi-component PA micelles that were intended to be a platform to further understand and optimize protein-inspired

binding. Although binding was achieved in the prototype material, the nested cavity conformation was limited in the densely packed micelle corona. Thus, we designed multi-component PA systems with varying ratios of a Binder PA and a Filler PA to sequentially reduce the binding motif density and observe the effect on binding. The results were unexpected, showing that phosphate binding was achieved across all systems, including the pure Filler PA, indicating that binding could be achieved without the sequence-specific nested cavity conformation. With this insight, we designed *de novo* peptide sequences that employed the design principles that we derived from the multi-component system, namely that hydrogen bonding and charge play large roles in sequestering phosphate, and they demonstrated noteworthy phosphate binding ability. Though these platforms were not as selective and could not bind as efficiently as the PA micelles, they offer intriguing insight for how biomimetic materials can be engineered to overcome the highly complex binding mechanisms of proteins in future iterations of design.

Chapter 4 detailed the discovery that peptide amphiphile micelles are intrinsically fluorescent according to the aggregation-induced emission (AIE) effect, and that this platform inherently is a stimuli-responsive sensing material. The AIE properties were evaluated and found to be consistent with similar AIE systems without aromatic rings. When the PA micelles bound to phosphate, second-order aggregation was induced, which intensified the AIE effect. The preliminary sensing results demonstrated a sensitivity level of down to 1 ppm concentration of phosphate. Overall, this discovered AIE phenomenon, when paired with the protein-inspired binding of the PA micelles, elevates the potential deployment of this platform not just for resource reclamation but now also for protein-inspired sensing applications.

5.2. Discussion and Future Outlook

One of this work's main contributions to the field of biomimetic materials is that it offered valuable insight into what factors are involved in mimicking the binding ability of proteins in a stimuli responsive absorbent material. We proved that binding to phosphate can occur by PA micelles, but we also uncovered binding principles that were used by this system that are not accessible to conformationally constrained proteins. While this work began as a protein-derived, sequence-specific material design, it became clear as the binding mechanism was elucidated that this system in some ways is also akin to a polyelectrolyte design study.

As discussed throughout this work, peptide amphiphiles have been traditionally used for their targeting ability of larger biomolecules such as antibodies or cell receptors. One of the distinct aspects of this work was that PAs were repurposed to target small molecules on the ion-scale to become a protein-inspired absorbent material. Phosphate, a small molecule, was chosen due to its value in the environmental economy and also because it was a straightforward test case, with an easily extractable P-loop sequence to extract and evaluate within the larger construct of a micelle. But through our work, we discovered that mimicking protein binding of small charged molecules by a densely charged supramolecular object becomes a complex fusion of protein-derived binding factors—conformation, charge, and hydrogen bonding—as well as entropically driven binding factors, which is inaccessible to typical proteins. And when you introduce polyelectrolyte-akin entropic binding influence, the specificity of binding featured by proteins becomes more difficult to retain.

When considering this finding in terms of future directions, there are several potential avenues for next spheres of study. First, this platform could be more fully explored exclusively as a polyelectrolyte-akin material system for targeting small charged molecules, dismissing the

sequence-specific protein interactions. This material is intriguing for this purpose because it is highly tunable in terms of amino acid control and self-assembled construct, thereby offering straightforward design and modification. It also presents a very high density of binding contributors in a localized environment, which allows multiple chains to interact with a single ion. This level of density is difficult to emulate in polymers or brush systems.

Second, one could redesign the PA micelle system to minimize nonspecific binding and restore sequence-specific protein-derived interactions for small charged molecules. Though the multi-component micelles described in Chapter 3 sought to reclaim this protein-inspired conformation, the system ultimately disregarded the nested cavity conformation. Instead, the system favored utilizing the terminal lysine residue amines of the Filler PA for phosphate binding, prompting non-specific multi-chain interactions. A redesign of the system could replace or shield these positive charges by adding additional glycine residues, and it could include a much longer spacer in the Binding PA to sufficiently distance the P-loop sequence from non-specific interference. By several simple design alterations for this highly tunable system, the small protein-binding motif would be forced to mimic the protein-derived binding mechanism, which is likely more specific, thereby restoring protein specificity for small ions by PA micelles.

Third, the target of the PA micelle system could be exchanged for a larger molecule that requires sequence-specificity in order to be bound, where conformation is critical and where these protein-analogous materials would be especially suited to be used. There has been extensive work in determining binding motifs for specific targets by proteins. Utilizing one of these to target a more complex molecule than a phosphate ion would be another straightforward approach to restoring protein specificity of binding.

Finally, a more ambitious goal for this system would be to very strategically utilize this multi-chain binding for more complex targets. While the multi-chain binding of phosphate was originally unintentional, it is intriguing to consider computationally inspired system design for a multi-component PA micelle system, with a Filler PA and two or more complementary Binding PAs that are controllably distributed along the micelle to adopt a multiple pronged binding scheme that is truly reminiscent of complex tertiary binding. Again, the highly tunable nature of this material, as well as the inherent protein-derived building blocks, positions this material for complex protein-inspired design that would be difficult to mimic in other synthetic systems.

The final point of discussion on this material is its potential to be translated for real-world application. Though two potential applications are put forth, namely resource recovery and detection, the PA micelle materials is more readily applicable to the latter than the former.

In order for a material like this to be deployable on the kilogram scale for resource recovery from wastewater, a few things need to be considered. First, the production needs to be cost-effective. While there have been strides to significantly scale-up the synthesis of peptides, such as utilizing recombinant technologies, this technique has yet to be realized in a cost-effective manner. Second, the material platform would need to be more mechanically robust and likely covalently tethered so that the micelles would remain intact in dilute solution. Initially, we attempted to engineer a robust hydrogel material using the already characterized C_{16}SGKGHhex material, which is a self-supporting hydrogel with appealing mechanical properties. In the two systems tested in Chapter 2, neither had comparable mechanical robustness. They were viscous, but they fell short of the strength of a self-supporting hydrogel. By covalently tethering the micelle components, material loss would be prevented and its durability as an absorbent material would

increase. And finally, the selectivity and specificity of the platform would need to be improved, using any of the techniques discussed previously in this section.

While there are more hurdles to overcome to deploy this material for resource recovery in complex wastewater solutions, there is more immediate promise in this material being used for detection and sensing applications. Scale-up and mechanical robustness are factors that are not nearly as important to optimize for these applications, since less material would be required for small-scale sensors and they would not require mechanical robustness needed for high throughput of wastewater. The primary factors to optimize for this application would be increasing specific binding performance and enhancing the emissive properties so that less material would be needed in sensing devices. Overall, by combining this fluorescence feature with the high tunability of protein-inspired binding, there is rich opportunity moving forward to explore this platform for protein-inspired sensing applications.

APPENDIX A.

SUPPLEMENTARY DATA FOR CHAPTER 2

A.1 MASS SPECTROSCOPY VERIFICATION USING MATRIX-ASSISTED LASER DESORPTION-IONIZATION – TIME OF FLIGHT (MALDI-TOF)

The theoretical molecular weight for C_{16}GGGhex is 928.10 g/mol. The main peak in the purified HPLC fraction is 950.698 (Figure A.1A). An artifact of this technique is that a sodium ion commonly adheres to the molecule in the place of a hydrogen atom upon ionization, making the detected mass larger than the mass of the molecule. After subtracting the molecular weight of a sodium ion (22.99 g/mol) and adding back the mass of the hydrogen atom it replaced, the confirmed molecular weight of C_{16}GGGhex is 928.72 g/mol. Similarly, for C_{16}SGKGHhex, the theoretical weight is 2288.55 g/mol. After subtracted the mass of sodium and adding the mass of hydrogen, the confirmed molecular weight of C_{16}SGKGHhex is 2287.37 g/mol (Figure A.1B).

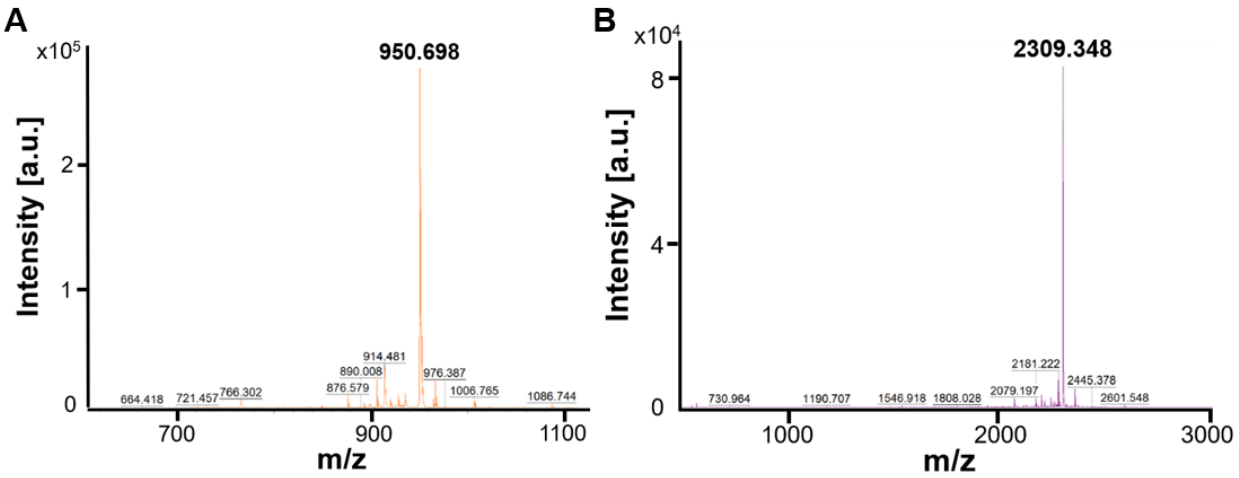

Figure A.1. The mass spectra for (A) C_{16}GGGhex and (B) C_{16}SGKGHhex after purification from HPLC.

A.2 Purity Analysis using Liquid Chromatography – Mass Spectroscopy (LC-MS)

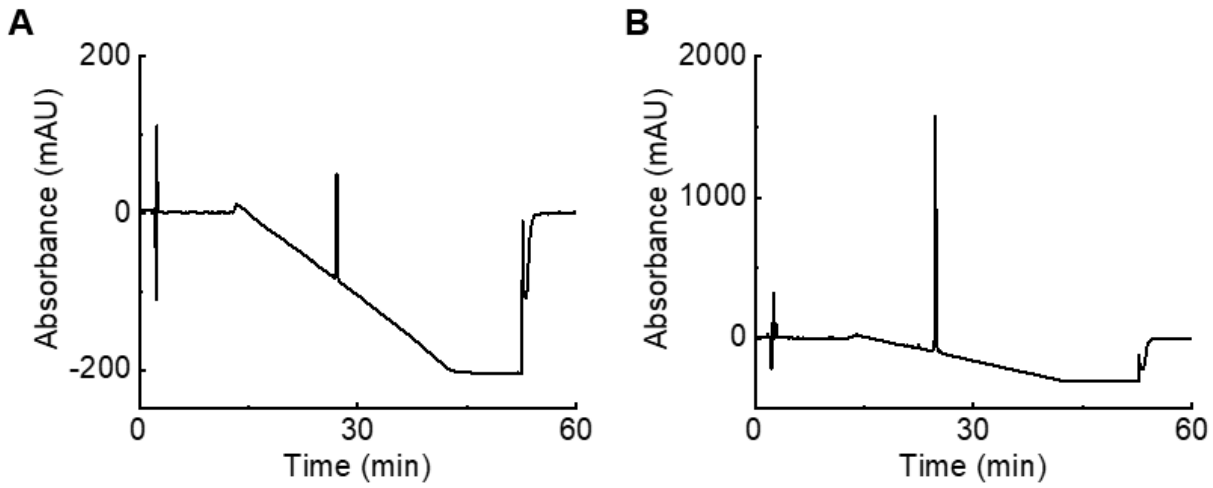

Figure A.2. LC-MS chromatogram of (A) C_{16}GGGhex and (B) C_{16}SGKGHhex at 220 nm. The product elutes in the center peak for each plot. The purities were calculated to be (A) 96.5% and (B) 97.3%.

Table A.1. LC-MS Chromatogram peak table for C_{16}GGGhex

Peak #	Ret. Time [min]	Area [mAU*s]	Height [mAU]	New Area [%]
1	7.075	17.42218	1.10176	1.81%
2	26.603	16.72878	1.79469	1.74%
3	**27.115**	**929.08282**	**134.86389**	**96.45%**
Total		19711.92	1744.347	100.00%

Table A.2. LC-MS Chromatogram peak table for C_{16}SGKGHhex

Peak #	Ret. Time [min]	Area [mAU*s]	Height [mAU]	New Area [%]
1	15.06	71.84814	3.26691	0.36%
2	16.16	50.0343	3.10221	0.25%
3	17.457	16.36457	2.35443	0.08%
4	18.007	5.32924	1.11091	0.03%
5	18.234	33.99007	1.75981	0.17%
6	19.27	28.48297	4.28034	0.14%
7	19.704	12.98752	2.0538	0.07%
8	19.964	16.9283	2.95362	0.09%
9	20.449	30.83108	2.91836	0.16%
10	22.018	6.64445	1.70828	0.03%
11	22.312	5.37997	1.35502	0.03%
12	22.411	58.5399	15.22104	0.30%
13	22.538	63.15965	14.43723	0.32%
14	23.886	14.48648	1.14472	0.07%
15	**24.728**	**1.92E+04**	**1668.184**	**97.30%**
16	25.306	42.21921	7.38365	0.21%
17	25.446	12.94693	2.46567	0.07%
18	25.702	28.63228	4.45938	0.15%
19	26.481	8.51018	1.46951	0.04%
20	28.191	8.36704	1.13123	0.04%
21	29.378	15.93975	1.58721	0.08%
Total		19711.92	1744.347	100.00%

The confirmed purity of C_{16}GGGhex was 96.45%, and the confirmed purity of C_{16}SGKGHhex was 97.30%.

A.3 Critical Micelle Concentration (CMC)

The CMC is calculated as the inflection point of the fluorescence intensity beginning to increase, which occurs in the presence of hydrophobic cores (Figure A.3). The CMCs were 8.43 μM and 130.1 μM for C16GGGhex and C16SGKGHhex, respectively. The ten-fold difference in CMC values can be explained by the packing parameter for surfactant molecules.[84] The packing parameter *P* evaluates the most stable degree of curvature at the tail-headgroup interface of the micelle using the ratio $P = v/al$, where (v) and (l) are the volume and maximum extended length of the tail, respectively, and (a) is the area of the headgroup at the interface. For C_{16}SGKGHhex, the (a) area of the headgroup is much larger due to the double-sided headgroup, causing each PA

molecule to face more steric constraints in its ability to self-assemble, corresponding to the higher CMC. C_{16}SGKGHhex is also much more hydrophilic than C_{16}GGGhex with more than double the number of amino acids in the headgroup, further stabilizing the individual PA molecules in an unassembled state.

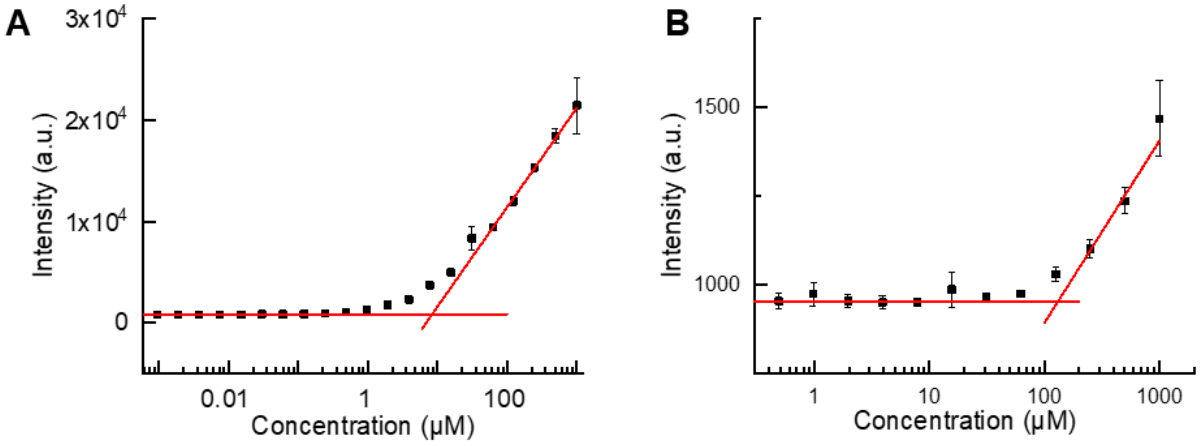

Figure A.3. The CMC plots of (A) C_{16}GGGhex and (B) C_{16}SGKGHhex.

A.4 Additional Negative-Stain Transmission Electron Microscopy (TEM) Imaging

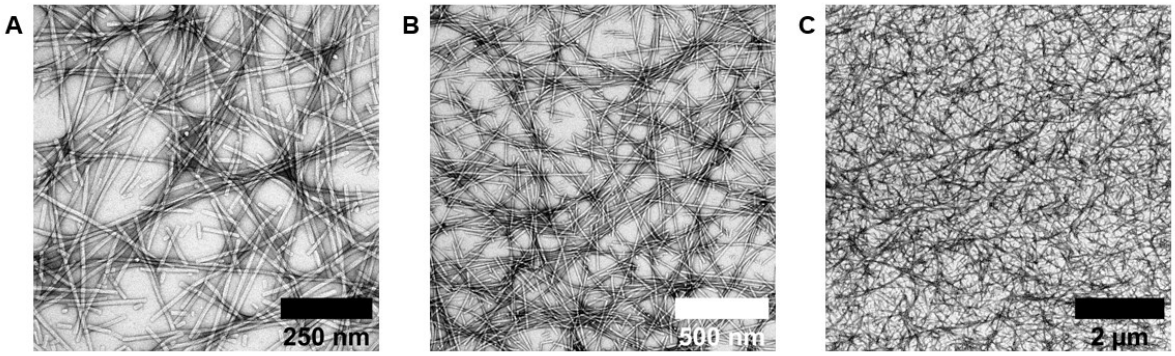

Figure A.4. C_{16}GGGhex at pH 2 forms extended wormlike micelles.

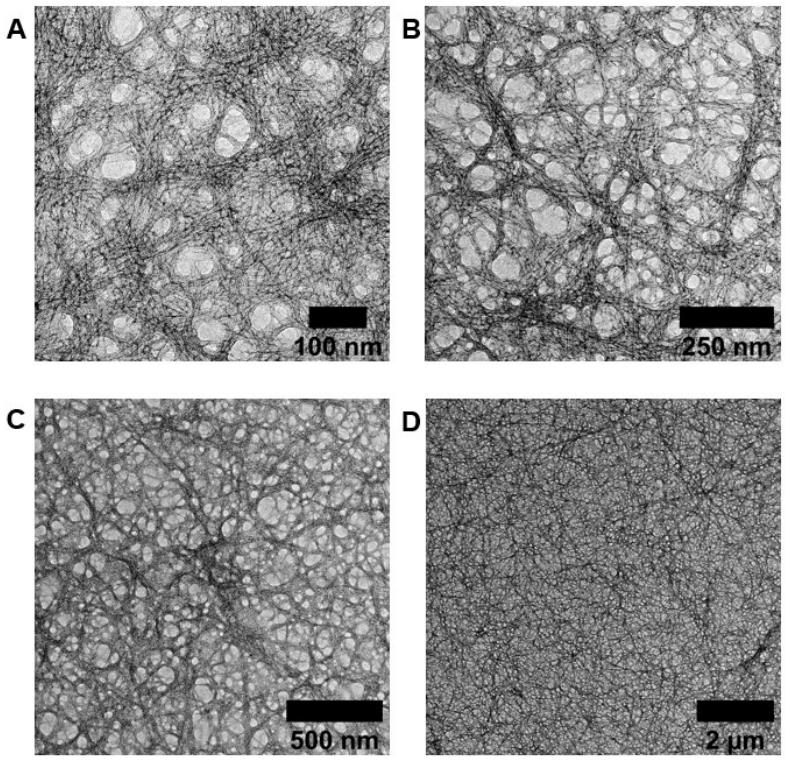

Figure A.5. C_{16}GGGhex at pH 6 forms extended wormlike micelles.

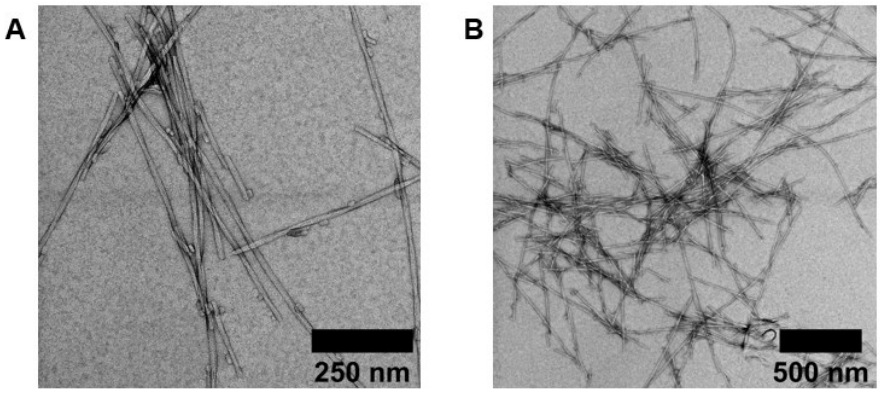

Figure A.6. C_{16}GGGhex at pH 10 forms wormlike micelles that begin to clump together.

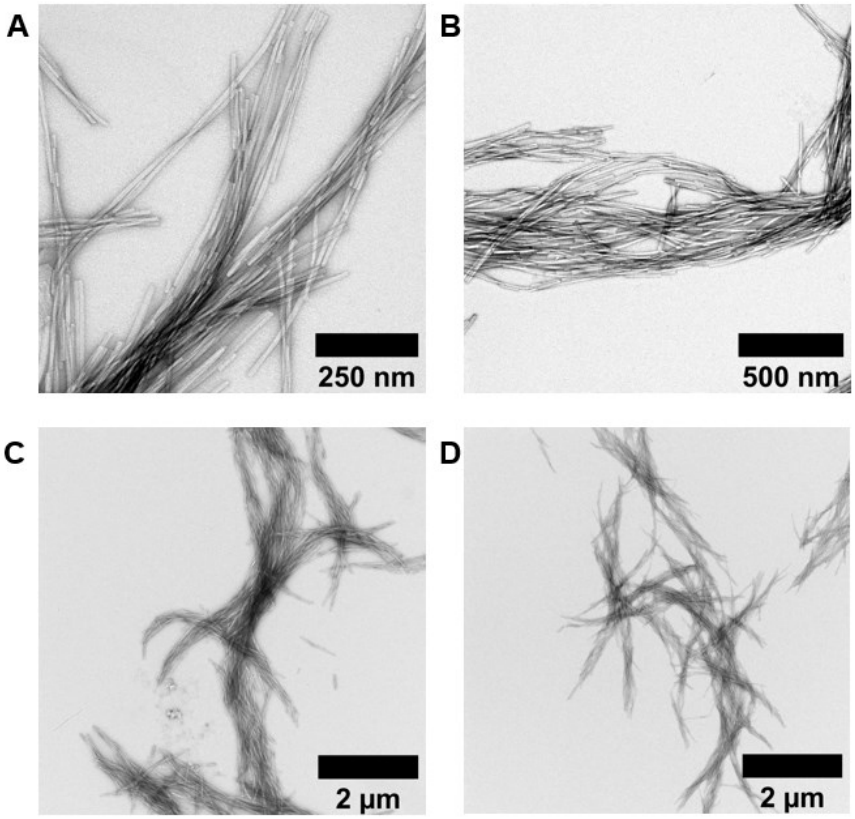

Figure A.7. C_{16}GGGhex at pH 11 forms wormlike micelles that heavily clump together.

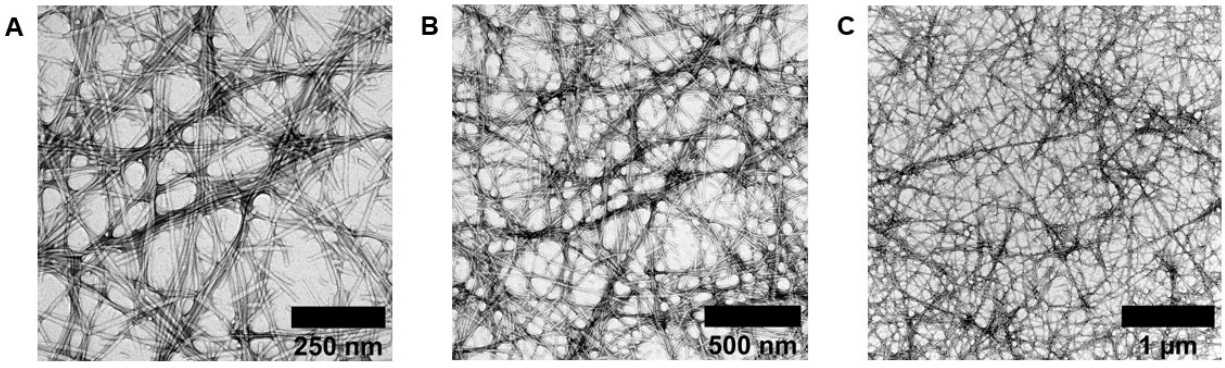

Figure A.8. C_{16}GGGhex at pH 6 after one cycle of capture and release at pH 11 demonstrates that the declumping of the micelles is reversible.

For C_{16}SGKGHhex in Figure A.9, this transition at high pH to wormlike micelles from spherical micelles can be understood in terms of the packing parameter discussed above. At low pH, the histidines are protonated, repelling each other and effectively increasing the area of the

headgroup, pushing the packing parameter below the 1/3 value corresponding to spherical micelles to accommodate the larger steric hindrance. Upon deprotonation and a subsequent decrease in headgroup area at high pH, the assembly becomes more stabilized as wormlike micelles and approaches the 1/2 packing parameter value corresponding to the wormlike micelles seen in Figure A.9.

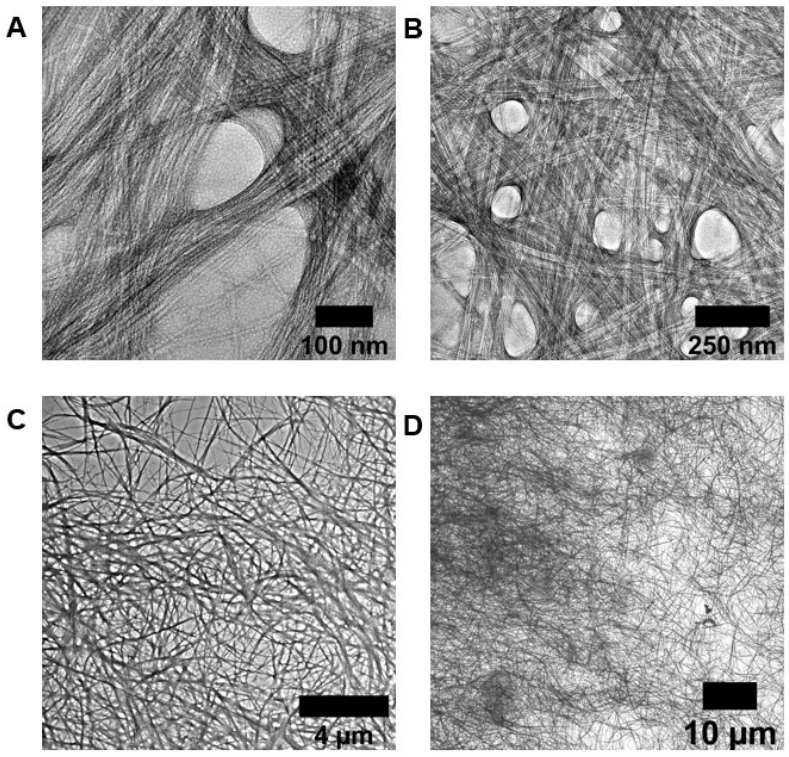

Figure A.9. C_{16}SGKGHhex at pH 10 forms extended wormlike micelles that clump together very thickly.

A.5 Spectrophotometric Molybdenum Blue Assay

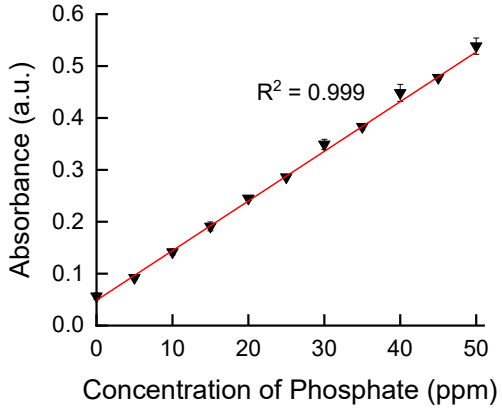

Figure A.10. Confirmation of a linear trend using the spectrophotometric molybdenum blue assay. As concentration of phosphate in solution increases, the absorbance increases with very reliable accuracy.

A.6 Analysis of Kinetics of Binding

The kinetics data shown in Figure A.11 demonstrated that C_{16}GGGhex sequestered and released phosphate within seconds to minutes of reaching the target pH, corresponding to the time it requires to promptly filter the suspension and evaluate the phosphate content. Additionally, the material maintains its unbound or bound state as long as the pH remains constant, up to the two hours that we tested

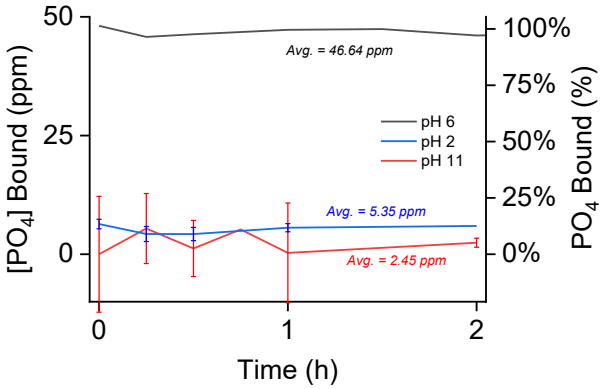

Figure A.11. The phosphate binding concentrations and percentages measured over time at the three pH values of 6, 2, and 11. Phosphate is captured at pH 6 and unbound at pH 2 and 11 over the two hours measured.

A.7 Effect of Increased NaCl on Binding and the Molybdenum Blue Assay

As more NaCl is added to binding experiments of C_{16}GGGhex at pH 6, the amount of phosphate binding noticeably decreases (Figure A.12). This phenomenon could explain the slight decrease in binding after multiple cycles of capture and release as the pH was repeatedly altered, if for example the wash steps between cycles did not completely wash out all NaCl and the concentration NaCl gradually accumulated in the sample as the number of cycles increases. This effect of decreased hexapeptide binding by an increase in NaCl concentration was also observed by Zhai, et al.[82]

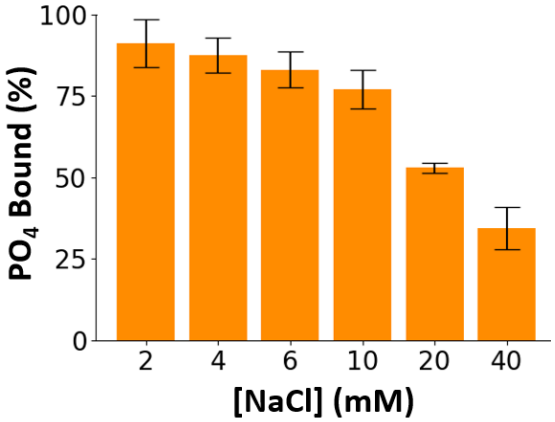

Figure A.12. Binding experiments of C_{16}GGGhex at pH 6 at a 5:1 ratio of PA:PO_4 and varying final solution concentrations of NaCl.

We also investigated whether these higher concentrations affected the spectrophotometric assay to confirm that the observed decrease in binding was not an artifact of the assay (Figure A.13). As the concentration of NaCl increases in the spectrophotometric calibration curves, the fitted lines do not noticeably vary or follow any noticeable trend, implying that added NaCl does not affect the spectrophotometric readings at these concentrations.

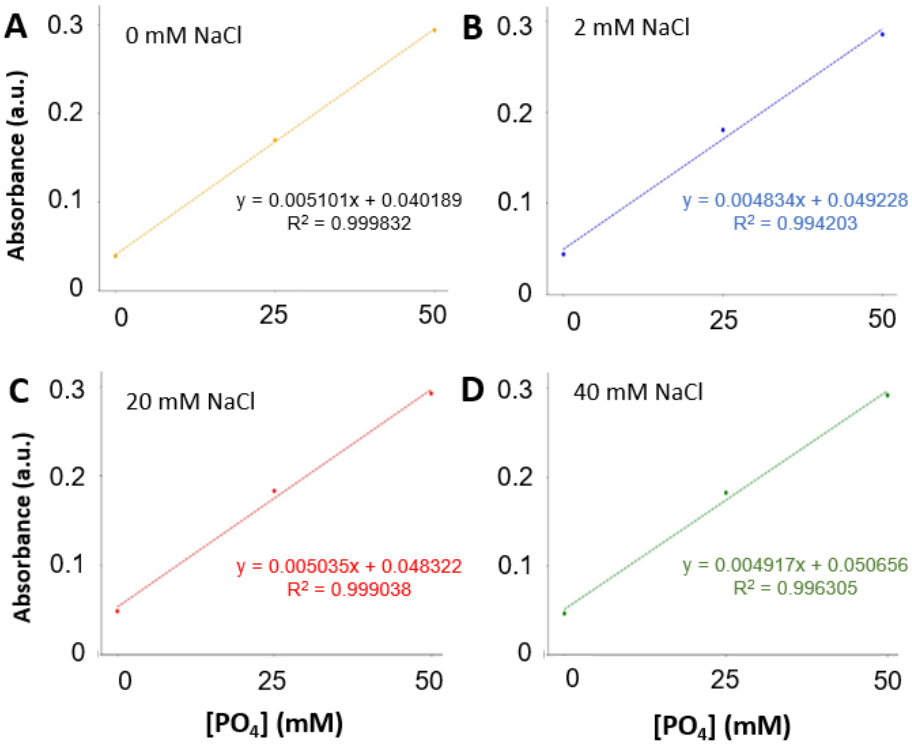

Figure A.13. Spectrophotometric calibration curves constructed with increasing amounts of added NaCl, from (A) 0 mM NaCl, (B) 2 mM NaCl, 20 mM NaCl, and (D) 40 mM NaCl.

Even though we confirmed that binding is impacted by increased NaCl, the impact for our material is relatively small at the pH extremes. Table A.3 details the average final concentration of added HCl and NaOH in order to achieve pH 2, 6, and 11 for our binding systems. The release conditions of pH 2 and 11 require concentrations of HCl and NaOH that fall in the range that would impact binding, both near 4 mM of added HCl or NaOH. However, this approximately 12% decrease in binding at pH 6 does not match the roughly 90-95% unbound phosphate at these extremes (Figure 2.3). Thus, we confirm that NaCl interference is not the cause of the observed near zero binding at pH 2 and 11.

Table A.3. Average final concentrations of added HCl and NaOH to achieve the final solution pH

Final pH	[HCl] (mM)	[NaOH] (mM)
2	3.6±0.2	0
6	0	0.2±0.1
11	0	4.6±0.2

A.8 Estimated Potential of Mean Force for Phosphate Micelle Binding

From the phosphate-micelle simulation at pH 6, we estimated the potential of mean force (PMF) profile as a function of separation distance between phosphates and the micelle center. The PMF is obtained *via* the equation $\mathrm{PMF}(r) = \mathrm{kTln}(P(r))$. The PMF profile shown is relative to the PMF at the distance of 8 nm, which corresponds to the unbound state. The PMF shows a minimum at a phosphate-micelle separation distance of approximately 3.5 nm. The PMF difference between this minimum and the unbound state is -11.6 kJ/mol.

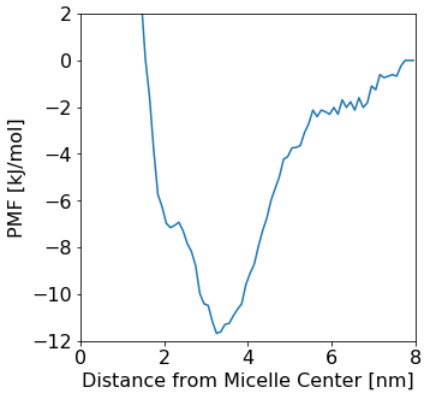

Figure A.14. PMF as a function of the separation distance between phosphates and the micelle central axis. The result is obtained at the condition pH 11 and PA:PO_4 = 5:1.

A.9 Representative Snapshot of Multi-chain Binding

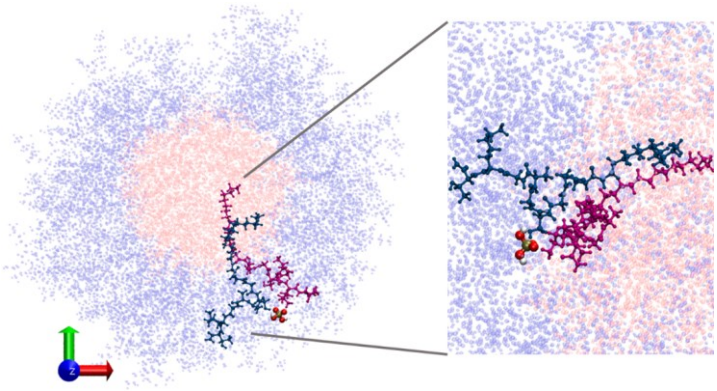

Figure A.15. Representative snapshot of Multi-chain Binding from phosphate-micelle simulation at pH 6. The hydrophobic core is shown in red and the corona is shown in blue. The two different PA chains interacting with the phosphate is shown in dark blue and magenta, respectively.

APPENDIX B.

SUPPLEMENTARY DATA FOR CHAPTERS 3 AND 4

B.1 MASS SPECTROSCOPY VERIFICATION AND PURITY ANALYSIS USING LIQUID CHROMATOGRAPHY–MASS SPECTROSCOPY (LC-MS)

After purification on high performance liquid chromatography (HPLC), the collected fraction containing the purified product was analyzed using LC-MS. The chromatographs (Figure B.1) and the mass spectra of the eluted peak (Figure S2) indicate that the syntheses were successful (see Table B.1). The purification achieved greater than 95% purity for all three samples (Tables B.2-B.4).

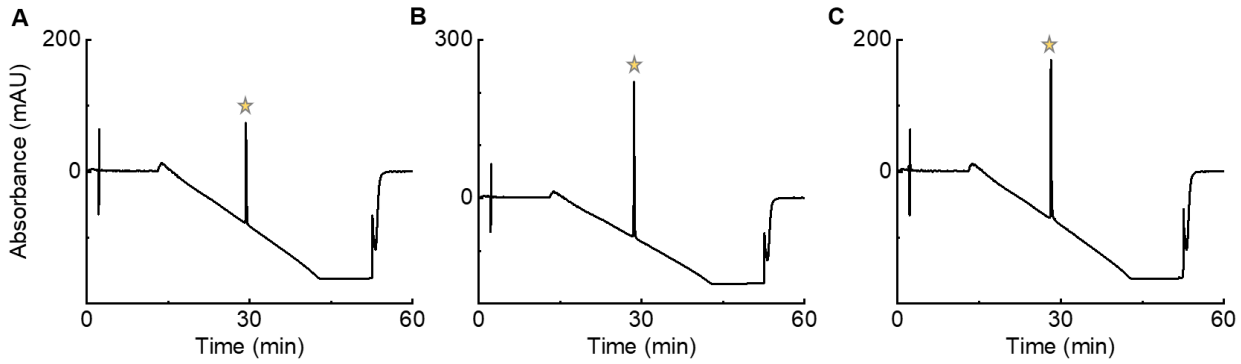

Figure B.1. LC-MS chromatogram at 220 nm UV absorbance of (A) $C_{16}G_5K$, (B) $C_{16}G_5$hex, and (C) $C_{16}S_5$hex. The product elutes in the center peak for each plot.

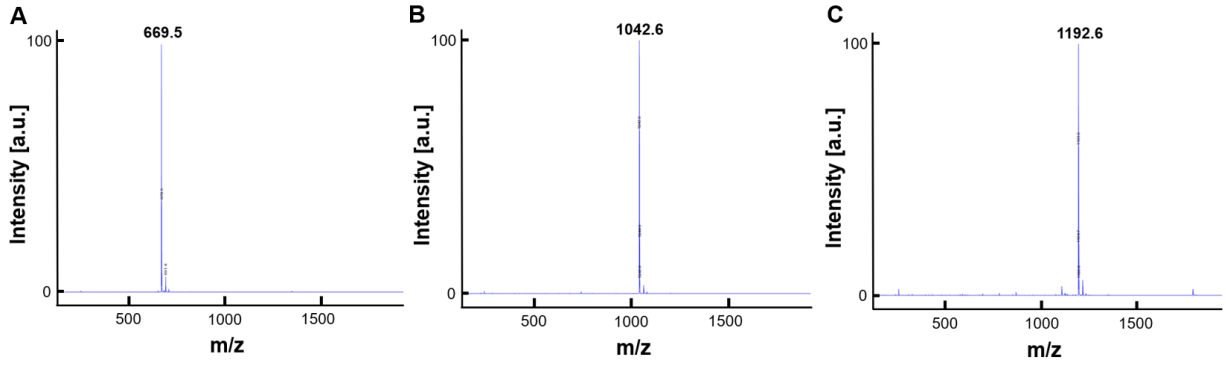

Figure B.2. The mass spectra at the LC-MS center peak for (A) $C_{16}G_5K$, (B) $C_{16}G_5$hex, and (C) $C_{16}S_5$hex after purification from HPLC.

Table B.1. Theoretical and Experimentally Measured Molecular Weights of Three Peptide Amphiphile (PA) Samples

Sample	Theoretical Molecular Weight (g/mol)	Experimentally Measured Molecular Weight on LC-MS (g/mol)
$C_{16}G_5K$	668.8	669.5
$C_{16}G_5hex$	1042.2	1042.6
$C_{16}S_5hex$	1192.3	1192.6

Table B.2. LC-MS Chromatogram peak table for $C_{16}G_5K$

Peak #	Ret. Time [min]	Area [mAU*s]	Height [mAU]	Area [%]
1	14.24228001	30.97977257	1.652881622	2.2%
2	16.94313431	12.77208042	1.306900024	0.9%
3	**29.30536842**	**1386.741699**	**152.6833344**	**96.5%**
4	29.697752	6.706115246	1.231860876	0.5%
Total		1437.199667	156.8749769	100%

Table B.3. LC-MS Chromatogram peak table for $C_{16}G_5hex$

Peak #	Ret. Time [min]	Area [mAU*s]	Height [mAU]	Area [%]
1	14.38019	9.962159	1.059084	0.4%
2	14.80785	25.19563	1.346974	1.0%
3	15.5501	28.60013	2.50615	1.2%
4	17.6879	19.15074	1.238985	0.8%
5	**28.58741**	**2364.111**	**294.5662**	**96.6%**
Total		2447.02	300.72	100%

Table B.4. LC-MS Chromatogram peak table for $C_{16}S_5hex$

Peak #	Ret. Time [min]	Area [mAU*s]	Height [mAU]	Area [%]
1	14.30829	52.81527	1.755722	4.2%
2	**28.19699**	**1211.203**	**214.2246**	**95.1%**
3	28.92766	9.714286	1.941672	0.8%
Total		1273.73	217.92	100%

The confirmed purities of $C_{16}G_5K$, $C_{16}G_5hex$, and $C_{16}S_5hex$ are 96.5%, 96.6%, and 95.1% respectively. This was calculated according to the area of each peak that eluted during the solvent gradient change from water with trifluoroacetic acid to acetonitrile. The area of the peak corresponds to the amount of that product present in the sample.

B.2 Additional TEM Images of Pure PA Micelles

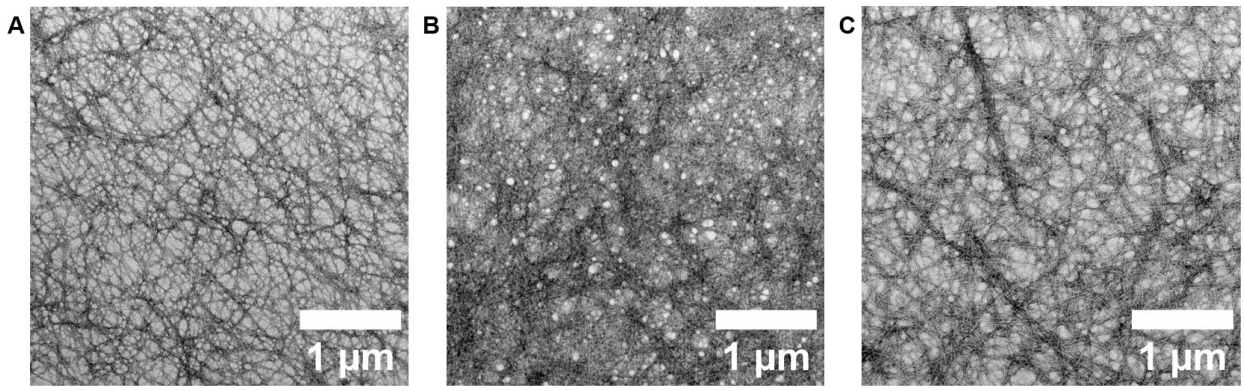

Figure B.3. Negative-stain transmission electron microscopy at longer length scales for (A) $C_{16}G_5K$, (B) $C_{16}G_5$hex, and (C) $C_{16}S_5$hex confirm extended wormlike micelles.

B.3 Absorption, Excitation, Emission, and CMC Data for $C_{16}G_5K$ and $C_{16}S_5$HEX

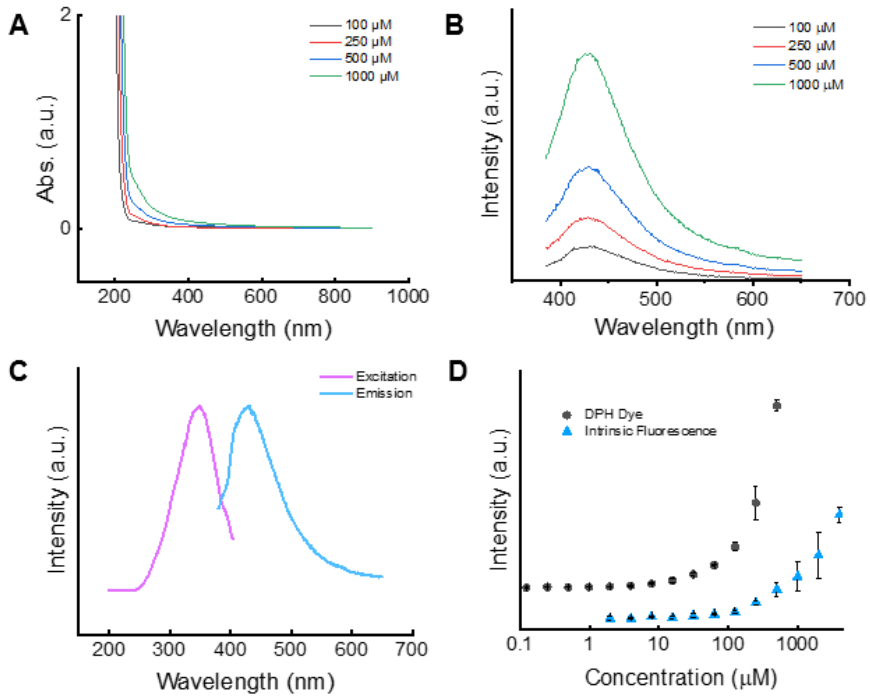

Figure B.4. Fundamental fluorescence characterization data for $C_{16}G_5K$, including (A) absorbance intensity, (B) the fluorescent emission intensity at an excitation of 355 nm, (C) an excitation scan at 430 nm emission and emission scan at 355 nm excitation, and (D) the critical micelle concentration (CMC) using 1,6-diphenyl-1,3,5-hexatriene (DPH) dye and the intrinsic fluorescence critical micelle concentration. Note: the FCMC data are shifted down and scaled by 10 to emphasis the inflection point shift.

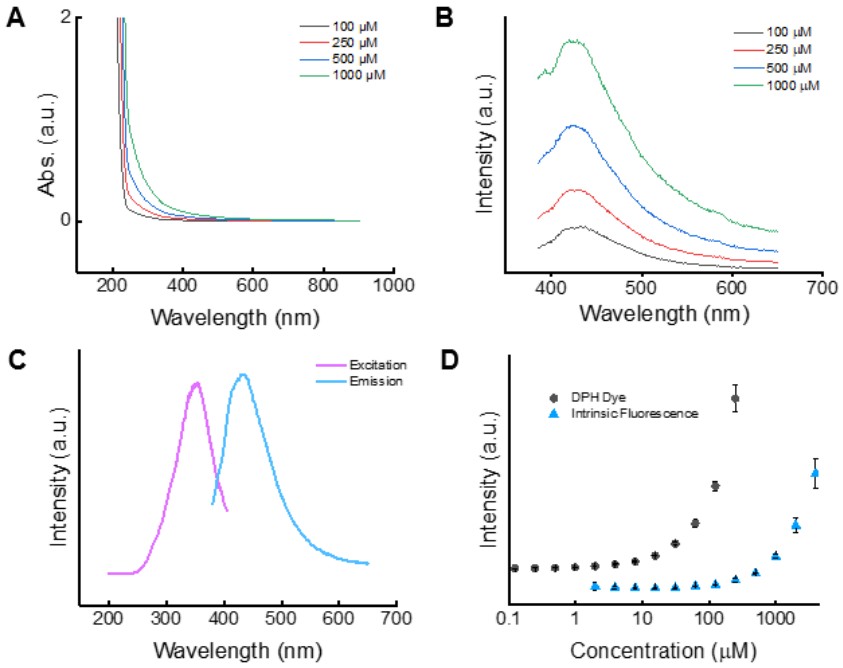

Figure B.5. Fundamental fluorescence characterization data for $C_{16}S_5$hex, including (A) absorbance intensity, (B) the fluorescent emission intensity at an excitation of 355 nm, (C) an excitation scan at 430 nm emission and emission scan at 355 nm excitation, and (D) the critical micelle concentration (CMC) using 1,6-diphenyl-1,3,5-hexatriene (DPH) dye and the intrinsic fluorescence critical micelle concentration. Note: the FCMC data are shifted down and scaled by 10 to emphasis the inflection point shift.

B.4 Quantum Yield Calculations

The quantum yield (QY) for each PA sample was calculated according to the equation

$$\Phi_{PA} = \Phi_{QS}\left(\frac{Slope_{PA}}{Slope_{QS}}\right)\left(\frac{\eta_{PA}^2}{\eta_{QS}^2}\right)$$

where Φ_{PA} is the QY of the peptide amphiphile, Φ_{QS} is the QY of the standard, $Slope_{PA}$ and $Slope_{QS}$ are the slopes from the plots of fluorescence intensity vs. absorbance for the PAs and the standard, respectively, and η_{PA}^2 and η_{QS}^2 are the refractive indexes for the solvents for the PA sample and the standard, respectively. The standard used was quinine sulfate in 0.1 M H_2SO_4, which had a comparable emission range as the PA micelles. The absorbance and fluorescence intensities were calculated for samples in the linear regime (Figure S6), ensuring that the slit widths

remained constant between measurements and samples. The reference quantum yield for the standard was 0.54, and the refractive indexes for both solvents were 1.33.

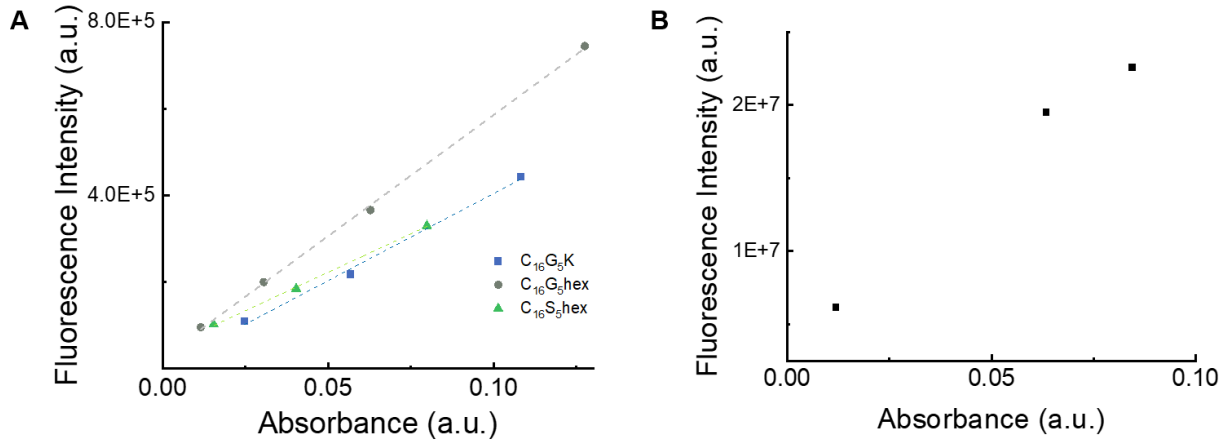

Figure B.6. Quantum yield measurements show linear correlations for absorbance vs. fluorescence intensity for (A) all three PA systems and (B) quinine sulfate with an R^2 value of over 0.99 for all four linear fits.

B.5 Circular Dichroism Spectra Fitted Curves

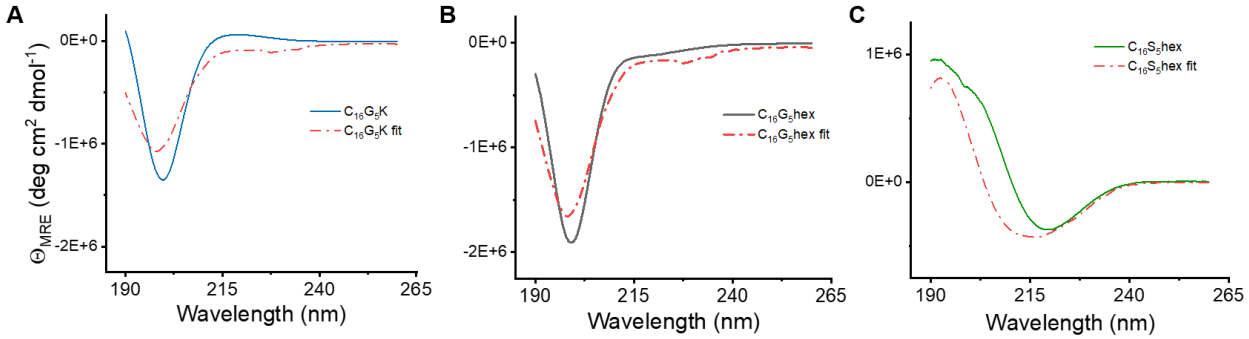

Figure B.7. Circular Dichroism spectra and their fitted curves for (A) $C_{16}G_5K$, (B) $C_{16}G_5$hex, and (C) $C_{16}S_5$hex.

Table B.5. Fitted Curve Values for $C_{16}G_5K$, $C_{16}G_5$hex, and $C_{16}S_5$hex.

Sample	Alpha Helix (%)	Beta Sheet (%)	Random Coil (%)
$C_{16}G_5K$	0	30.3	69.7
$C_{16}G_5$hex	0	28.4	71.6
$C_{16}S_5$hex	0	100	0

B.6 Additional TEM Images of PA Micelles with Phosphate

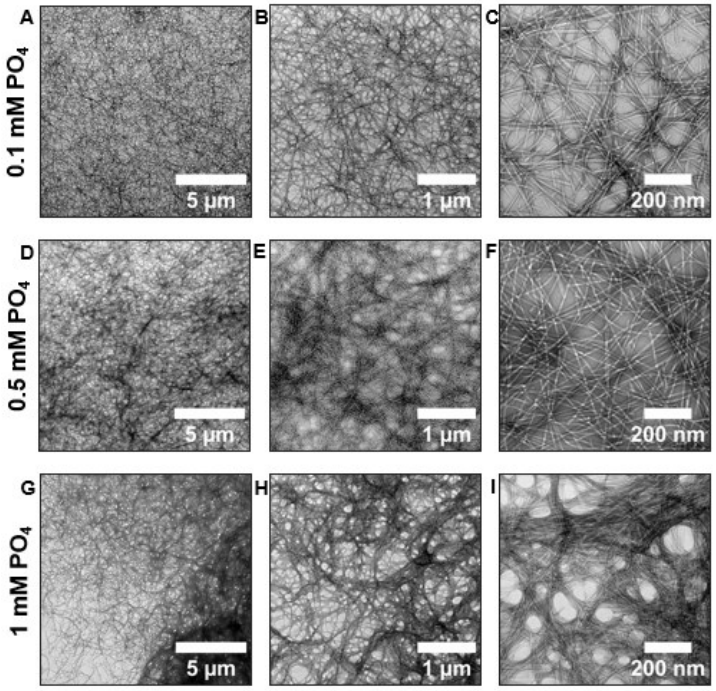

Figure B.8. Negative-stain TEM images for $C_{16}G_5K$ with increasing amounts of phosphate added.

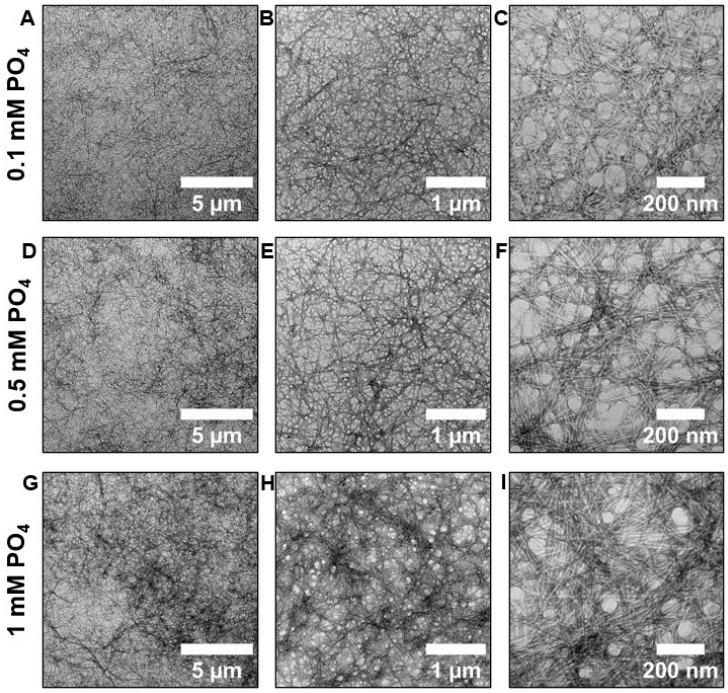

Figure B.9. Negative-stain TEM images for $C_{16}S_5$hex with increasing amounts of phosphate added.

REFERENCES

(1) Tamerler, C.; Sarikaya, M. Genetically Designed Peptide-Based Molecular Materials. *ACS Nano* **2009**, *3*.

(2) Dimarco, R. L.; Heilshorn, S. C. Multifunctional Materials through Modular Protein Engineering. *Advanced Materials*. 2012.

(3) Hamley, I. W. Small Bioactive Peptides for Biomaterials Design and Therapeutics. *Chem. Rev.* **2017**, *117*, 14015–14041.

(4) Elias, M.; Wellner, A.; Goldin-Azulay, K.; Chabriere, E.; Vorholt, J. A.; Erb, T. J.; Tawfik, D. S. The Molecular Basis of Phosphate Discrimination in Arsenate-Rich Environments. *Nature* **2012**, *491*, 134–137.

(5) Ananthanarayanan, B.; Little, L.; Schaffer, D. V.; Healy, K. E.; Tirrell, M. Neural Stem Cell Adhesion and Proliferation on Phospholipid Bilayers Functionalized with RGD Peptides. *Biomaterials* **2010**, *31*, 8706–8715.

(6) O'Leary, L. E. R.; Fallas, J. A.; Bakota, E. L.; Kang, M. K.; Hartgerink, J. D. Multi-Hierarchical Self-Assembly of a Collagen Mimetic Peptide from Triple Helix to Nanofibre and Hydrogel. *Nat. Chem.* **2011**, *3*, 821–828.

(7) Chu-Kung, A. F.; Bozzelli, K. N.; Lockwood, N. A.; Haseman, J. R.; Mayo, K. H.; Tirrell, M. V. Promotion of Peptide Antimicrobial Activity by Fatty Acid Conjugation. *Bioconjug. Chem.* **2004**, *15*, 530–535.

(8) Huang, T.; Qian, Y.; Fu, X.; Huang, S.; Li, Y.; Zhou, C. De Novo Design of Triblock Amphiphilic Short Antimicrobial Peptides. *ACS Appl. Polym. Mater.* **2020**, *2*, 3988–3992.

(9) Wang, K. F.; Nagarajan, R.; Camesano, T. A. Differentiating Antimicrobial Peptides Interacting with Lipid Bilayer: Molecular Signatures Derived from Quartz Crystal

Microbalance with Dissipation Monitoring. *Biophys. Chem.* **2015**, *196*, 53–57.

(10) Acar, H.; Ting, J. M.; Srivastava, S.; LaBelle, J. L.; Tirrell, M. V. Molecular Engineering Solutions for Therapeutic Peptide Delivery. *Chem. Soc. Rev.* **2017**, *46*, 6553–6569.

(11) Lin, B. F.; Megley, K. A.; Viswanathan, N.; Krogstad, D. V.; Drews, L. B.; Kade, M. J.; Qian, Y.; Tirrell, M. V. PH-Responsive Branched Peptide Amphiphile Hydrogel Designed for Applications in Regenerative Medicine with Potential as Injectable Tissue Scaffolds. *J. Mater. Chem.* **2012**, *22*, 19447.

(12) Black, K. A.; Lin, B. F.; Wonder, E. A.; Desai, S. S.; Chung, E. J.; Ulery, B. D.; Katari, R. S.; Tirrell, M. V. Biocompatibility and Characterization of a Peptide Amphiphile Hydrogel for Applications in Peripheral Nerve Regeneration. *Tissue Eng. Part A* **2015**, *21*, 1333–1342.

(13) Álvarez, Z.; Kolberg-Edelbrock, A. N.; Sasselli, I. R.; Ortega, J. A.; Qiu, R.; Syrgiannis, Z.; Mirau, P. A.; Chen, F.; Chin, S. M.; Weigand, S.; Kiskinis, E.; Stupp, S. I. Bioactive Scaffolds with Enhanced Supramolecular Motion Promote Recovery from Spinal Cord Injury. *Science (80-.).* **2021**, *374*, 848–856.

(14) Peters, D.; Kastantin, M.; Kotamraju, V. R.; Karmali, P. P.; Gujraty, K.; Tirrell, M.; Ruoslahti, E. Targeting Atherosclerosis by Using Modular, Multifunctional Micelles. *Proc. Natl. Acad. Sci. U. S. A.* **2009**, *106*, 9815–9819.

(15) Mlinar, L. B.; Chung, E. J.; Wonder, E. A.; Tirrell, M. Active Targeting of Early and Mid-Stage Atherosclerotic Plaques Using Self-Assembled Peptide Amphiphile Micelles. *Biomaterials* **2014**, *35*, 8678–8686.

(16) Su, Z.; Hostert, J. D.; Renner, J. N. Phosphate Recovery by a Surface-Immobilized Cerium Affinity Peptide. *ACS ES&T Water* **2020**, *1*.

(17) Saylan, Y.; Erdem, Ö.; Inci, F.; Denizli, A. Advances in Biomimetic Systems for Molecular Recognition and Biosensing. *Biomimetics* **2020**, *5*.

(18) Lee, J. H.; Jin, H. E.; Desai, M. S.; Ren, S.; Kim, S.; Lee, S. W. Biomimetic Sensor Design. *Nanoscale* **2015**, *7*, 18379–18391.

(19) Yao, L.; Sun, Y. T.; Sun, W.; Xu, T. H.; Ren, C.; Fan, X.; Sun, L.; Liu, L. L.; Feng, J. M.; Ma, J. F.; Wang, L. N. High Phosphorus Level Leads to Aortic Calcification via β-Catenin in Chronic Kidney Disease. *Am. J. Nephrol.* **2015**, *41*, 28–36.

(20) Zhang, L.; Zhang, W. A Protein Engineered to Bind Uranyl Selectively and with Femtomolar Affinity ¨. *Nat. Chem.* **2014**, *6*, 236–241.

(21) Aryal, B. P.; Brugarolas, P.; He, C. Binding of ReO4 2 with an Engineered MoO4 22-Binding Protein: Towards a New Approach in Radiopharmaceutical Applications. *J. Biol. Inorg. Chem.* **2012**, *17*, 97–106.

(22) Romero Romero, M. L.; Yang, F.; Lin, Y. R.; Toth-Petroczy, A.; Berezovsky, I. N.; Goncearenco, A.; Yang, W.; Wellner, A.; Kumar-Deshmukh, F.; Sharon, M.; Baker, D.; Varani, G.; Tawfik, D. S. Simple yet Functional Phosphate-Loop Proteins. *Proc. Natl. Acad. Sci. U. S. A.* **2018**, *115*.

(23) Knight, A. S.; Zhou, E. Y.; Pelton, J. G.; Francis, M. B. Selective Chromium(VI) Ligands Identified Using Combinatorial Peptoid Libraries. *J. Am. Chem. Soc.* **2013**, *135*, 17488–17493.

(24) Knight, A. S.; Zhou, E. Y.; Francis, M. B. Development of Peptoid-Based Ligands for the Removal of Cadmium from Biological Media. *Chem. Sci.* **2015**, *6*, 4042–4048.

(25) Zhong, H.; Yuan, C.; He, J.; Yu, Y.; Jin, Y.; Huang, Y.; Zhao, R. Engineering Peptide-Functionalized Biomimetic Nanointerfaces for Synergetic Capture of Circulating Tumor

Cells in an EpCAM-Independent Manner. *Anal. Chem.* **2021**, *93*.

(26) Grant, S. B.; Saphores, J.-D.; Feldman, D. L.; Hamilton, A. J.; Fletcher, T. D.; Cook, P. L. M.; Stewardson, M.; Sanders, B. F.; Levin, L. A.; Ambrose, R. F.; Deletic, A.; Brown, R.; Jiang, S. C.; Rosso, D.; Cooper, W. J.; Marusic, I. Taking the "Waste" Out of "Wastewater" for Human Water Security and Ecosystem Sustainability. *Science (80-.).* **2012**, *337*, 681–686.

(27) WWAP (United Nations World Water Assessment Programme). *The United Nations World Water Development Report 2017. Wastewater: The Untapped Resource*; UNESCO: Paris, 2017.

(28) Van Loosdrecht, M. C. M.; Brdjanovic, D. Anticipating the Next Century of Wastewater Treatment. *Science (80-.).* **2014**, *344*, 1452–1453.

(29) Mo, W.; Zhang, Q. Energy-Nutrients-Water Nexus: Integrated Resource Recovery in Municipal Wastewater Treatment Plants. *J. Environ. Manage.* **2013**, *127*, 255–267.

(30) Liu, C.; Hsu, P. C.; Xie, J.; Zhao, J.; Wu, T.; Wang, H.; Liu, W.; Zhang, J.; Chu, S.; Cui, Y. A Half-Wave Rectified Alternating Current Electrochemical Method for Uranium Extraction from Seawater. *Nat. Energy* **2017**, *2*, 1–8.

(31) De-Bashan, L. E.; Bashan, Y. Recent Advances in Removing Phosphorus from Wastewater and Its Future Use as Fertilizer (1997-2003). *Water Res.* **2004**, *38*, 4222–4246.

(32) Kolpin, D. W.; Furlong, E. T.; Meyer, M. T.; Thurman, E. M.; Zaugg, S. D.; Barber, L. B.; Buxton, H. T. Pharmaceuticals, Hormones, and Other Organic Wastewater Contaminants in U.S. Streams, 1999-2000: A National Reconnaissance. *Environ. Sci. Technol.* **2002**, *36*, 1202–1211.

(33) Gros, M.; Petrović, M.; Ginebreda, A.; Barceló, D. Removal of Pharmaceuticals during Wastewater Treatment and Environmental Risk Assessment Using Hazard Indexes. *Environ. Int.* **2010**, *36*, 15–26.

(34) Le Corre, K. S.; Valsami-Jones, E.; Hobbs, P.; Parsons, S. A. Phosphorus Recovery from Wastewater by Struvite Crystallisation: A Review. *Crit. Rev. Environ. Sci. Technol.* **2009**, *39*, 433–477.

(35) Mehta, C. M.; Khunjar, W. O.; Nguyen, V.; Tait, S.; Batstone, D. J. Technologies to Recover Nutrients from Waste Streams: A Critical Review. *Crit. Rev. Environ. Sci. Technol.* **2015**, *45*, 385–427.

(36) Lee, C.-G.; Alvarez, P. J. J.; Kim, H.-G.; Jeong, S.; Lee, S.; Lee, K. B.; Lee, S.-H.; Choi, J.-W. Phosphorous Recovery from Sewage Sludge Using Calcium Silicate Hydrates. *Chemosphere* **2018**, *193*, 1087–1093.

(37) Cordell, D.; Rosemarin, A.; Schröder, J. J.; Smit, A. L. Towards Global Phosphorus Security: A Systems Framework for Phosphorus Recovery and Reuse Options. *Chemosphere* **2011**, *84*, 747–758.

(38) Cai, T.; Park, S. Y.; Li, Y. Nutrient Recovery from Wastewater Streams by Microalgae: Status and Prospects. *Renew. Sustain. Energy Rev.* **2013**, *19*, 360–369.

(39) Yuan, Z.; Pratt, S.; Batstone, D. J. Phosphorus Recovery from Wastewater through Microbial Processes. *Curr. Opin. Biotechnol.* **2012**, *23*, 878–883.

(40) Puyol, D.; Batstone, D. J.; Hülsen, T.; Astals, S.; Peces, M.; Krömer, J. O. Resource Recovery from Wastewater by Biological Technologies: Opportunities, Challenges, and Prospects. *Front. Microbiol.* **2017**, *7*, 1–23.

(41) Harris, S. M.; Nguyen, J. T.; Pailloux, S. L.; Mansergh, J. P.; Dresel, M. J.; Swanholm, T.

B.; Gao, T.; Pierre, V. C. Gadolinium Complex for the Catch and Release of Phosphate from Water. *Environ. Sci. Technol.* **2017**, *51*, 4549–4558.

(42) Desmidt, E.; Ghyselbrecht, K.; Zhang, Y.; Pinoy, L.; Van Der Bruggen, B.; Verstraete, W.; Rabaey, K.; Meesschaert, B. Global Phosphorus Scarcity and Full-Scale P-Recovery Techniques: A Review. *Crit. Rev. Environ. Sci. Technol.* **2015**, *45*, 336–384.

(43) Cisse, L.; Mrabet, T. World Phosphate Production: Overview and Prospects. *Phosphorus Res. Bull.* **2004**, *15*, 21–25.

(44) Cordell, D.; Drangert, J. O.; White, S. The Story of Phosphorus: Global Food Security and Food for Thought. *Glob. Environ. Chang.* **2009**, *19*, 292–305.

(45) Smith, V. H.; Schindler, D. W. Eutrophication Science: Where Do We Go from Here? *Trends Ecol. Evol.* **2009**, *24*, 201–207.

(46) Mapare, S. V.; Yu, P.-L.; Sarkar, A.; Mukhopadhyay, S. C. A Review of Sensor Technology for In-Field Phosphate Monitoring. In *2013 Seventh International Conference on Sensing Technology (ICST)*; IEEE, 2013; pp 411–418.

(47) Dreusicke, D.; Schulz, G. E. The Glycine-Rich Loop of Adenylate Kinase Forms a Giant Anion Hole. *FEBS Lett.* **1986**, *208*.

(48) Saraste, M.; Sibbald, P. R.; Wittinghofer, A. The P-Loop - a Common Motif in ATP- and GTP-Binding Proteins. *Trends Biochem. Sci.* **1990**, *15*, 430–434.

(49) Watson, J. D.; Milner-White, E. J. A Novel Main-Chain Anion-Binding Site in Proteins: The Nest. A Particular Combination of φ,ψ Values in Successive Residues Gives Rise to Anion-Binding Sites That Occur Commonly and Are Found Often at Functionally Important Regions. *J. Mol. Biol.* **2002**, *315*, 171–182.

(50) Leipe, D. D.; Wolf, Y. I.; Koonin, E. V; Aravind, L. Classification and Evolution of P-

Loop GTPases and Related ATPases. *J. Mol. Biol.* **2002**, *317*, 41–72.

(51) Denessiouk, K. A.; Johnson, M. S.; Denesyuk, A. I. Novel CαNN Structural Motif for Protein Recognition of Phosphate Ions. *J. Mol. Biol.* **2005**, *345*, 611–629.

(52) Milner-White, E. J.; Russell, M. J. Sites for Phosphates and Iron-Sulfur Thiolates in the First Membranes: 3 to 6 Residue Anion-Binding Motifs (Nests). *Orig. Life Evol. Biosph.* **2005**, *35*, 19–27.

(53) Sheet, T.; Supakar, S.; Banerjee, R. Conformational Preference of "CNN" Short Peptide Motif towards Recognition of Anions. *PLoS One* **2013**, *8*.

(54) Afzal, A. M.; Al-Shubailly, F.; Leader, D. P.; Milner-White, E. J. Bridging of Anions by Hydrogen Bonds in Nest Motifs and Its Significance for Schellman Loops and Other Larger Motifs within Proteins. *Proteins Struct. Funct. Bioinforma.* **2014**, *82*, 3023–3031.

(55) Priya, R.; Kumar, A.; Manimekalai, M. S. S.; Grüber, G. Conserved Glycine Residues in the P-Loop of ATP Synthases Form a Doorframe for Nucleotide Entrance. *J. Mol. Biol.* **2011**, *413*.

(56) Bianchi, A.; Giorgi, C.; Ruzza, P.; Toniolo, C.; Milner-White, E. J. A Synthetic Hexapeptide Designed to Resemble a Proteinaceous P-Loop Nest Is Shown to Bind Inorganic Phosphate. *Proteins Struct. Funct. Bioinforma.* **2012**, *80*, 1418–1424.

(57) Zhai, H.; Qin, L.; Zhang, W.; Putnis, C. V.; Wang, L. Dynamics and Molecular Mechanism of Phosphate Binding to a Biomimetic Hexapeptide. *Environ. Sci. Technol.* **2018**, *52*, 10472–10479.

(58) Zhu, H.; Wang, H.; Shi, B.; Shangguan, L.; Tong, W.; Yu, G.; Mao, Z.; Huang, F. Supramolecular Peptide Constructed by Molecular Lego Allowing Programmable Self-Assembly for Photodynamic Therapy. *Nat. Commun.* **2019**, *10*, 1–10.

(59) Hartgerink, J. D.; Beniash, E.; Stupp, S. I. Self-Assembly and Mineralization of Peptide-Amphiphile Nanofibers. *Science (80-.).* **2001**, *294*, 1684–1688.

(60) Trent, A.; Marullo, R.; Lin, B.; Black, M.; Tirrell, M. Structural Properties of Soluble Peptide Amphiphile Micelles. *Soft Matter* **2011**, *7*, 9572–9582.

(61) Missirlis, D.; Chworos, A.; Fu, C. J.; Khant, H. A.; Krogstad, D. V.; Tirrell, M. Effect of the Peptide Secondary Structure on the Peptide Amphiphile Supramolecular Structure and Interactions. *Langmuir* **2011**, *27*, 6163–6170.

(62) Chung, E. J.; Cheng, Y.; Morshed, R.; Nord, K.; Han, Y.; Wegscheid, M. L.; Auffinger, B.; Wainwright, D. A.; Lesniak, M. S.; Tirrell, M. V. Fibrin-Binding, Peptide Amphiphile Micelles for Targeting Glioblastoma. *Biomaterials* **2014**, *35*, 1249–1256.

(63) Li, Y.; Lock, L. L.; Mills, J.; Ou, B. S.; Morrow, M.; Stern, D.; Wang, H.; Anderson, C. F.; Xu, X.; Ghose, S.; Li, Z. J.; Cui, H. Selective Capture and Recovery of Monoclonal Antibodies by Self-Assembling Supramolecular Polymers of High Affinity for Protein Binding. *Nano Lett.* **2020**, *20*, 6957–6965.

(64) Yang, Q.; Zhu, Y.; Luo, B.; Lan, F.; Wu, Y.; Gu, Z. PH-Responsive Magnetic Metal-Organic Framework Nanocomposites for Selective Capture and Release of Glycoproteins. *Nanoscale* **2017**, *9*, 527–532.

(65) Chen, Y.; Li, P.; Modica, J. A.; Drout, R. J.; Farha, O. K. Acid-Resistant Mesoporous Metal-Organic Framework toward Oral Insulin Delivery: Protein Encapsulation, Protection, and Release. *J. Am. Chem. Soc.* **2018**, *140*, 5678–5681.

(66) Hasan, Z.; Jhung, S. H. Removal of Hazardous Organics from Water Using Metal-Organic Frameworks (MOFs): Plausible Mechanisms for Selective Adsorptions. *J. Hazard. Mater.* **2015**, *283*, 329–339.

(67) Tu, R. S.; Tirrell, M. Bottom-up Design of Biomimetic Assemblies. *Adv. Drug Deliv. Rev.* **2004**, *56*, 1537–1563.

(68) Nagul, E. A.; McKelvie, I. D.; Worsfold, P.; Kolev, S. D. The Molybdenum Blue Reaction for the Determination of Orthophosphate Revisited: Opening the Black Box. *Anal. Chim. Acta* **2015**, *890*, 60–82.

(69) Ganesh, S.; Khan, F.; Ahmed, M. K.; Velavendan, P.; Pandey, N. K.; Kamachi Mudali, U. Spectrophotometric Determination of Trace Amounts of Phosphate in Water and Soil. *Water Sci. Technol.* **2012**, *66*, 2653.

(70) Abraham, M. J.; Murtola, T.; Schulz, R.; Páll, S.; Smith, J. C.; Hess, B.; Lindah, E. Gromacs: High Performance Molecular Simulations through Multi-Level Parallelism from Laptops to Supercomputers. *SoftwareX* **2015**, *1–2*, 19–25.

(71) Sidky, H.; Colón, Y. J.; Helfferich, J.; Sikora, B. J.; Bezik, C.; Chu, W.; Giberti, F.; Guo, A. Z.; Jiang, X.; Lequieu, J.; Li, J.; Moller, J.; Quevillon, M. J.; Rahimi, M.; Ramezani-Dakhel, H.; Rathee, V. S.; Reid, D. R.; Sevgen, E.; Thapar, V.; Webb, M. A.; Whitmer, J. K.; De Pablo, J. J. SSAGES: Software Suite for Advanced General Ensemble Simulations. *J. Chem. Phys.* **2018**, *148*.

(72) Vanommeslaeghe, K.; Hatcher, E.; Acharya, C.; Kundu, S.; Zhong, S.; Shim, J.; Darian, E.; Guvench, O.; Lopes, P.; Vorobyov, I.; Mackerell, A. D. CHARMM General Force Field: A Force Field for Drug-like Molecules Compatible with the CHARMM All-Atom Additive Biological Force Fields. *J. Comput. Chem.* **2009**, *32*, 671–690.

(73) Jorgensen, W. L.; Chandrasekhar, J.; Madura, J. D.; Impey, R. W.; Klein, M. L. Comparison of Simple Potential Functions for Simulating Liquid Water. *J. Chem. Phys.* **1983**, *79*, 926–935.

(74) Essmann, U.; Perera, L.; Berkowitz, M. L.; Darden, T.; Lee, H.; Pedersen, L. G. A Smooth Particle Mesh Ewald Method. *J. Chem. Phys.* **1995**, *103*, 8577–8593.

(75) Hess, B.; Bekker, H.; Berendsen, H. J. C.; Fraaije, J. G. E. M. LINCS: A Linear Constraint Solver for Molecular Simulations. *J. Comput. Chem.* **1997**, *18*, 1463–1472.

(76) Daura, X.; Gademann, K.; Jaun, B.; Seebach, D.; van Gunsteren, W. F.; Mark, A. E. Peptide Folding: When Simulation Meets Experiment. *Angew. Chemie Int. Ed.* **1999**, *38*, 236–240.

(77) Lee, O. S.; Stupp, S. I.; Schatz, G. C. Atomistic Molecular Dynamics Simulations of Peptide Amphiphile Self-Assembly into Cylindrical Nanofibers. *J. Am. Chem. Soc.* **2011**, *133*, 3677–3683.

(78) Eisenhaber, F.; Lijnzaad, P.; Argos, P.; Sander, C.; Scharf, M. The Double Cubic Lattice Method: Efficient Approaches to Numerical Integration of Surface Area and Volume and to Dot Surface Contouring of Molecular Assemblies. *J. Comput. Chem.* **1995**, *16*, 273–284.

(79) Thayer, A. M. Making Peptides At Large Scale. *Chem. Eng. News Arch.* **2011**, *89*, 21–25.

(80) Gruber, M.; Greisen, P.; Junker, C. M.; Hélix-Nielsen, C. Phosphorus Binding Sites in Proteins: Structural Preorganization and Coordination. *J. Phys. Chem. B* **2014**, *118*, 1207–1215.

(81) Romero Romero, M. L.; Yang, F.; Lin, Y. R.; Toth-Petroczy, A.; Berezovsky, I. N.; Goncearenco, A.; Yang, W.; Wellner, A.; Kumar-Deshmukh, F.; Sharon, M.; Baker, D.; Varani, G.; Tawfik, D. S. Simple yet Functional Phosphate-Loop Proteins. *Proc. Natl. Acad. Sci. U. S. A.* **2018**, *115*, E11943–E11950.

(82) Zhai, H.; Qin, L.; Zhang, W.; Putnis, C. V.; Wang, L. Dynamics and Molecular

Mechanism of Phosphate Binding to a Biomimetic Hexapeptide. *Environ. Sci. Technol.* **2018**, *52*, 10472–10479.

(83) Paramonov, S. E.; Jun, H. W.; Hartgerink, J. D. Self-Assembly of Peptide-Amphiphile Nanofibers: The Roles of Hydrogen Bonding and Amphiphilic Packing. *J. Am. Chem. Soc.* **2006**, *128*, 7291–7298.

(84) Israelachvili, J. N.; Mitchell, D. J.; Ninham, B. W. Theory of Self-Assembly of Hydrocarbon Amphiphiles into Micelles and Bilayers. *J. Chem. Soc. Faraday Trans. 2* **1976**, *72*, 1525.

(85) Schneider, C. A.; Rasband, W. S.; Eliceiri, K. W. NIH Image to ImageJ: 25 Years of Image Analysis. *Nat. Methods* **2012**, *9*, 671–675.

(86) Ghosh, A.; Haverick, M.; Stump, K.; Yang, X.; Tweedle, M. F.; Goldberger, J. E. Fine-Tuning the PH Trigger of Self-Assembly. *J. Am. Chem. Soc.* **2012**, *134*, 3647–3650.

(87) Gebhardt, K. E.; Ahn, S.; Venkatachalam, G.; Savin, D. A. Rod-Sphere Transition in Polybutadiene-Poly(L-Lysine) Block Copolymer Assemblies. *Langmuir* **2007**, *23*, 2851–2856.

(88) Bunce, J. T.; Ndam, E.; Ofiteru, I. D.; Moore, A.; Graham, D. W. A Review of Phosphorus Removal Technologies and Their Applicability to Small-Scale Domestic Wastewater Treatment Systems. *Front. Environ. Sci.* **2018**, *6*, 1–15.

(89) Gruber, M. F.; Wood, E.; Truelsen, S.; Østergaard, T.; Hélix-Nielsen, C. Computational Design of Biomimetic Phosphate Scavengers. *Environ. Sci. Technol.* **2015**, *49*, 9469–9478.

(90) Comer, J.; Gumbart, J. C.; Hénin, J.; Lelievre, T.; Pohorille, A.; Chipot, C. The Adaptive Biasing Force Method: Everything You Always Wanted to Know but Were Afraid to Ask.

J. Phys. Chem. B **2015**, *119*, 1129–1151.

(91) Chouyyok, W.; Wiacek, R. J.; Fryxell, G. E. Phosphate Removal by Anion Binding on Functionalized Nanoporous Sorbents. *Environ. Sci. Technol.* **2010**, *44*, 3073–3078.

(92) Liu, H.; Sun, X.; Yin, C.; Hu, C. Removal of Phosphate by Mesoporous ZrO2. *J. Hazard. Mater.* **2008**, *151*, 616–622.

(93) Zeng, L.; Li, X.; Liu, J. Adsorptive Removal of Phosphate from Aqueous Solutions Using Iron Oxide Tailings. *Water Res.* **2004**, *38*, 1318–1326.

(94) Fowler, W. C.; Deng, C.; Gri, G. M.; Teodoro, T.; Guo, A. Z.; Zaiden, M.; Gottlieb, M.; Pablo, J. J. De; Tirrell, M. V. Harnessing Peptide Binding to Capture and Reclaim Phosphate. *J. Am. Chem. Soc.* **2021**, *143*, 4440–4450.

(95) Choi, T. S.; Tezcan, F. A. Overcoming Universal Restrictions on Metal Selectivity by Protein Design. *Nature* **2022**, *603*, 522–527.

(96) Berndt, P.; Fields, G. B.; Tirrell, M. Synthetic Lipidation of Peptides and Amino Acids: Monolayer Structure and Properties. *J. Am. Chem. Soc.* **1995**, *117*, 9515–9522.

(97) Yu, Y. C.; Berndt, P.; Tirrell, M.; Fields, G. B. Self-Assembling Amphiphiles for Construction of Protein Molecular Architecture. *J. Am. Chem. Soc.* **1996**, *118*, 12515–12520.

(98) Hendricks, M. P.; Sato, K.; Palmer, L. C.; Stupp, S. I. Supramolecular Assembly of Peptide Amphiphiles. *Acc. Chem. Res.* **2017**, *50*, 2440–2448.

(99) Acar, H.; Samaeekia, R.; Schnorenberg, M. R.; Sasmal, D. K.; Huang, J.; Tirrell, M. V.; LaBelle, J. L. Cathepsin-Mediated Cleavage of Peptides from Peptide Amphiphiles Leads to Enhanced Intracellular Peptide Accumulation. *Bioconjug. Chem.* **2017**, *28*, 2316–2326.

(100) Greenfield, M. A.; Hoffman, J. R.; De La Cruz, M. O.; Stupp, S. I. Tunable Mechanics of

Peptide Nanofiber Gels. *Langmuir* **2010**, *26*, 3641–3647.

(101) Kastantin, M.; Missirlis, D.; Ananthanarayanan, B.; Neumann, T.; Tirrell, M.; Farine, M. Linker Chemistry Determines Secondary Structure of P53 14−29 in Peptide Amphiphile Micelles . *Bioconjug. Chem.* **2010**, *21*, 465–475.

(102) Barrett, J. C.; Ulery, B. D.; Trent, A.; Liang, S.; David, N. A.; Tirrell, M. V. Modular Peptide Amphiphile Micelles Improving an Antibody-Mediated Immune Response to Group A Streptococcus. *ACS Biomater. Sci. Eng.* **2016**, *3*, 144–152.

(103) Behanna, H. A.; Donners, J. J. J. M.; Gordon, A. C.; Stupp, S. I. Coassembly of Amphiphiles with Opposite Peptide Polarities into Nanofibers. *J. Am. Chem. Soc.* **2005**, *127*, 1193–1200.

(104) Ye, R.; Liu, Y.; Zhang, H.; Su, H.; Zhang, Y.; Xu, L.; Hu, R.; Kwok, R. T. K.; Wong, K. S.; Lam, J. W. Y.; Goddard, W. A.; Tang, B. Z. Non-Conventional Fluorescent Biogenic and Synthetic Polymers without Aromatic Rings. *Polym. Chem.* **2017**, *8*, 1722–1727.

(105) Chatterjee, D. P.; Pakhira, M.; Nandi, A. K. Fluorescence in “Nonfluorescent” Polymers. *ACS Omega* **2020**, *5*, 30747–30766.

(106) YongYang, G.; YeQiang, T.; Ju, M.; Yiren, Z.; WangZhang, Y.; YongMing, Z.; JingZhi, S.; Zhong, T. Ben. Room Temperature Phosphorescence from Natural Products: Crystallization Matters. *Sci. China Chem.* **2013**, *56*, 1178–1182.

(107) Wang, Y.; Bin, X.; Chen, X.; Zheng, S.; Zhang, Y.; Yuan, W. Z. Emission and Emissive Mechanism of Nonaromatic Oxygen Clusters. *Macromol. Rapid Commun.* **2018**, *39*, 1–6.

(108) Liu, C.; Cui, Q.; Wang, J.; Liu, Y.; Chen, J. Autofluorescent Micelles Self-Assembled from an AIE-Active Luminogen Containing an Intrinsic Unconventional Fluorophore. *Soft Matter* **2016**, *12*, 4295–4299.

(109) Homchaudhuri, L.; Swaminathan, R. Novel Absorption and Fluorescence Characteristics of L-Lysine. *Chem. Lett.* **2001**, No. 8, 844–845.

(110) Homchaudhuri, L.; Swaminathan, R. Near Ultraviolet Absorption Arising from Lysine Residues in Close Proximity: A Probe to Monitor Protein Unfolding and Aggregation in Lysine-Rich Proteins. *Bull. Chem. Soc. Jpn.* **2004**, *77*, 765–769.

(111) Luo, J.; Xie, Z.; Xie, Z.; Lam, J. W. Y.; Cheng, L.; Chen, H.; Qiu, C.; Kwok, H. S.; Zhan, X.; Liu, Y.; Zhu, D.; Tang, B. Z. Aggregation-Induced Emission of 1-Methyl-1,2,3,4,5-Pentaphenylsilole. *Chem. Commun.* **2001**, *18*, 1740–1741.

(112) Ellis, B.; Brignola, P.; Brashear, R. L.; Thomas, R.; Dickerson, S. H.; Dickson, H. D.; Kelly, H.; Gaul, M.; Griffin, R. J.; Hassell, A. M.; Keith, B.; Mullin, R.; Petrov, K. G.; Reno, M. J.; Rusnak, D. W.; Tadepalli, S. M.; Ulrich, J. C.; Craig, D.; Vanderwall, D. E.; Waterson, A. G.; Williams, J. D.; White, W. L.; Uehling, D. E.; Pompa, P. P.; Maruccio, G.; Della, A.; Sabella, S.; Tamburro, A. M.; Laureana, L.; Pompa, P. P.; Maruccio, G.; Torre, A. Della; Sabella, S.; Tamburro, A. M.; Cingolani, R.; Rinaldi, R. Charge Transport and Intrinsic Fluorescence in Amyloid-like Fibrils. *Proc. Natl. Acad. Sci. U. S. A.* **2007**, *104*, 18019–18024.

(113) Chen, X.; Luo, W.; Ma, H.; Peng, Q.; Yuan, W. Z.; Zhang, Y. Prevalent Intrinsic Emission from Nonaromatic Amino Acids and Poly(Amino Acids). *Sci. China Chem.* **2018**, *61*, 351–359.

(114) Hu, R.; Wang, J.; Qin, A.; Tang, B. Z. Aggregation-Induced Emission-Active Biomacromolecules: Progress, Challenges, and Opportunities. *Biomacromolecules* **2021**.

(115) Kang, M.; Zhang, Z.; Song, N.; Li, M.; Sun, P.; Chen, X.; Wang, D.; Tang, B. Z. Aggregation-enhanced Theranostics: AIE Sparkles in Biomedical Field. *Aggregate* **2020**,

1, 80–106.

(116) Huang, X.; Gu, X.; Zhang, G.; Zhang, D. A Highly Selective Fluorescence Turn-on Detection of Cyanide Based on the Aggregation of Tetraphenylethylene Molecules Induced by Chemical Reaction. *Chem. Commun.* **2012**, *48*, 12195–12197.

(117) Neupane, L. N.; Oh, E. T.; Park, H. J.; Lee, K. H. Selective and Sensitive Detection of Heavy Metal Ions in 100% Aqueous Solution and Cells with a Fluorescence Chemosensor Based on Peptide Using Aggregation-Induced Emission. *Anal. Chem.* **2016**, *88*, 3333–3340.

(118) Gao, M.; Tang, B. Z. Fluorescent Sensors Based on Aggregation-Induced Emission: Recent Advances and Perspectives. *ACS Sensors* **2017**, *2*, 1382–1399.

(119) Bao, P.; Li, C.; Ou, H.; Ji, S.; Chen, Y.; Gao, J.; Yue, X.; Shen, J.; Ding, D. A Peptide-Based Aggregation-Induced Emission Bioprobe for Selective Detection and Photodynamic Killing of Gram-Negative Bacteria. *Biomater. Sci.* **2021**, *9*, 437–442.

(120) Wu, T.; Huang, J.; Yan, Y. Self-Assembly of Aggregation-Induced-Emission Molecules. *Chem. - An Asian J.* **2019**, *14*, 730–750.

(121) Honggang, C.; Webber, M. J.; Stupp, S. I. Self-Assembly of Peptide Amphiphiles: From Molecules to Nanostructures to Biomaterials. *Pept. Sci.* **2010**, *94*, 1–18.

(122) Lin, L. Y.; Huang, P. C.; Yang, D. J.; Gao, J. Y.; Hong, J. L. Influence of the Secondary Structure on the AIE-Related Emission Behavior of an Amphiphilic Polypeptide Containing a Hydrophobic Fluorescent Terminal and Hydrophilic Pendant Groups. *Polym. Chem.* **2016**, *7*, 153–163.

(123) Li, S. T.; Lin, Y. C.; Kuo, S. W.; Chuang, W. T.; Hong, J. L. Aggregation Induced Emission Enhancement in Relation to the Secondary Structures of Poly(γ-Benzyl-l-

Glutamate) Containing a Fluorescent Tetraphenylthiophene Moiety. *Polym. Chem.* **2012**, *3*, 2393–2402.

(124) Stuart, M. C. A.; Boekema, E. J. Two Distinct Mechanisms of Vesicle-to-Micelle and Micelle-to-Vesicle Transition Are Mediated by the Packing Parameter of Phospholipid–Detergent Systems. *Biochim. Biophys. Acta - Biomembr.* **2007**, *1768*, 2681–2689.

(125) Sivaguru, M.; Khaw, Y. M.; Inoue, M. A Confocal Reflection Super-Resolution Technique to Image Golgi-Cox Stained Neurons. *J. Microsc.* **2019**, *275*, 115–130.

(126) Zhang, X.; Jackson, J. K.; Burt, H. M. Determination of Surfactant Critical Micelle Concentration by a Novel Fluorescence Depolarization Technique. *J. Biochem. Biophys. Methods* **1996**, *31*, 145–150.

(127) Melhuish, W. H. Quantum Efficiencies of Fluorescence of Organic Substances: Effect of Solvent and Concentration of the Fluorescent Solute. *J. Phys. Chem.* **1961**, *65*, 229–235.

(128) Zhang, Z.; Xiong, J.; He, G.; Dang, D.; Xie, Y.; Wang, Q. Fluorous Effect-Induced Emission of Azido Substituted Poly(Vinylidene Fluoride) with High Photostability and Film Formation. *Polym. Chem.* **2020**, *11*, 1307–1313.

(129) Marullo, R.; Kastantin, M.; Drews, L. B.; Tirrell, M. Peptide Contour Length Determines Equilibrium Secondary Structure in Protein-Analogous Micelles. *Biopolymers* **2013**, *99*, 573–581.

(130) Chua, M. H.; Shah, K. W.; Zhou, H.; Xu, J. Recent Advances in Aggregation-Induced Emission Chemosensors for Anion Sensing. *Molecules* **2019**, *24*.

(131) Chen, J.; Xie, Z.; Lam, J. W. Y.; Law, C. C. W.; Tang, B. Z. Silole-Containing Polyacetylenes. Synthesis, Thermal Stability, Light Emission, Nanodimensional Aggregation, and Restricted Intramolecular Rotation. *Macromolecules* **2003**, *36*, 1108–

1117.

(132) Sun, Y.; Neary, W. J.; Burke, Z. P.; Qian, H.; Zhu, L.; Moore, J. S. Mechanically Triggered Carbon Monoxide Release with Turn-On Aggregation-Induced Emission. *J. Am. Chem. Soc.* **2022**, *144*, 1125–1129.